UNIVERSITY OF CALIFORNIA SAN DIEGO

A Soft Platform for Cellular Electrophysiology Recording

A dissertation submitted in partial satisfaction of the
requirements for the degree
Doctor of Philosophy

in

Materials Science and Engineering

by

Yue Gu

Committee in charge:

Professor Sheng Xu, Chair
Professor Shadi A. Dayeh
Professor Duygu Kuzum
Professor Andrew D. McCulloch
Professor Joseph Wang

2021

The dissertation of Yue Gu is approved,

and it is acceptable in quality and form for publication

on microfilm and electronically.

University of California San Diego

2021

DEDICATION

To my wife, Jie, and our parents.

EPIGRAPH

Two things fill the mind with ever new and increasing admiration and awe,

the more often and steadily we reflect upon them:

the starry heavens above me and the moral law within me.

--Immanuel Kant

TABLE OF CONTENTS

LIST OF FIGURES

ACKNOWLEDGMENTS

Above all, I would like to express my sincere gratitude to my advisor, Professor Sheng Xu, for the continuous support and guidance of my Ph.D. study and research, for his patience in training me, and for believing in me and offering me the great opportunity to work in the most creative and cooperative team that I could ever dream of. His broad scientific vision, enthusiasm in solving various true challenges, optimism in the face of difficulties, and high self-discipline standard profoundly influence and educate me, leading and shaping me into who I am today. It is my great honor to be able to graduate from Xu lab, and I could not have imagined having a better advisor for my Ph.D. study.

Besides my advisor, I would like to thank the rest of Xu Group members. Without their tremendous help, I could not acquaint the knowledge and skills so quickly to progress. Special thanks to Hongjie, Yusheng, Yimu, Chunfeng, and Yang, who accompanied me when I felt lost and gave me the strength to carry on. They are great friends in my life and role models in my academic career. I will treasure the friendship we built, the memories we experienced, and the work we made together. My sincere thanks also go to Namheon, who involved me in his fantastic projects and taught me micro/nano-fabrication techniques without any reservation. He has been my work partner, collaborator, and mentor. I will never forget the hundreds of hours we spent together in the cleanroom. To Zhenlong, for always being available when I ask him any question. I admire his abundant enthusiasm for research and life. I would also like to thank Dr. Lin Zhang for his genuine suggestions and generous help over the years.

To the CMRG team led by Prof. Andrew McCulloch, for his tremendous support of my doctoral work. In particular, I would like to thank Jen and Min, for their trust and generosity. I spent much more time in BSB or CMRG lab than our lab, bringing lots of trouble to Jen and the rest of the team. I feel grateful for her patience in training me and showing me how a professional researcher behaves. To Min, I would express my sincere appreciation to her, for her continuous help and encouragement, for teaching me how to perform a patch clamping and calcium ion flux recording. I feel fortunate to have her as a collaborator, with whom I could share my ideas and concerns in research. Her optimism in life always inspired me to persist during tough times.

I would also like to give my deepest thanks to Prof. Xiaocheng Jiang, Leo, and Xiaochuan at Tufts University, for teaching me electrophysiological sensing approaches and providing HL-1 cells. I could not finish the cardiomyocyte sensing project without their support and advice. Also, to our collaborators from Terasaki Institute for Biomedical Innovation, Prof. Ali Khademhosseini, Prof. Samad Ahadian, Dr. Rohollah Nasiri, for providing the engineered cardiac microtissue constructs, with which we could promote the project to such a high level, and for their trust and patience while we were preparing the manuscript. I would also like to thank Prof. Liangfang Zhang and Dr. Hua Gong, for providing us with the blood cell membranes and educating us on cell membrane manipulation and coating. To our UCI collaborators, Prof. Peter Burke and Dr. Jinfeng Li, I would like to thank them for providing the beautiful AFM and SMM images of our FET sensors and for the careful explanations of the results.

I acknowledge all the staff engineers and friends that I was blessed to meet in the Nano3 cleanroom, because of whom I was able to comfort myself and stay long there. Special thanks to

Mehran, Yun Goo, Samheon, Ren, Renjie, Keundong in Prof. Shadi Dayeh group, and Yichen, Yuhan in Prof. Duygu Kuzum group, for their selfless and prompt help, as well as for their companies in days and nights.

I would like to say thank you to my dear parents for the endless love and care from the beginning of my life. Thank you for your huge support, both financially and mentally, for your trust and respect. My great appreciation to all my family members, who always show unconditional love and stand by my side. Especially to my grandma above there, I wish you could see this day with joy and pride.

Finally, I acknowledge my wife, Jie. Meeting her in UCSD and in the cleanroom is the most romantic thing in my life. It is also my fortune to have her as my best friend. Thank you for giving me unconditional love and trust, for sparking fires in my mind, and accompany me to grow up and strong. Meeting you, knowing you, and marrying you is the best thing happening in the days that I spent in the US. I am also glad to witness each other's improvement. All my successes are also shared with her.

Chapters Two to Five, in full, is a partial reprint of the materials: 'Three-dimensional transistor arrays for intra- and inter-cellular recording, Yue Gu, Chunfeng Wang, Namheon Kim, Jingxin Zhang, Tsui Min Wang, Jennifer Stowe, Rohollah Nasiri, Jinfeng Li, Daibo Zhang, Albert Yang, Leo Huan-Hsuan Hsu, Xiaochuan Dai, Jing Mu, Zheyuan Liu, Muyang Lin, Weixin Li, Chonghe Wang, Hua Gong, Yimu Chen, Yusheng Lei, Hongjie Hu, Yang Li, Lin Zhang, Zhenlong Huang, Xingcai Zhang, Samad Ahadian, Pooja Banik, Liangfang Zhang, Xiaocheng Jiang, Peter

J. Burke, Ali Khademhosseini, Andrew D. McCulloch, Sheng Xu, accepted in Nature Nanotechnology, 2021'. The dissertation author was the first author of this paper.

Yue Gu

San Diego, CA

September

VITA

2012 Bachelor of Engineering in Electronic Packaging Technologies

Beijing Institute of Technology

2015 Master of Engineering in Materials Science and Engineering

Beijing Institute of Technology

2021 Doctor of Philosophy in Materials Science and Engineering

University of California San Diego

PUBLICATIONS

(* authors contributed equally to the work)

Gu, Y., Wang, C.F., Kim, N., Zhang, J., Wang, T.M., Stowe, J., Nasiri, R., Li, J.F., Zhang, D., Yang, A., Hsu, L. H.-H., Dai, X., Mu, J., Liu, Z., Lin, M., Li, W., Wang, C., Gong, H., Chen, Y., Lei, Y., Hu, H., Li, Y., Zhang, L., Huang, Z., Zhang, X., Ahadian, S., Banik, P., Zhang, L., Jiang, X., Burke, P.J., Khademhosseini, A., McCulloch, A.D., Xu, S., "Three-dimensional transistor arrays for intra- and inter-cellular recording", Nature Nanotechnology, 2021, accepted.

Chen, X., Gao, X., Nomoto, A., Shi, K., Lin, M., Hu, H., Gu, Y., Zhu, Y., Wu, Z., Chen, X., Wang, X., Qi, B., Zhou, S., Ding, H., Xu, S., "Fabric-substrated capacitive biopotential sensors enhanced by dielectric nanoparticles", Nano Research, 2021, 14, 3248-3252.

Wang, C., Qi, B., Lin, M., Zhang, Z., Makihata, M., Liu, B., Zhou, S., Huang, Y., Hu, H., Gu, Y., Chen, Y., Lei, Y., Lee, T., Chien, S., Jang, K., Kistiler, E., Xu, S., "Continuous monitoring of deep-tissue haemodynamics with stretchable ultrasonic phased arrays", Nature Biomedical Engineering, 2021, 5(7), 749-758.

Ma X., Ahadian, S., Liu, S., Zhang, J., Liu, S, Cao, T., Lin, W., Wu, D., Roberto de Barros, N., Zare, M., Diltemiz, S., Jucaud, V., Zhu, Y., Zhang, S., Banton, E., Gu, Y., Nan, K., Xu, S., Dokmeci,M., Khademhosseini, A., "Smart Contact Lenses for Biosensing Applications", Advanced Intelligent Systems, 2021, 3(5), 20000263.

Lei, Y.*, Chen, Y.*, Zhang, R., Li, Y., Yan, Q., Lee, S., Yu, Y., Tsai, H., Choi, W., Wang, K., Luo, Y., Gu, Y., Zheng, X., Wang, C., Wang, C., Hu, H., Li, Y., Qi, B., Lin, M., Zhang, Z., Dayeh. S., Pharr, M., Fenning, D., Lo, Y., Luo, J., Yang, K., Yoo, J., Nie, W., Xu, S., "A fabrication process for flexible single-crystal perovskite devices", Nature, 2020, 583, 790-795.

Hou, Z., Zhao, X., Liu, Y., Tan, C., Gu, Y., "Comparative study on the hourglass-like joint of electroplated Sn-base solder reinforced by adding Ag_3Sn nanoparticles and Ag micro-alloying elements" Materialia, 2020, 9, 100558.

Chen, Y.*, Lei, Y.*, Li, Y., Yu, Y., Cai, J., Chiu, M., Rao, R., Gu, Y., Wang, C., Choi, W., Hu, H., Wang, C., Li, Y., Song, J., Zhang, J., Qi, B., Lin, M., Zhang, Z., Islam, A., Maruyama, B., Dayeh, S., Li, L., Yang, K., Lo, Y., Xu, S., "Strain Engineering and Epitaxial Stabilization of Halide Perovskites", Nature, 2020, 577, 209.

Hong, S., Gu, Y., Seo, J., Wang, J., Liu, P., Meng, Y., Xu, S., Chen, R., "Wearable thermoelectrics for personalized thermoregulation", Science Advances, 2019, 5(5), eaaw0536.

Gong, H.*, Chen, F.*, Huang, Z.*, Gu, Y.*, Zhang, Q., Chen, Y., Zhang, Y., Zhuang, J., Cho, Y., Fang, R., Gao, W., Xu, S., Zhang, L., "Biomembrane-Modified Field Effect Transistors for Sensitive and Quantitative Detection of Biological Toxins and Pathogens", ACS Nano, 2019.

Wang, C., Li, X., Hu, H., Zhang, L., Huang, Z., Lin, M., Zhang, Z., Yin, Z., Huang, B., Gong, H., Bhaskaran, S., Gu, Y., Makihata, M., Guo, Y., Lei, Y., Chen, Y., Wang, C., Li, Y., Zhang, T., Chen, Z., Pisano, A., Zhang, L., Zhou, Q., Xu, S., "Monitoring of the central blood pressure waveform via a conformal ultrasonic device", Nature Biomedical Engineering, 2018, 2(9), 687.

Huang, Z., Hao, Y., Li, Y., Hu, H., Wang, C., Nomoto, A., Pan, T., Gu, Y., Chen, Y., Zhang, T., Li, W., Lei, Y., Kim, N., Wang, C., Zhang, L., Ward, J., Maralani, A., Li, X., Durstock, M., Pisano, A., Lin, Y., Xu, S., "Three-dimensional integrated stretchable electronics". Nature Electronics, 2018, 1(8), 473.

Lei, Y.*, Chen, Y.*, Gu, Y., Wang, C., Huang, Z., Qian, H., Nie, J., Hollett, G., Choi, W., Yu, Y., Kim, N., Wang, C., Zhang, T., Hu, H., Zhang, Y., Li, X., Li, Y., Shi, W., Liu, Z., Sailor, M. J., Dong, L., Lo, Y.-H., Luo, J., Xu, S., "Controlled Homoepitaxial Growth of Hybrid Perovskites", Advanced Materials, 2018, 30, 1705992.

Hu, H., Zhu, X., Wang, C., Zhang, L., Li, X., Lee, S., Huang, Z., Chen, R., Chen, Z., Wang, C., Gu, Y., Chen, Y., Lei, Y., Zhang, T., Kim, N., Guo, Y., Teng, Y., Zhou, W., Li, Y., Nomoto, A., Sternini, S., Zhou, Q., Pharr, M., Scalea, F,. Xu, S., "Stretchable ultrasonic transducer arrays for three-dimensional imaging on complex surfaces", Science Advances, 2018, 4(3), eaar3979.
Yang, P., Zhao, X., Liu, Y., Gu, Y., "Facile, Large-Scale and Expeditious Synthesis of Hollow Co and Co@Fe Nanostructures: Application for Electromagnetic Wave Absorption", The Journal of Physical Chemistry C, 2017.

Vinu Mohan, A.M.*, Kim, N.*, Gu, Y.*, Bandodkar, A.*, You, J., Kumar, R., Kurniawan, J., Xu, S., Wang, J., "Merging of Thin- and Thick-Film Fabrication Technologies: Toward Soft Stretchable "Island–Bridge" Devices", Advanced Materials Technologies, 2017, 2(4), 1600284.

Bandodkar, A.*, You, J.*, Kim, N.*, Gu, Y.*, Kumar, R., Vinu Mohan, A., Kurniawan, J., Imani, S., Nakagawa, T., Parish, B., Parthasarathy, M., Mercier, P., Xu, S., Wang, J., "Soft, stretchable, high power density electronic skin-based biofuel cells for scavenging energy from human sweat", Energy & Environmental Science, 2017, 10(7), 1581-1589.

Wen, Y., Zhao, X., Chen, Z., Gu, Y., Wang, Y., Chen, Z., Wang, X., "Reliability enhancement of Sn-1.0 Ag-0.5 Cu nano-composite solders by adding multiple sizes of TiO_2 nanoparticles", Journal of Alloys and Compounds, 2016, 696, 799-807.

Wang, Y., Zhao, X., Xie, X., Gu, Y., Liu, Y., "Effects of nano-SiO_2 particles addition on the microstructure, wettability, joint shear force and the interfacial IMC growth of Sn3.0Ag0.5Cu solder", Journal of Materials Science: Materials in Electronics, 2015, 26(12), 9387-9395.

Gu, Y., Zhao, X., Li, Y., Liu, Y., Wang, Y., Li, Z., "Effect of nano-Fe_2O_3 additions on wettability and interfacial intermetallic growth of low-Ag content Sn–Ag–Cu solders on Cu substrates", Journal of Alloys and Compounds, 2015, 627, 39-47.

Chen, P., Zhao, X., Wang, Y., Liu, Y., Li, H., Gu, Y., "Enhancement of mean-time-to-failure of Sn3. 0Ag0. 5Cu solder bump joint under current stressing via controlling bump shape", Journal of Materials Science: Materials in Electronics, 2015, 26(3), 1940-1949.

Xie, X., Zhao, X., Liu, Y., Cheng, Y., Zheng, B., Gu, Y., "Effect of Ag Addition on Growth of the Interfacial Intermetallic Compounds between Sn-0.7 Cu Solder and Cu Substrate", Materials Science Forum, 2015, 815, 129-134.

Gu, Y., Liu, Y., Zhao, X., Wen, S., Li, H., Wang, Y., "Effects of Cobalt Nanoparticles Addition on Shear Strength, Wettability and Interfacial Intermetallic Growth of Sn−3.0 Ag−0.5 Cu Solder during Thermal Cycling", Materials Science Forum, 2015, 97-102.

Gu, Y., Zhao, X., Liu, Y., Lv, Y., "Preparation and tribological properties of dual-coated TiO_2 nanoparticles as water-based lubricant additives", Journal of Nanomaterials, 2014.

ABSTRACT OF THE DISSERTATION

A Soft Platform for Cellular Electrophysiology Recording

by

Yue Gu

Doctor of Philosophy in Materials Science and Engineering

University of California San Diego, 2021

Professor Sheng Xu, Chair

Electrophysiological studies of electrogenic cells help elucidate, diagnose, and modulate cellular electrical activities. Transmembrane potentials are the manifest of microscopic ionic events and set the bases for macroscopic electrophysiological characteristics of tissues and organs.

Research in this field is largely driven by the versatile tools to precisely record transmembrane potentials of a single cell and a cellular network. The gold-standard patch-clamp, in various forms, is challenging to simultaneously interface different cells due to their poor maneuverability and massive invasiveness during operations. An ideal sensor needs to be in direct contact with the cytoplasm to record intracellular events, based on transistors with minimal access impedance and wide bandwidth at a reduced device size, and scalable to interrogate multiple cells in parallel. Existing nanostructured sensors lack one or more of those requirements. Based on these motivations, we report a three-dimensional (3D) field-effect transistor (FET) array made by a compressive buckling technique. The 3D geometry allows penetrating the cell membrane and recording low-magnitude subthreshold signals inside the cell. A phospholipid coating on the 3D FETs facilitates the spontaneous internalization of the FET into the cytoplasm with minimal invasiveness. Using the 3D FET array, we can record intra- and inter-cellular signal propagation of cardiomyocytes. Also, we demonstrate the intracellular recording of cardiomyocytes in a 3D cardiac tissue construct. This platform technology will help acquire new insights into electrical behaviors in cellular networks and other broad basic electrophysiological studies.

In Chapter One, the basics of electrophysiology and the conventional and novel tools for electrophysiology studies will be introduced. In Chapter Two, the compressive bucking technique will be introduced. Mechanical robustness and electrical properties characterizations of the high-performance field-effect transistors will be discussed. Our work presents the design and fabrication of a customizable soft platform intracellular electrophysiology sensing, which was enabled by the compressive buckling technique. In Chapter Three, intracellular and extracellular

electrophysiological recordings of a cell line and two primary cells will be introduced. Our work presents a high-performance transistor sensor that has the capability of faithful recording full-amplitude action potentials and subthreshold membrane potentials of cardiomyocytes. In Chapter Four, electrical signal propagative behaviors of cells in 2D cell cultures will be introduced. Our work presents the first-time observation of signal propagation inside one cell, whose conduction velocity is five times that of between neighboring cells. In Chapter Five, electrical signal propagation in 3D cardiac tissue constructs will be introduced. Our work presents the first-time recording of intracellular action potentials of cardiomyocytes in a 3D cardiac tissue. Also, conduction velocities in the 3D tissue were measured by the soft device.

Chapter 1. Introduction of cellular electrophysiology recording.

1.1 Introduction of Electrophysiology.

Electrophysiology is a very useful biophysical method for the study of electrical properties of cell membranes[1]. Understanding the function of cell membranes is significantly important in electrophysiology studies. The cell membrane consists of a fluid-crystalline phospholipid bilayer structure with various functional proteins embedded in it. The electrical properties of the cell membrane are attributed to ionic activities via a specific protein, called transfer proteins, which can either form channels/pores or carriers that can actively transport ions. The transmembrane ionic flow constitutes a membrane conductance change, thus mediating cellular functions.

The first bioelectrical phenomenon recorded is the confrontation with electrical shock from the electrical organ of certain fishes[2]. Later, we call this kind of fish electric ray or Torpedo torpedo. In ancient times, people used the fish for electro-therapy, such as treating headaches or gout. The birth of electrophysiology was marked by the experiment done by John Walsh, in which the discharge of an electric organ was made visible. There is an approximate two-hundred-year interval before an evolutional tool—the voltage clamp—was developed. New discoveries continuously came out showing that alternations of ion conductance modulate the action potential generation, which is a strong electrical spike generated by many influx ions into the cell body. The technique was further refined by the patch-clamp in 1976, which is still most widely applicable in research labs all over the world, shown in Figure 1. Using the patch-clamp, we can detect the ion currents through single channels. Also, modulations of the cell membrane potentials can be easily

conducted using the patch-clamp. In recent years, electrophysiology is helping the understanding of the cellular biophysical phenomenon and the treatments of heart and nervous system diseases, such as heart arrhythmia, stroke, Parkinson's disease, etc.

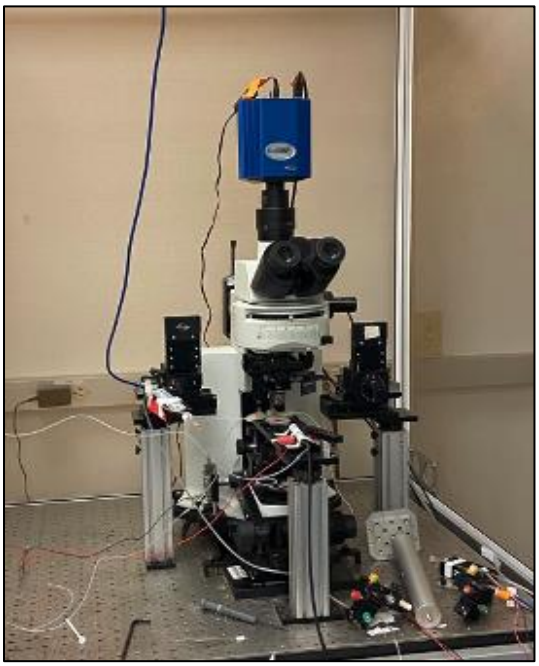

Figure 1. The patch-clamp platform widely used to study electrophysiology of single cells.

Electrophysiology has three obvious features. First, electrophysiology provides the most direct and sensitive measurement of ions flowing through ion channels in individual cells. The use of low-noise electronic signal acquisition and processing permits the recording of current passing through a single channel protein. It also requires the accurate control of the interaction positions of the sensor (e.g., glass pipette in the patch-clamp) with the certain ion channel on the cell membrane. Second, it allows for the membrane potential to be clamped (i.e., modulated) at specific voltages with precise temporal control during the ion-channel assay. Ion channel currents are measured under well-defined conditions, providing more specific and relevant information. For example, there are voltage sensitive ion channels on the cardiac muscle cell membranes, that are

open under a positive bias on the cell membranes. This characteristic of the cell membrane is a major mechanism of showing the large spike in an action potential. Third, kinetic responses of ion channels in the time resolution of tens of microseconds can be accurately determined. Owing to the high sampling rate of electronic sensing devices, it allows for the measurement of the intrinsic properties of ion channels, such as the time constants for channel opening, closing, and inactivation. No other technologies permit such detailed studies of ion channel kinetic behaviors.

Action potentials are observed in electrogenic cells such as cardiomyocytes or neurons. In Figure 2, when a very rapid opening of all the voltage-gated sodium channels is triggered by depolarization of the cell membrane. Such a series of events triggers a massive change in membrane voltage defining the action potential. In an action potential, there are discrete steps including depolarization, repolarization, and refractory period. The feature of each step has strong relationships to certain misfunction of the cell membrane, probably due to lack of or damage of the ion channels. In other words, lots of information can be read by the action potential shape.

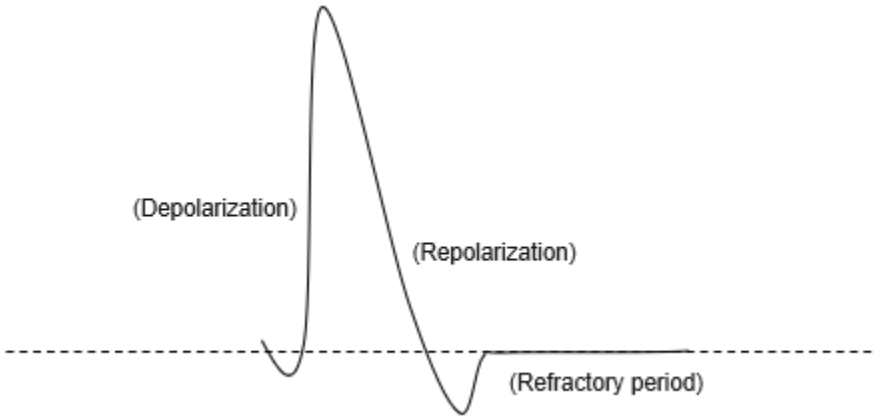

Figure 2. A typical action potential consisting of depolarization, repolarization, and a refractory period.

Tools for electrophysiology studies can be categorized into three parts: on the body surface, on tissue, and on the single cell. Recordings from the body surface is possible since the animal body, simply speaking, represents an electrolyte container. This study includes electrodermatography for cardiac resynchronization therapy, electrogastrography for electroshock, electrocochleography for electro-sleep therapy, electrocardiography for electronuraltherapy or electroacupuncture, electroencephalography for electrogymnastics, electroneurography for electrocoagulation, electrospinography, electrooculography, electroretinography, electronystagmography, electromyography for muscle stimulation and fatigue therapy. These biological or biomedical measurements provide vital information closely related to health conditions. Recording electrical signals from the tissue disclose more accurate information of electrically active cells or tissues, such as cardiac and brain slices, neuronal or cardiac cultures and retinal preparations. Extracellular field potentials can be detected on tissue surfaces. They are from cellular networks or cells in a tissue generating fast changes in their membrane potential. The information is a summation of signals from individual cells. Extracellular field potentials around cells can be detected by capacitive coupling between the cell membrane and an extracellular electrode close enough to the cell. One major advantage of extracellular field potential recording is its noninvasiveness to cells or tissues[3]. Recording electrical signals from single cells is fulfilled with the most powerful electrophysiological method, mostly for basic research, the voltage-clamp or the patch-clamp. At a given membrane potential allows the measurement and analysis of currents across the cell membrane that are mediated by specialized channels and carriers. The analysis of voltage dependencies forms the basis for most electrophysiological investigations. To

note, intracellular action potential has larger amplitude of nearly a hundred millivolts that can manifest subthreshold ion activities that cannot be obtained by extracellular signals.

1.2 Conventional Tools for Electrophysiology Study

A conventional tool for extracellular potentials sensing is the multi-electrode array (MEA). Cells can either be cultured on top of the device or attached to the device for sensing. There is a minimum cleft of ~10 nm between the cell membrane and the electrode, therefore, the acquired signals show small amplitude. In the electrical model, the cell membrane is regarded as a resistor capacitance pair. Thus, the intracellular signal gets distorted by this membrane RC component.

To read the intracellular membrane potentials, the voltage-clamp was first described in 1949 by Cole and modified and improved by Erwin Neher and Bert Sakmann in 1952. It was the prerequisite for the two milestones in modern electrophysiology: the description of excitability and the demonstration of single-channel events. The basic principle of the voltage-clamp is the feedback amplifier, which allows us to apply voltage pulses to the membrane and measure the potential- and time-dependent changes of current responses that flow across the membrane to the grounded bath (i.e., cell culture medium), and hence represent the membrane current[4]. The patch-clamp technique is a further development of the one-electrode voltage-clamp. The essential characteristic is an extremely high resistance formed by close contact between the pipette rim and cell surface reaching several giga ohms. In the past several decades, there have been lots of refinement on the modern or advanced patch-clamp platforms. Even so, the technique still has shortcomings. First, the technique requires extensive labor to use. A successful patch-clamping

costs hours to get. Second, the technique is skill demanding. Even for experienced electrophysiologists, it is challenging to accomplish a giga-ohm sealing. Third, the technique is extremely low throughput. Upon a successful patch-clamping, the signals that can be collected from the cell is limited, which is also because the technique is invasive to the targeted cell. Forth, the setup is cumbersome and very sensitive to any mechanical or electrical disturbance during the experiment[5]. To overcome these difficulties, advanced forms of the patch-clamps have been developed, such as automated glass pipette-based patch-clamping (Cyto Patch Chip, Apatchi-1, Flyscreen, RoboPatch, AutoPatch, Dynaflow), planar electrode (PatchPlate IonWorks HT, Seal Chip in PatchXpress, NPC-16), and automated, TEVCON Xenopus oocytes (OPusXpress, Robocyte)[6-10]. However, unfortunately, these novel patch-clamp platforms cannot tackle all of the four difficulties.

1.3 Electrophysiology Studies Promoted by Nanotechnology

Due to the rapid development of nanoscience and nanoengineering, there are lots of emerging technologies designed to couple with biological objects and obtain vital properties from them[11]. In electrophysiology studies, the nanotech-driven electronic devices show superior performance, including operational friendliness and ease, flexibility and conformal interacting with cells/tissues/organs, high-sensitivity recording due to high surface-to-volume ratio, less invasive intracellular action potential monitoring, chronic recording, simultaneous multi-site recording with higher spatial resolution, and multi-function achieved by the flexibly controllable device manufacturing by the bottom-up techniques[12]. One or combined of these characteristics

made nano-sized electronic devices available and proved to be a promising substitute to the laborious patch-clamping platforms.

There are lots of ways to classify these nano-electronic devices. First, by the materials of the devices, there are rigid and soft devices. Rigid devices employ hard materials such as silicon and metal nanowires that penetrate the tissues or cell membranes upon implementation. An obvious drawback of these rigid nanowires is the huge mechanical mismatch between the rigid devices and the soft biological tissues or cells. The implementation of these devices will result in severe physical invasiveness of the targets making the measurements inaccurate and short lifespan. On the contrary, soft devices use low-modulus materials such as polymers in their structures. The largely decreased mechanical mismatch between the devices and the soft targets makes the measurement more stable and reliable. Second, by the targets of these devices or recording activities, there are intracellular and extracellular devices. Intracellular devices can insert their sensing parts into the cell body, forming a one-on-one correspondence of the signal recording. The most common form of these intracellular devices is the long and thin nanowire or its variants such as nanotube. The nanowires can be synthesized by the top-down method (material etching) or the bottom-up method (chemical vapor deposition). Usually, the nanowire is fixed onto a polymer substrate that can be installed to a customized adaptor and connected to an external power source or data acquisition equipment. Intracellular sensing devices can intrude into the cell body and obtain internal membrane potential. Extracellular recording device records the local field potential or the action potential of single cells outside of the cell membrane. Therefore, the recorded signals are distorted or filtered by the resistor-capacitor pair constituted by the cell membrane. In

conclusion, the intracellular signals would carry more detailed electrophysiological information than the extracellular recordings. Third, by working principles, there are passive and active sensing devices. A passive device represents a conductive or capacitive wire/pad/structure that can transmit electrophysiological signals to the acquisition devices. Because the device is a resistor in the measurement circuit, its resistance would influence the output signal to the acquisition equipment. When the passive device is long and thin, especially in nanoscale, the resistance would play a critical role in the circuit and show the drastically decreased amplitude of the recorded signals. On the contrary, a typical active device does not suffer attenuated recordings. It is composed of a semiconductive material forming a transistor physical structure that can actively record electrical potential change around itself. Because of all the feature, active device can be miniaturized and maintain high sensitivity, and it becomes the most promising type of device for future electrophysiological research.

1.4 Current Research Using Active Sensors.

Passive bio-interfaces, when made rigid, have been used in clinics for a long time, mostly because of their robustness and simple manufacturing process. Rigid electrophysiological recording tools were first developed by micro/nano fabrication techniques, represented by Utah array and Michigan array[13-15]. These tools are designed to interact with brain tissues and monitor brain activities in vivo, both for neuroscience study and brain disease therapy. When the fabrication techniques with polymeric materials became more mature, flexibility of the neural probes turned feasible providing softer contacts with brain or cardiac tissues that decrease the invasiveness

during signal recording. These probes use epoxy-based or polyimide-based materials and have sharp needle-like shapes that can penetrate into the thick brain or other tissue during implementation. Some flexible bio-interfaces are manufactured as a planar configuration that can be placed on the cortical surface achieving chronic cortical or cardiac recording[16-21]. Attributing to the flexibility even stretchability of the novel planar electrode arrays, a conformal contact between the brain surface and devices is formed[22-24]. Passive devices for intracellular action potential are designed based on two platforms that are MEA and patch-clamp. Therefore, one kind of such interface is using nanosized arrayed structures, such as nanowires or nanobumps, to interface and internalize with the cells achieving intracellular action potential sensing[25-32]. Another kind is to replace the glass pipette used in the patch-clamp technique with nanowires. Importantly, a poration process is necessary to realize intracellular sensing configuration. The poration of the cell membrane can be made by chemical, mechanical force, or electrical stimulus.

Again, the intrinsic shortcomings of the passive interfaces, including high access electrical impedance, no full-amplitude signal recording capability, and low sensitivity, impede the further development of this kind of bio-interfaces. To overcome them, specifically to decrease the access impedance of the bio-interface, further, to obtain more information from biological systems, a lot of active devices were brought up based on the transistor format, such as field-effect transistors. Silicon is the most widely applied semiconductive material in building up these interfaces. However, other semiconductive materials, such as carbon-based low dimension materials, carbon nanotube and graphene, are also studied[33]. For extracellular sensing, several soft, thin, and mesh-like silicon nanowire-based bio-interfaces were developed[14,34]. These tools were either injected

into brain tissue or incorporate with cell cultures mapping their action potentials in a 3D configuration[35-40]. Such 3D designs satisfy the requirement of large area brain mapping. Intracellular action potential recording is always more interesting because it can elucidate more subthreshold physiological signals. First, a hollow nanowire made of oxide material interfaces and patches the cell membrane and propagate the acquire potential change via its tube filled with extracellular solution all the way to the gate terminal of a FET[41-43]. Second, a FET nanowire interfaces the cell membrane directly and obtains the transmembrane potential at the local position[44,45].

1.5 Remained Challenges in Active Sensors for Cellular Recording.

Even though the active bio-interfaces show excellent features in future electrophysiological applications, there are still some difficulties to overcome. First, the active bio-interface has more electronic leads and greater complexity than the passive counterpart. Secord, the large leakage current is seen due to the imperfections on the device. Third, using the current bottom-up fabrication method, it is difficult to increase the number of intracellular sensors in one tool/device.

In the general electrophysiology research field, these challenges are also existing, even after the application of these novel nanoscience-driving bio-interfaces. First, we have seen that these nano-sensors show the excellent capability of sensing action potentials, especially those active intracellular sensors, which can obtain full amplitude recording. However, the signals such as subthreshold synaptic potentials, membrane oscillations have not been sensed by these nano-devices. The limitation is due to the inherently high impedance of the nano-pillar/wire devices and

the inherent high noise level of the nano-FET sensors. Second, the present intracellular tools only have one to four active FET probes that are insufficient for large-scale sensing or study of intercellular communication in cellular networks. It is due to the complexity of the bottom-up fabrication technique of these sensors. Third, the nano-pillars/wires can sense action potentials intracellularly under the condition of electroporation. It is a transient process that makes contact and interfaces unstable during the test. The nano-FETs are interfaced with the cells by mechanically pressing and targeting. It makes the physical contact unstable.

1.6 Conclusion.

In this chapter, we have discussed current research and challenges in the bio-interfaces for electrophysiological signals recording of human body surface, tissue surface, and single cell. Even though promising developments have been achieved in nanoscience-driving tools in a short period, critical problems such as the low sensitivity, scalability, and large mechanical modulus of the tool are still unsolved, which suggests that more efforts are needed to address those remaining problems to sweep the way for better application on such tools.

Chapter 2. Engineering a Soft Sensing Platform Using Compressive Buckling Technique

2.1 Introduction of Compressive Buckling Technique

Buckling is a scientific term used by mechanists to describe an unstable state of a mechanical structure when fractures occur. It is usually characterized by a sudden sideways deflection of a structural member. For example, when a column is under a concentric axial load, increasing the load to a certain value, the column exhibits a deformation or bending. This deformation is defined as buckling. In architecture, we would like to avoid any buckling by an overload on blocks or beams of the building structure. When we see this controlled deformation, because there is a threshold for buckling to happen, from a positive perspective, we can make use of it to realize the transformation from a two-dimensional (2D) structure to a three-dimensional (3D) structure. In the real world, pop-up books also borrow this bucking idea to make a vivid structure out of a planar book.

By the inspiration of the phenomenon, a series of microstructures were introduced[46]. To apply the compression on the 2D structure, researchers transferred the 2D structure, called precursor, onto a pre-stretched/strained elastomeric substrate. Some parts of the 2D structure were bonded to the substrate, and the rest of the structure was freestanding. When the pre-strain in the elastomer substrate was released, a compressive force was applied to the 2D structure. Once the force is large enough, the structure will have an out-of-plane deformation and turn into 3D.

The compressive buckling technique is simple to generate 3D structures. We can use functional materials in the structure to fabricate functional devices. For example, an energy

harvester or mechano-vibrators can be made using piezo-electric materials in the structure[47,48]. Light-emission diode and photodetectors were made using semiconductive materials[49-53]. Pressure sensors[54], integrated circuit integration[55], electronic scaffolds[56], micro-robots[56], tunable inductors[57,58], capacitors[49], FETs[50], electrically antennas[59,60], etc. have been demonstrated using the compressive buckling techniques.

2.2 Design of An FET Array for Intracellular Electrophysiology Recording

The 3D FET array was constructed using a compressive buckling technique.

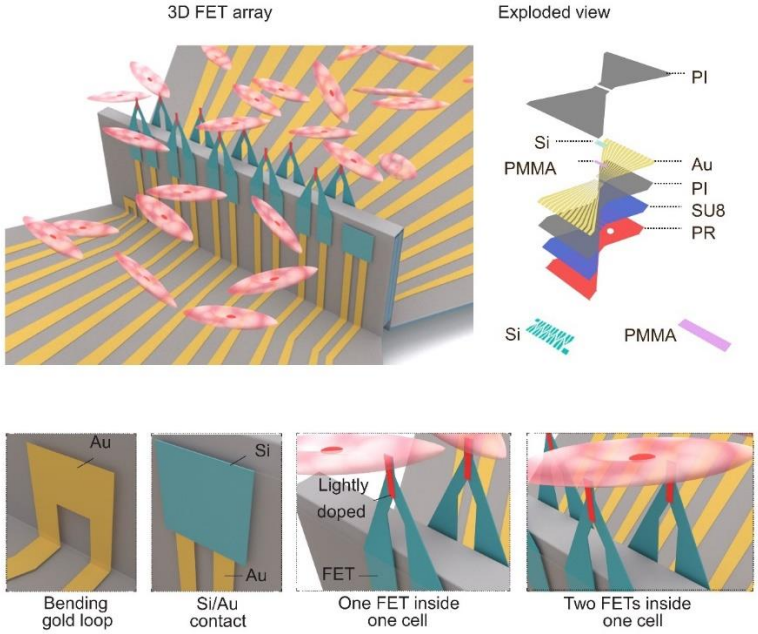

Figure 3. 3D FET arrays by compressive buckling.
Schematic images showing a 10-FET array interfacing with a group of cardiomyocytes. An exploded view at the top right illustrates a multilayered design of the FET array. Inset images at the bottom showing, from left to right, an Au loop for checking the electrical conductivity after the device buckles, an Au/Si bilayer for probing the quality of electrical contact after the device is soaked in an acidic solution, one FET recording intracellular signals, and two FETs in the same cell to study intracellular signal conductions. The red area on each FET denotes the lightly doped channel.

First, a multi-layered two-dimensional (2D) precursor was fabricated using standard micro/nanofabrication (Figure 3 left).

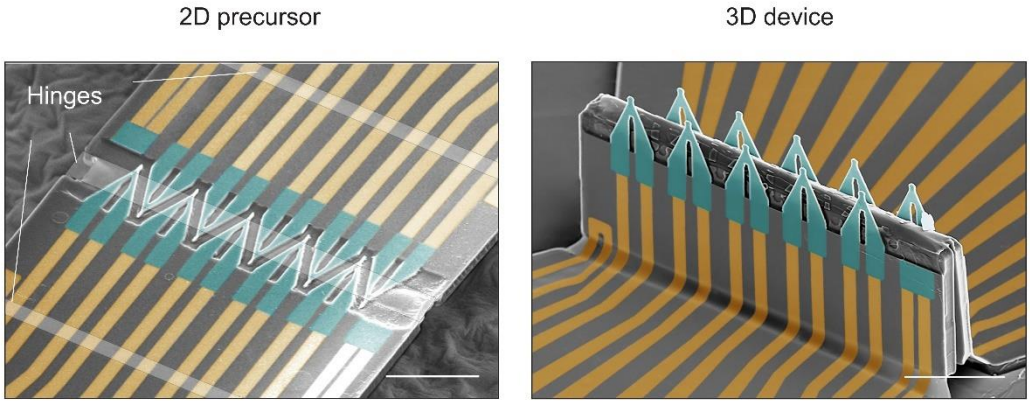

Figure 4. Characterization of the 2D and 3D device.
False-colored SEM images showing the transformation from a 2D precursor (left) to a 3D 10-FET array (right). Each FET has a tapering tip (5 μm long and 1~2 μm wide). Scale bars: 50 μm.

The precursor was transferred, and selected regions were bonded onto a prestrained elastomer substrate, after which the prestrain of the elastomer substrate was released.

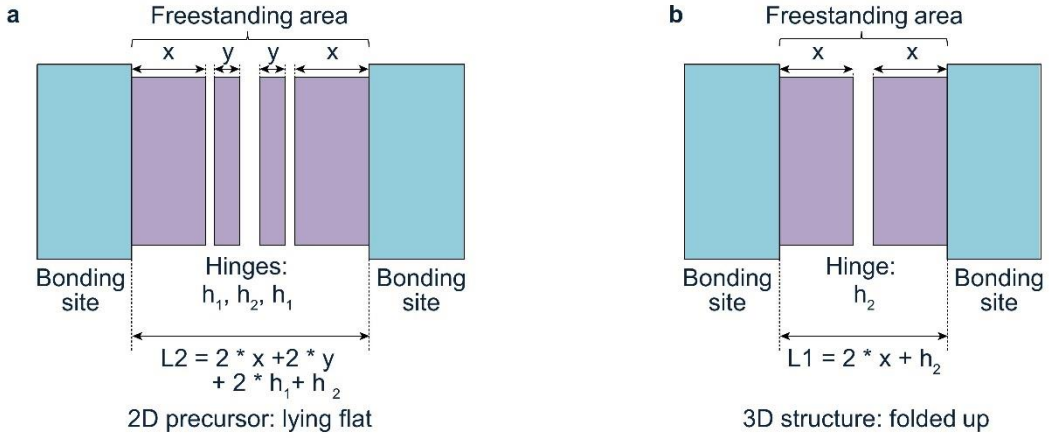

Figure 5. Structural design of the arrayed FETs.
Schematics showing the design principle of the 2D precursor of a 10-FET array. The applied prestrain on the dragon skin elastomer is defined by (L2 - L1)/L1.

The compression causes the 2D precursor to buckle at predesigned hinge locations to form a 3D shape (Figure 4 right).

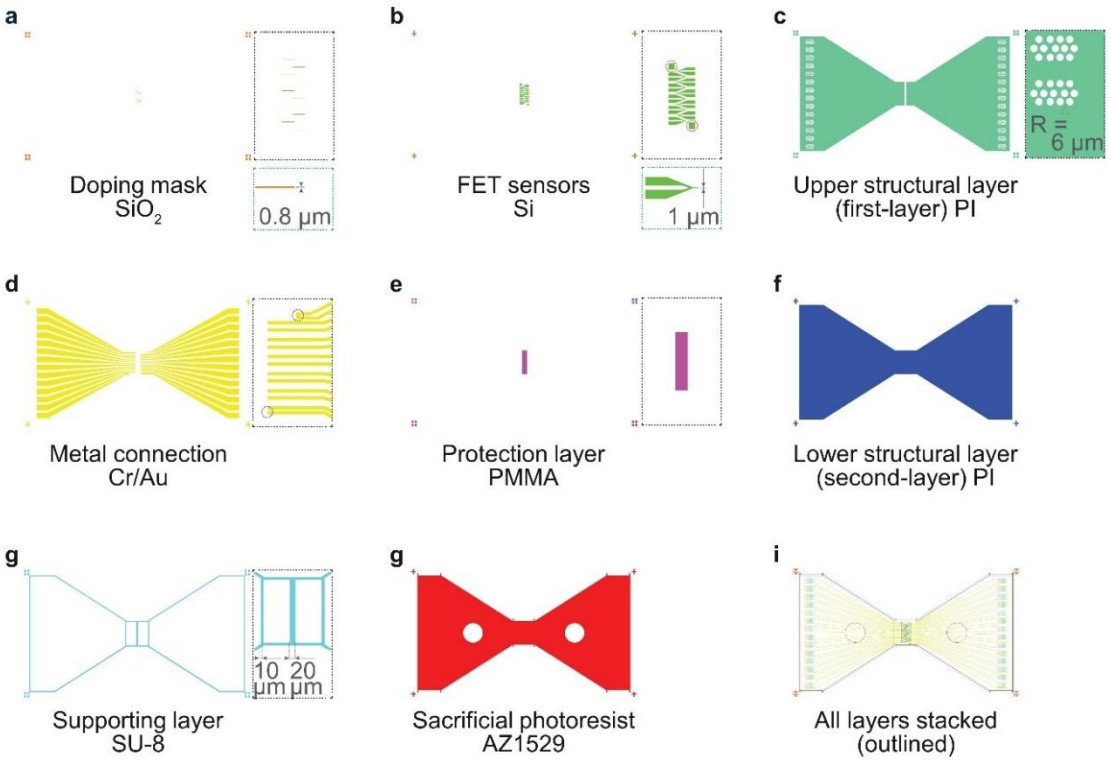

Figure 6. The CAD designs of the FETs.

The CAD designs of the FETs showing the unique features of every layer of the device. Each layer has four alignment markers at corners for photolithography. **a,** The doping line is 0.8 μm wide by photolithography. **b,** The sensors' tips are 1–2 μm wide, which can provide high sensitivity and spatial resolution while minimizing invasiveness to the cells and forming tight sealings during measurements. Two square pads highlighted by the red dashed circles in the inset image serve to check the quality of metal connections with silicon after soaking in the acid solution for several hours. **c,** The holes shown in the inset image are designed to expose the metal connections for bonding with external connective wires (e.g., ACF cables). **d,** In the inset image, the black dashed circle on the top indicates a metal loop that is used for checking connections after compressive buckling. The black dashed circle at the bottom are the wires connecting to the square silicon pad in (**b**). **e,** PMMA holds the ten FETs together during the fabrication and gets removed during compressive buckling. (**f**) The second PI layer has the same layout as the first one. **g,** In this design, the middle hinge (h_2) is 20 μm wide. **h,** The shape of the bonding site can be circular, square, or rectangular. A circular shape in this case makes the compressive strain more evenly distributed on the bonding area and prevents delamination of the device from the elastomer substrate.

To verify the electrical functions of the device before and after the buckling, dummy structures consisting of Au and Si/Au are processed in parallel and used as checkpoints (bottom insets in Figure 3).

The 3D structure is coated with a bilayer of Parylene C and SiO_2 for electrical insulation and hydrophilic surface functionalization. The compressive buckling technique enables us to fabricate arrays at various scales, with different materials, layouts, dimensions, and geometries. The 3D geometry allows the FET to penetrate the cell membrane and record low-amplitude sub-threshold signals inside the cell. The small sensor tip (1~2 μm) penetrates the cell membrane with minimal invasiveness.

The device layout is designed to allow interfacing with multiple cells and even having two FETs in the same cell (Figure 3). To make the entire device mechanically robust, we have carried out theoretical and experimental studies to optimize the materials and their dimensions, such as using low molecular weight poly(methyl methacrylate) (PMMA) and thick acid-resistant photoresist as sacrificial layers.

2.3 Fabrication of the Soft FET Array.

Fabrication of the stretchable 3D FET array involved standard micro/nanofabrication techniques, as well as a newly designed transfer printing technique and the unique compressive buckling technique (Figure 7).

The 3D FET has a functional silicon transistor connected with gold conduction electrodes, which are sandwiched by two polyimide (PI) structure layers.

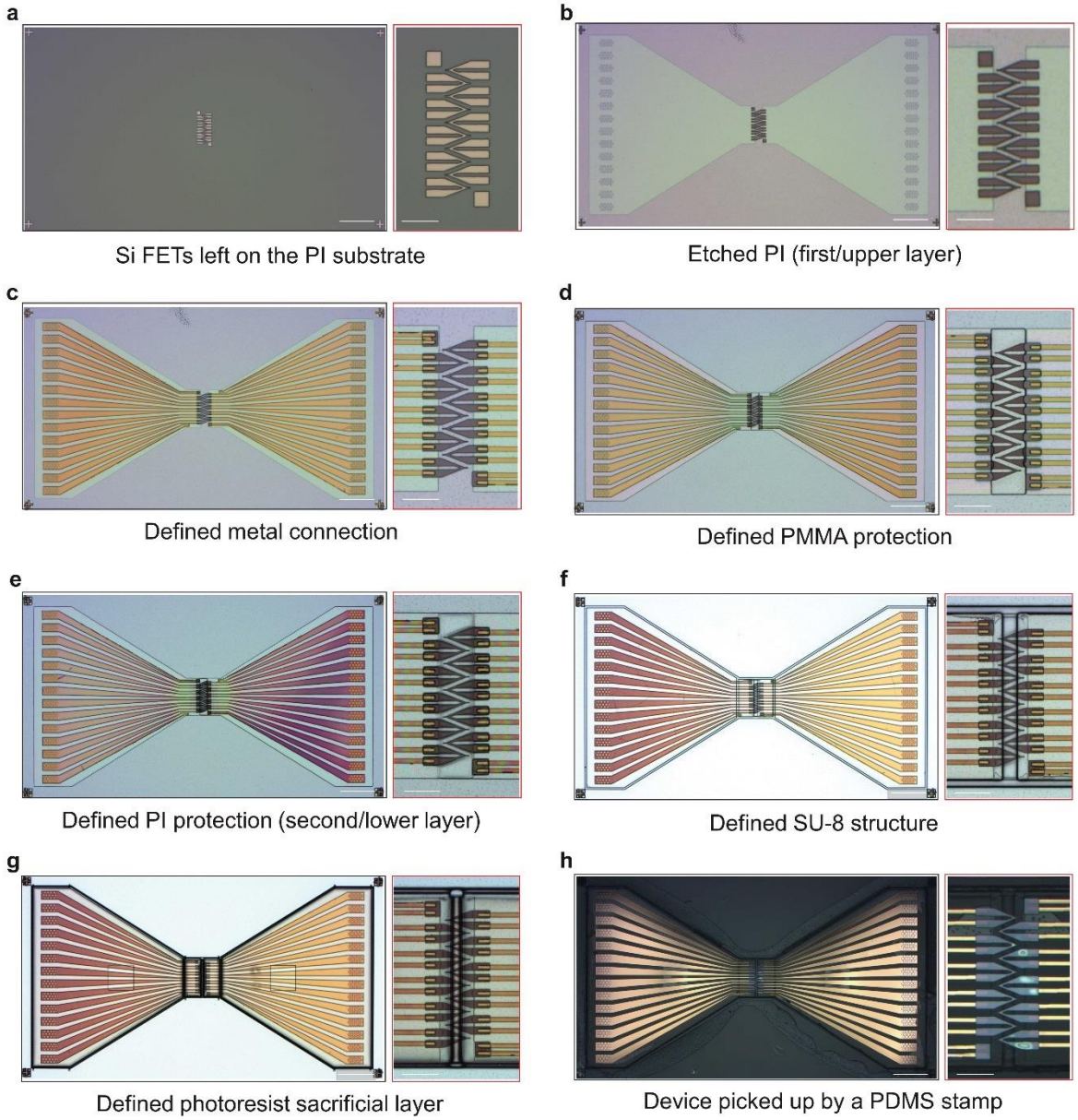

Figure 7. Optical microscopical images illustrating the fabrication steps of the arrayed FETs. **a**, The FETs have been doped by spin-on diffusants on the SOI wafer. **b**, The sensors are transfer-printed to a temporary substrate coated with PI (first/upper layer). **c-g**, Multi-layered polymers and metal are formed in steps of spin coating, sputtering, and photolithography on the temporary substrate. **h**, Finally, the multi-layered 2D device is transferred to the PDMS stamp. The scale bars on each panel, left: 200 μm, right: 50 μm.

A poly(methyl methacrylate) (PMMA) layer is holding and protecting the FETs during the sequential fabrication process. It would get removed by acetone before releasing the prestrain and

applying the compressive force. A relatively rigid SU-8 layer serves as the mechanical support of the whole device. A photoresist layer defines the bonding sites of the SU-8 to the prestrained elastomeric substrate.

The device was fabricated on a silicon-on-insulation (SOI) wafer (University wafers, device layer: 1.5 μm, oxide layer: 3 μm, carrier layer: 550 μm), shown in Figure 8. SOI samples were diced by a diamond dicing machine and cleaned thoroughly in an RCA (Radio Corporation of America) clean process to remove all organic contaminations, particles, and SiO_2 on the wafer surface (Mixture solution is Ammonia hydroxide (29%): hydrogen peroxide (30%): deionized (DI) water = 1: 1: 5 in volume; The solution was heated to 140 °C, and the samples were boiled for 15 min; The oxide on the silicon surface got removed by dipping the samples in buffered oxide etchant (BOE) 6:1 for 2–3 seconds followed by DI water rinsing).

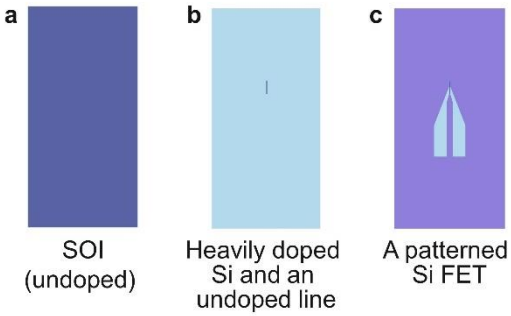

Figure 8. Silicon doping on SOI.
The FET's drain, source, and gate regions are determined on an n-type SOI wafer by doping. First, the undoped region (i.e., the region with only the background doping from the wafer) is coated by a layer of SiO_2 as the barrier for spin-on dopants from diffusing into the silicon substrate. Second, the FET shape is defined by photolithography and reactive ion etching.

Next, the 1.5 μm silicon was thinned down to 400 nm by dry etching (inductively coupled plasma–reactive ion etching (ICP-RIE); RIE: 30 W, ICP: 1,200 W, 18.0 mTorr, 20 °C, 25.0 sccm

SF_6, 50.0 sccm C_4F_8, 120–180 s). Another dry etching process (ICP-RIE; RIE: 200 W, ICP: 2,000 W, 50.0 mTorr, 15 °C, 50 sccm O_2, 1 min) removed the induced C_4F_8 residue coated on the silicon surface.

The sample was RCA cleaned again to remove any oxide or contaminants on the surface. Alignment markers at the four corners of the sample were defined by photolithography (photoresist NR-3000PY: spin-casting at 4,000 r.p.m. for 60 s, baking on a hotplate at 150 °C for 60 s, UV irradiance at 220 $mJ \cdot cm^{-2}$, post-exposure baking at 100 °C for 60 s, and developing for ~20 s with developer RD6) and dry etching (ICP-RIE: 30 W, ICP: 1,200 W, 18.0 mTorr, 20 °C, 25.0 sccm SF_6, 50.0 sccm C_4F_8, 60 s). The silicon on the alignment markers' positions was thinner than the other areas, providing optical contrast while aligning the photomask in subsequent fabrication steps. Next, SiO_2 doping mask was fabricated by depositing a uniform 100 nm or 300 nm thick oxide layer on the sample surface using plasma-enhanced chemical vapor deposition (PECVD; RF power: 20 W, 1,000 mTorr, 350 °C, 117.0 sccm SiH_4, 710.0 sccm N_2O, 246 s), and the doping mask patterns were defined by photolithography (photoresist AZ 1505: spin-casting at 4,000 r.p.m. for 45 s, baking on a hotplate at 105 °C for 90 s, UV irradiance at 30 $mJ \cdot cm^{-2}$, and developing for ~15 s with developer AZ 300 MIF) and dry etching SiO_2 (RIE: 150 W, 30.0 mTorr, 20 °C, 25.0 sccm Ar, 25.0 sccm CHF3, 720 s).

The dopants were coated on the sample surface (spin-on diffusants, B151 or P509: spin-casting at 3,000 r.p.m. for 10 s, soft baking on a hotplate at 200 °C for 15 min) and annealed in a rapid thermal annealing furnace (RTA furnace: 950 °C for certain time). During sample annealing, the dopants would diffuse into the silicon dioxide mask instead of the underneath silicon, forming

the selectively undoped regions. Then, the doping mask and the excessive dopants got removed in BOE for ~15 min. After that, silicon probe structures were defined by photolithography (photoresist AZ 1505: spin-casting at 4,000 r.p.m. for 45 s, baking on a hotplate at 105 °C for 90 s, UV irradiance at 30 $mJ \cdot cm^{-2}$, and developing for ~15 s with developer AZ 300 MIF) and silicon dry etching (RIE: 30 W, ICP: 1,200 W, 18.0 mTorr, 20 °C, 25.0 sccm SF_6, 50.0 sccm C_4F_8, 60 s) and a follow-up RCA clean to obtain contamination-free silicon samples for FETs.

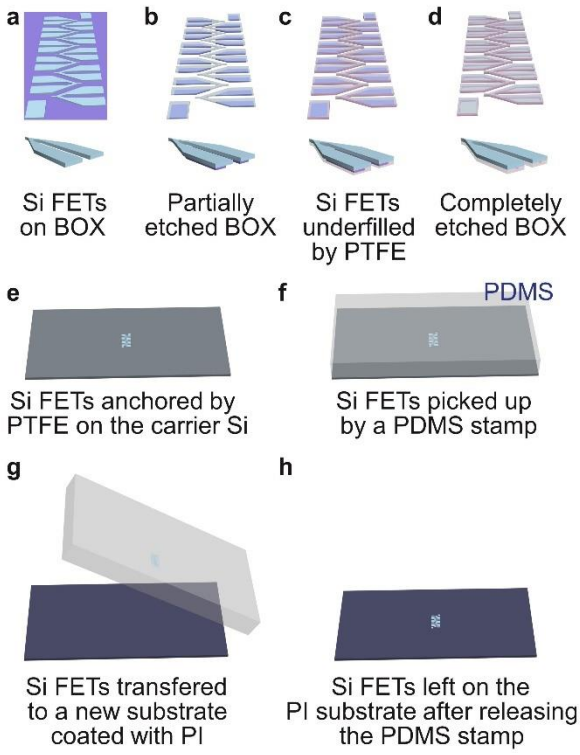

Figure 9. 2D FET fabrication on SOI.
The FETs are firstly anchored to the substrate by PTFE, and then are transferred using a PDMS stamp to a temporary 2D substrate coated with PI.

It was notable that offsets in doping regions caused by misalignment of photolithography and/or non-uniform doping induced by uneven spin-coating on the silicon surfaces would introduce variations in the measured conductance and transconductance of the FETs.

The FET had a lightly doped conduction channel in the middle and two heavily doped source and drain terminals on the sides. We characterized the doping concentration distribution by using an atomic force microscope coupled with the scanning microwave microscopy function. The height difference between the lightly doped middle region and its two sides was due to the RIE etching of the SiO_2 when defining the doping mask that covered the middle part.

To dry etch the SiO_2, CHF_3 gas was applied, which could also react with Si at a selectivity of 3:1. If there was any over-etching, the exposed Si would also be etched to form a small step edge compared to the middle region protected by photoresist during the dry etching. Over-etching was preferred over under-etching because we wanted to ensure the silicon is completely exposed before casting spin-on-dopants to fulfill successful doping.

The 3 μm oxide layer (buried oxide: BOX) in the SOI was wet etched (hydrofluoric acid (HF) 49%: 140–160 s) to undercut the FET structures and also left sufficient oxide residue to connect the FET structures to the carrier wafer. A layer of PTFE (polytetrafluoroethylene) (AF: PTFE (Amorphous Fluoroplastics Solution) was deposited: spin-casting at 1,000 r.p.m. for 60 s, baking on a hotplate sequentially at 110 °C for 5–10 min, 245 °C for 5 min, and 330 °C for 15 min) on the FET surfaces, and dry etched (RIE; 80 W, 50.0 mTorr, 35–40 °C, 50.0 sccm O_2, 10 s) to expose the silicon surface. As a result, the previous undercut portion of SiO_2 was filled with PTFE. Then, the rest of the SiO_2 was completely etched off by placing the samples in HF (49%) for 2–3 hours.

A temporary 2D substrate was needed to connect and encapsulate these FET structures in functional devices. The temporary substrate was prepared by sequentially coating Al (sputtering;

200 W, 3.0 mTorr, 10 sccm Ar, 5 min, ~60 nm), PMMA (495 A11: spin-casting at 4,000 r.p.m. for 60 s, baking on a hotplate at 180 °C for 1 min, ~800 nm), and SiO_2 (plasma-enhanced chemical vapor deposition (PECVD); RF power: 20 W, 1,000 mTorr, 350 °C, 117.0 sccm SiH_4, 710.0 sccm N2O, 82 s, ~100 nm). Here, the Al layer served as the sacrificial materials to be later etched away in hydrochloric acid (HCl, 37–38%) to release the FET device from the substrate. The PMMA and SiO_2 dual layers acted as the protection materials to firstly avoid HCl from attacking the metal connections at the Au/Cr/Si interfaces, and to secondly prevent chemicals in subsequent steps from over-etching the PI or PMMA.

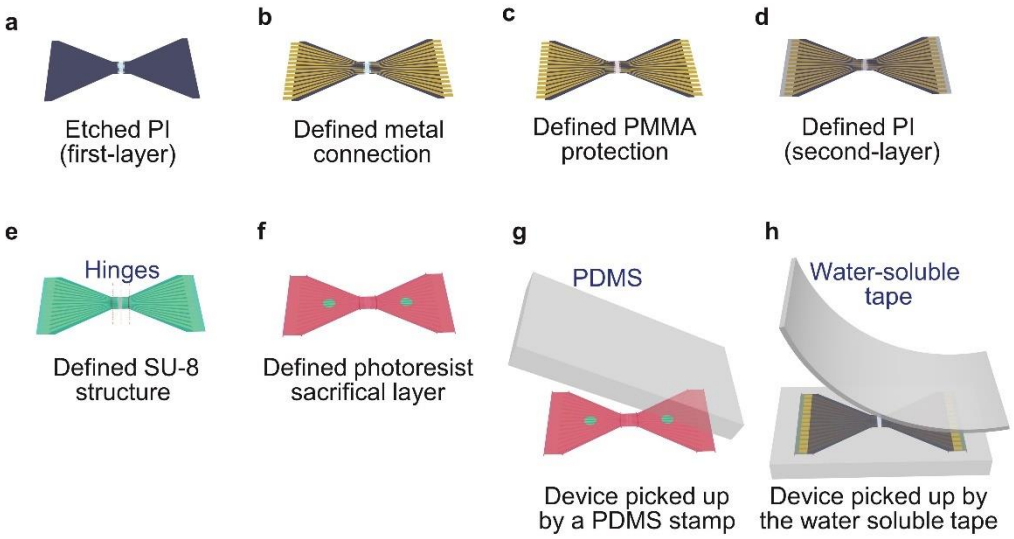

Figure 10. FET fabrication on a temporary 2D substrate.
Multi-layered polymers and metal are coated and patterned on the temporary substrate. Finally, the layered device is transferred to a PDMS stamp and picked up by a water-soluble tape.

The sample prepared in 1.2.1 was deposited with an anti-adhesive C_4F_8 layer (RIE: 5 W, ICP: 500 W, 18.0 mTorr, 20 °C, 10.0 sccm C_4F_8, 120 s) to reduce the adhesion between the silicon device and the transfer-printing stamp. A polydimethylsiloxane (PDMS; base: curing agent = 4:1 in weight ratio) stamp was used to press on the FET structures and quickly pick them up from the

SOI carrier wafer. Dry etching (RIE: 80 W, 50.0 mTorr, 20 °C, 50.0 sccm O_2, 420 s) the picked-up silicon surface to completely remove all of the PTFE underneath the FETs and to activate the silicon surface. Next, PI (2545; spin-casting at 6,000 r.p.m. for 60 s, baking on a hotplate at 100 °C for 20 s, ~1.6 μm) was coated on the prepared temporary substrate as described in 1.2.2. At the time the PI layer was baked for 20 s, we pressed the PDMS stamp with the activated FET surface contacting the PI and held it on the hotplate for 1 min before slowly releasing the PDMS stamp from the substrate. Then the FET structures were successfully transfer-printed to the temporary substrate.

The C_4F_8 layer left on FET surfaces got removed by dry etching (RIE: 80 W, 50.0 mTorr, 35–40 °C, 50.0 sccm O_2, 10 s). Then we fully cured the PI layer (hard baking on a hotplate; 250 °C, 60 min). Its shape was determined by photolithography (photoresist AZ 1529: spin-casting at 4,000 r.p.m. for 45 s, baking on a hotplate at 95 °C for 120 s, UV irradiance at 350 $mJ \cdot cm^{-2}$, and developing for ~40 s with developer AZ 300 MIF) and dry etching (RIE: 80 W, 50.0 mTorr, 35–40 °C, 40.0 sccm O_2, 10 sccm CF4, 300 s).

A lift-off process was used to define the metal patterns for connecting the FETs by photolithography (photoresist NR-3000PY: spin-casting at 4,000 r.p.m. for 60 s, baking on a hotplate at 150 °C for 60 s, UV irradiance at 220 $mJ \cdot cm^{-2}$, post-exposure baking at 100 °C for 60 s, and developing for ~20 s with developer RD6) and sputtering (chromium: 200 W, 3.0 mTorr, 5 sccm Ar, 30 s, ~5 nm; gold: 200 W, 3.0 mTorr, 5 sccm Ar, 5 min, ~100 nm). The metallization was finalized after the samples were soaked in acetone for 15 min. Moisture induced in the lift-off process got removed when the samples were baked in a vacuum oven at 100 °C for 10 min.

A PMMA layer was coated on the FETs for dual purposes: to protect the FETs during the following fabrication process and to serve as a sacrificial layer to release the FETs from the PI layer during the compressive buckling. Because PMMA is not photo-patternable by UV light in photolithography, a combination of photolithography and dry etching process was employed to pattern the PMMA layer. Given that PMMA is dissolvable in organic solvents such as acetone and NMP that would be used to remove the photoresist after dry etching, we coated a thin layer of PI on the PMMA before casting the photoresist. Notably, the PI is also photo-patternable and dissolvable in basic developers such as AZ 300 MIF but is resistant to acetone. Herein, sequential coating of PMMA (495 A11: spin-casting at 2,000 r.p.m. for 60 s, baking on a hotplate at 180 °C for 1 min, ~1,250 nm) and PI (PI2545/NMP = 2:1 in volume; spin-casting at 3,000 r.p.m. for 60 s, baking on a hotplate at 150 °C for 1 min, ~624 nm) followed by photolithography (photoresist AZ 1512: spin-casting at 4,000 r.p.m. for 60 s, baking on a hotplate at 95 °C for 60 s, UV irradiance at 120 $mJ \cdot cm^{-2}$, and developing for ~12 s with developer AZ 300 MIF) and dry etching (RIE: 80 W, 50.0 mTorr, 35–40 °C 50.0 sccm O_2, 150 s) defined the PMMA structure. The photoresist and PI on top of the PMMA got removed by acetone and developer AZ 300 MIF, respectively. Similarly, moisture was removed in the vacuum oven (100 °C, 5 min).

An adhesion promoter for PI (VM651/DI water = 1:50 in volume; spin-casting at 3,000 r.p.m. for 60 s, baking on a hotplate at 100 °C for 1 min) was cast before a second PI layer (PI2545; spin-casting at 1,500 r.p.m. for 60 s, baking on a hotplate at 150 °C for 1 min, ~4,500 nm) was formed to sandwich the FET sensors and the PMMA. Its pattern was established by photolithography (photoresist AZ 1529: spin-casting at 4,000 r.p.m. for 45 s, baking on a hotplate

at 95 °C for 120 s, UV irradiance at 350 mJ·cm^{-2}, and developing for ~40 s with developer AZ 300 MIF) and dry etching (RIE: 80 W, 50.0 mTorr, 35–40 °C, 50.0 sccm O_2, 300 s). The PI was fully cured after baking at 250 °C on a hotplate for 1 hour.

A relatively rigid and thick SU-8 layer provided structural support to the device. The second PI layer was activated by oxygen plasma (RIE: 50 W, 50.0 mTorr, 35–40 °C, 50.0 sccm O_2, 10 s) to bond with the SU-8 and prevent any delamination that might occur in the multi-layered device. Photolithography (SU-8 2010: spin-casting at 4,000 r.p.m. for 30 s, baking on a hotplate at 95 °C for 150 s, UV irradiance at 140 mJ·cm^{-2}, post-exposure baking at 95 °C for 210 s, and developing for ~140 s with SU-8 developer). Hard baking (100 °C on a hotplate, 1 hour) fully crosslinked the polymer chains of the SU-8.

A photoresist layer served as the sacrificial material for releasing the non-bonded areas of the device during the compressive buckling. To fabricate such a layer, the SU-8 surface was activated (RIE: 50 W, 50.0 mTorr, 35–40 °C, 50.0 sccm O_2, 30 s) before coating a photoresist layer followed by photolithography (photoresist AZ 1529: spin-casting at 4,000 r.p.m. for 45 s, baking on a hotplate at 95 °C for 120 s, UV irradiance at 350 mJ·cm^{-2}, and developing for ~40 s with developer AZ 300 MIF).

The device had a stack of layers and was attached to the temporary substrate during the fabrication processes as described above. To free the multi-layered device from the temporary substrate, the Al layer was etched in HCl fume evaporated from HCl solution (37–38%) in Figure 11. After 12-hour etching, the Al was mostly gone, but the device was still loosely anchored on the

substrate by the photoresist pattern and could be released from the substrate by the mechanical force of the stamp.

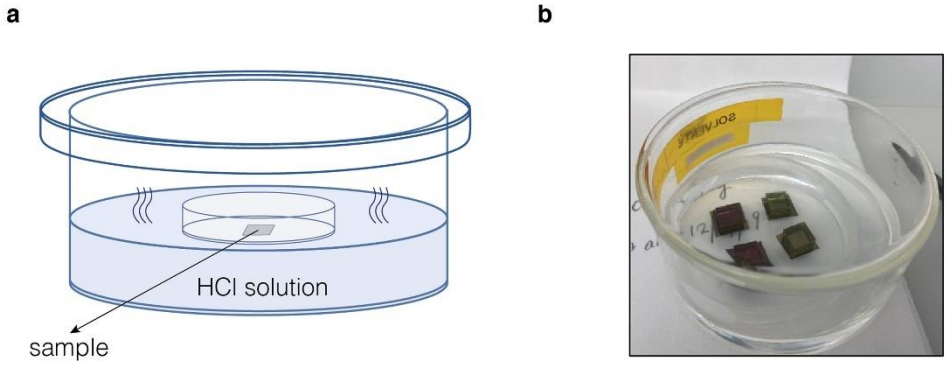

Figure 11. Sacrificial aluminum removal using HCl fume.
a, A sample was placed in a glass bowl that is floating on the hydrochloric acid solution. The large bowl has a lid to prevent the evaporated HCl fume from escaping. **b,** A photo of four samples being etched by the HCl fume.

A PDMS stamp picked up the device from the substrate. A cellulose-based, water-soluble tape allowed retrieval of the device from the PDMS stamp. Next, a strip of elastomer (Dragon Skin) was placed and prestrained on a uniaxial stretcher. The device and the dragon skin surfaces were treated in ultraviolet-induced ozone (UVO) cleaner, with the UV lamp ~1 cm apart from their surfaces, for 10 minutes. The device/tape was transferred on the UVO-treated elastomer surface with the press. The bonded structure was then baked in a convection oven at 80 °C for 10 min.

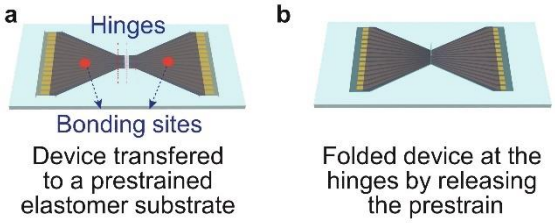

Figure 12. Buckling up the 2D precursor structure on an elastomer substrate.
The FET array is transferred to a prestrained elastomer substrate and selectively bonded at the two pre-designed bonding sites. When the prestrain releases, the 2D FET array gets compressed and buckled up to form 3D geometries.

DI water and acetone removed the water-soluble tape and the PMMA and photoresist layers in the device, respectively. The selectively bonded sites were located at the middle places of the SU-8. When the prestrain in the elastomer substrate was slowly released, the 2D structure transformed to the 3D configuration gradually. Finally, the entire device was rinsed with BOE and DI water to remove any oxide residues adhered to the device.

Before interfacing with cells, first, the entire device was wired using anisotropic conductive film (ACF) cables, which were bonded to the backend flat printed circuit cable (FPC) connector board (by aligning and pressing the cable on the tin leads with heating at 180 °C for 10 s). Second, the device was coated by a bilayer of Parylene C (1 g) and SiO_2 (sputtering; 200 W, 3.0 mTorr, 50 sccm Ar, 10 min). Parylene C was used to protect the silicon FET from dissolving in the solution. SiO_2 was used to generate a hydrophilic surface of the FET for binding with phospholipids. The insulation layer was vital to maintain the FET's high sensitivity and material stability during the measurement. The device was soaked in 70% ethanol for half an hour and then treated by UV for 1 hour for sterilization.

To precisely control the thickness of each layer in the FET device, we performed experiments to find the relationship between the film thickness and spin rate of the spinner, shown in Figure 13. The thickness was measured using the Daktek profiler. Each thickness was measured from five different samples of the same spin rate and soft bake time. Variations were marked by the error bars in the plot. With a higher spin rate, the film would become thinner. However, there is a minimum thickness of each photoresist precursor, which is determined by the concentration of the solids in the solution.

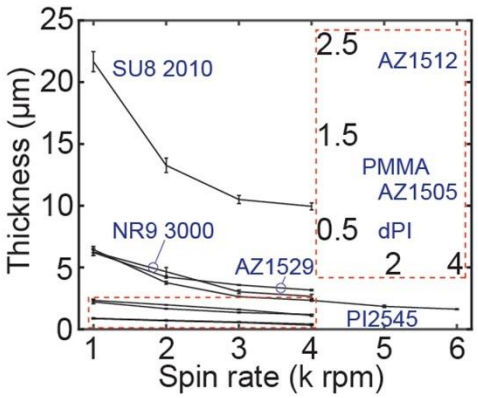

Figure 13. Relationship between photoresist thickness and spin rate during spin-coating.
The thickness of each material was measured after soft bake. The error bar was determined from measurements from five different samples. The thickness was measured using the Daktek profiler.

The fabrication processes introduced above include several times dry etching. To have precise control of the etching time, we tested the etching rate of AZ photoresist, SU-8 photoresist, PMMA, and PI, shown in Figure 14.

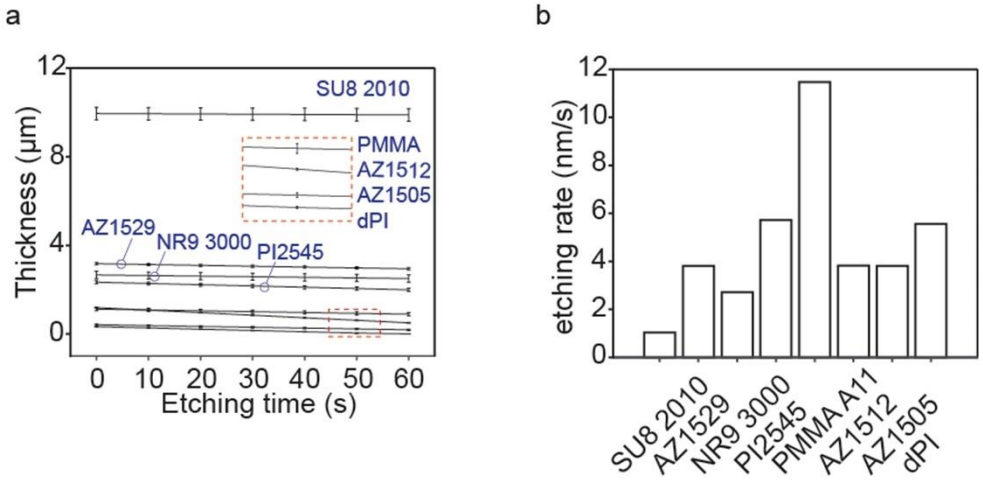

Figure 14. Testing of dry etching rates of polymers used in the FET.
a, Thicknesses of each polymer after certain dry etching time. **b,** The linear regression of each curve shows the etching rate of each polymer.

The experiments were performed using the same etcher and the same etching parameters (RIE: 80 W, 50.0 mTorr, 35–40 °C, 50.0 sccm O_2).

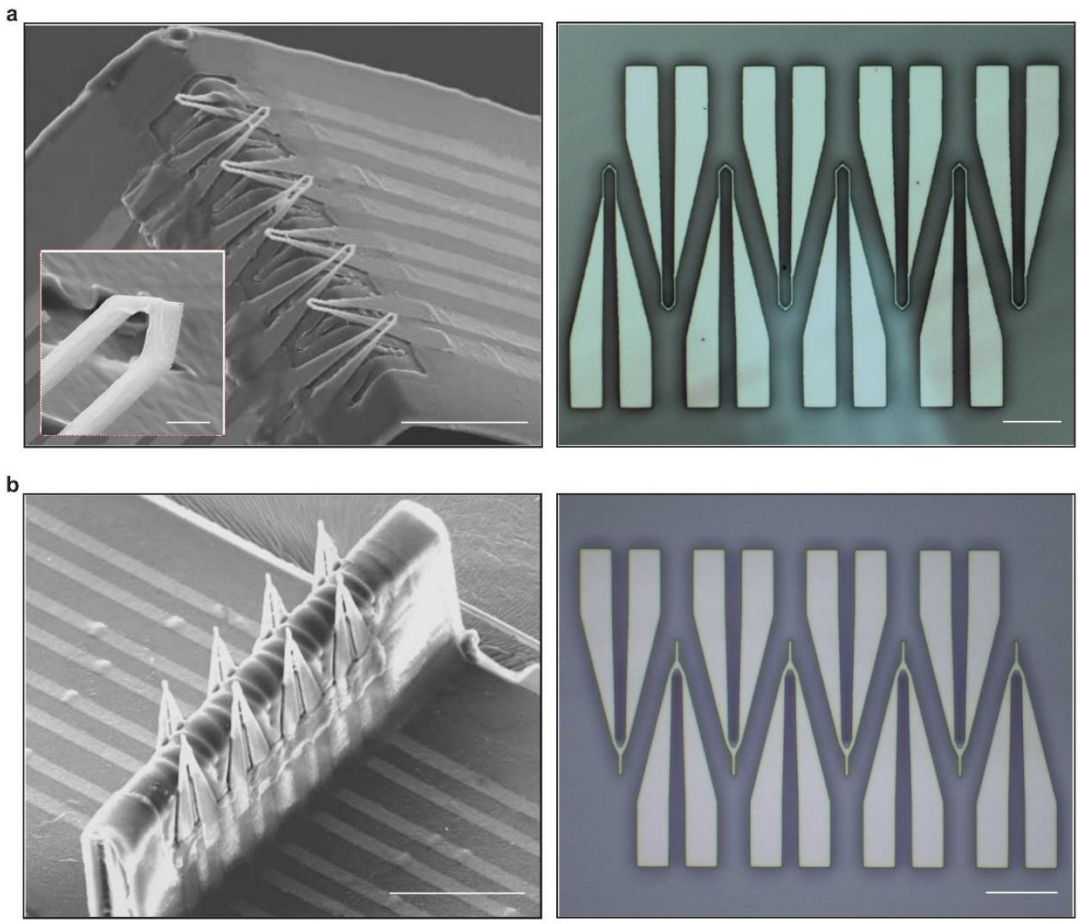

Figure 15. Versatile designs of the FET shape.
Scanning electron and optical microscopical (SEM and OM) images of FETs of two representative structural designs. **a**, An SEM image of an eight-FET array after buckling (top) and an OM image of them in 2D (bottom). Each sensor has a kinked tip defined by e-beam lithography (inset). This structure mimics a reported nanowire probe with a similar kinked tip[44]. The prestrain is only halfway released to enlarge the distance between the two rows of probes, thus covering a larger sensing area. **b**, An SEM image of an eight-FET array with sharp tips for minimal invasiveness to the cells (top) and an OM image of them in 2D (bottom). The FET's tip is 1 μm wide and 10 μm long. Scale bars: 50 μm in the top two SEM images; 2 μm in the inset image of (**a**); 20 μm in the bottom two OM images.

The etching rate of each polymer was determined by the linear regression of each curve. These numbers provide critical information to design the materials used in the FET device and the fabrication processes.

Notably, the introduced technology of fabricating the soft platform can be easily adopted to make other shape and type of sensor arrays. Figure 15 shows two different FET arrays made using this platform technology.

2.4 Robust Test of the Soft Platform in Mechanical Simulation.

To make the entire device mechanically robust, we have carried out theoretical and experimental studies to optimize the materials and their dimensions, such as using low molecular weight poly(methyl methacrylate) (PMMA) and thick acid-resistant photoresist as sacrificial layers.

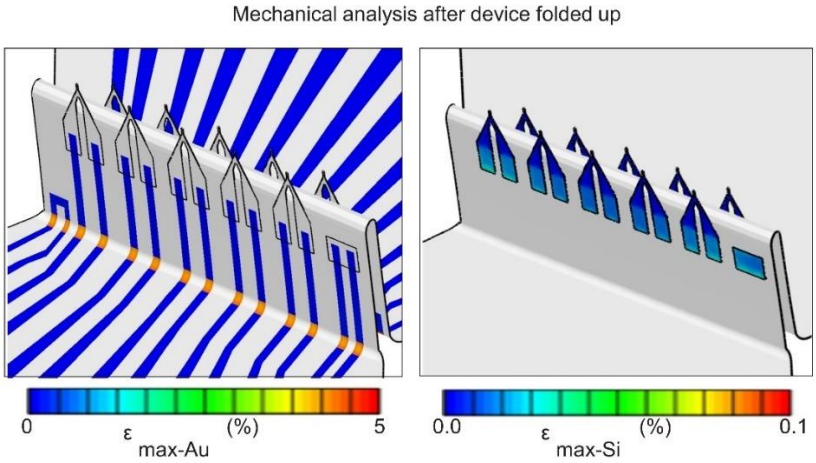

Figure 16. Mechanical simulation of the FET structure.
Finite element analysis of a 3D 10-FET array. The maximum strains in Au and Si are well below the fracture limit of each material.

As simulated by finite element analysis (Figure 16), after the optimization, the maximum strains of the Au and Si in the buckled 3D device are 4% and 0.05%, respectively, which are under their failure strains. The buckling process is reversible. Upon externally applied tensile strain, the

3D device unfolds and recovers to the 2D geometry. The softness of the device reduces the mechanical mismatch between the cell culture and the device.

ABAQUS (v6.13) was used to study the mechanical behavior of the device during compressive buckling. As the thickness of the silicone substrate was much greater than that of the device, a boundary condition was to constrain the device to buckle only above the substrate. Displacement boundary conditions were applied to the two edges of the device to initiate the compression. Composite shell elements (S4R) were used to model the SU-8, PI, Si, and Au layers. The minimal size of the element was set to be half of the FET tip's width (~0.5 μm). The total number of elements in the model was ~106. Mesh convergence of the simulation was accomplished for all cases. The elastic modulus (E) and the Poisson's ratio (ν) are as follows: E_{PI} = 2.5 GPa, ν_{PI} = 0.34; E_{Si} = 130 GPa, ν_{Si} = 0.27; E_{Au} = 78 GPa, ν_{Au} = 0.44; and E_{SU-8} = 4 GPa, ν_{SU-8} = 0.22. The fracture strain of Au and Si are 5 % and 1 %, respectively.

2.5 Verification of the FET Structure in Scanning Microwave Microscope.

The FET's structure was verified by scanning microwave microscopy in topographic and reflection coefficient mapping modes (Figure 17).

The FET was characterized by a scanning microwave microscope (SMM; KeysightTM 7500), which combined an atomic force microscope and a vector network analyzer. The atomic force microscope had a conductive probe scanning on the FET surface to show the topography.

Simultaneously, a microwave signal from the network analyzer was transmitted to the probe, reflected by the sample at the contact point, and then sent back to the network analyzer.

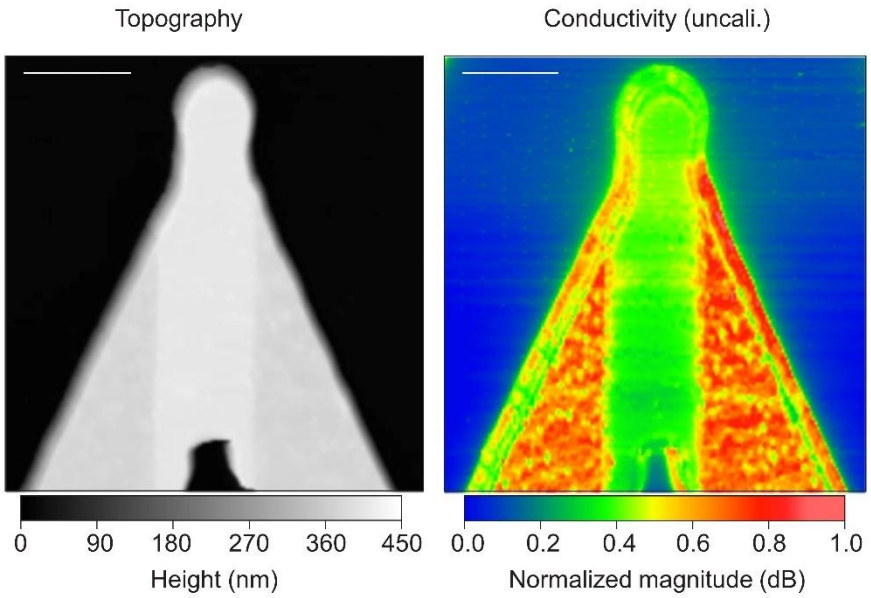

Figure 17. Characterization of the FET structure.
Images of an FET tip by atomic force microscopy (left) and a scanning microwave microscopy (right). The former operates in the contact mode and maps the surface topography of the FET. The latter maps the uncalibrated conductivity, and thus the admittance distribution, of the FET. A lightly doped region can be clearly distinguished in both images. Because of the over-etching of the oxide doping mask, the lightly doped region is slightly thicker than the surrounding heavily doped regions. Also, the lightly doped region shows a lower conductivity than the surrounding heavily doped regions. Scale bars: 2 μm.

The reflection coefficient obtained from the transmission and reflection signals showed the conductance information.

The reflection coefficient of the microwave signal varies depending on the dielectric properties of the sample at each scanned point; hence the conductivity can be mapped. In the experiment, we particularly tuned the reference setting so we could verify if the corresponsive relationship between the reflection coefficient and the uncalibrated conductivity was positive or negative[61,62].

To enhance the measurement sensitivity, a homemade interferometric system was developed. The interferometric system contained a hybrid coupler that split the source microwave into two coherent signals[61,62].

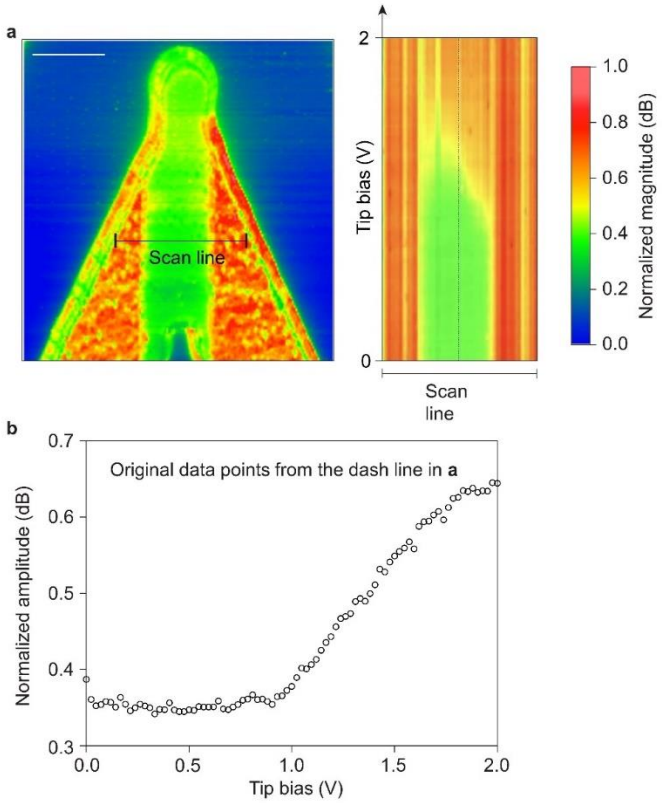

Figure 18. Mapping FET's conductivity by an atomic force microscope with a bias applied by the scanning tip.

a, A linear scan of the FET's conductivity was performed with a positive bias by the atomic force microscope. The results show a larger positive bias applied on the FET's lightly doped conduction channel yields a larger conductivity in the channel, which verifies the n-type properties of the FET's channel, which corresponds with the results by electrical transport characterizations. Scale bar: 2 μm. **b,** Original data points from the conductivity linear scan showing the FET's conduction channel turns "ON" at the 1 V tip bias. The "threshold voltage" didn't appear in the water-gate characterization because we use a much smaller gate bias range for scanning the water-gate characterization. Additionally, we expect the FET device is "ON" at zero bias because the middle region is also n-type with lots of free electrons. The discrepancy between the two measurements is from their different characterization mechanisms, including the gate capacitance, method of applying the gate bias, and the information that can be read from the signals.

One signal went to the probe, and the other to a tunable attenuator and phase-shifter. Both signals got reflected: the former one was reflected by the sample, and the latter reflected by the tunable attenuator and phase-shifter. The two reflected signals were combined at the output of the coupler and canceled each other after proper tuning. The resulting signal was amplified and measured by the network analyzer in the transmission mode. With proper tuning, the system operated at its best sensitivity; small conductivity changes could be detected.

A linear scan of the FET tip area was performed to verify the doping results. In Figure 17, the conduction channel's conductivity increased with a greater bias applied by the atomic force probe, which showed convincing evidence that the FET had an n-type channel. The conductivity went up when the tip bias was ~1 V, representing the threshold voltage to turn "ON" the FET. Notably, the FET was engineered to have an N^+NN^+ structure which meant it was in a depletion mode at the "ON" state with zero gate bias.

The plausible contradiction here could be due to the different mechanisms of the characterization approaches, where the gate capacitance, method of applying the gate bias, and the information that could be read from the signals were different, which have been well studied[63].

The difference of the ON/OFF voltage range between the tip-gate and the ion water-gate is mainly caused by that the ion water-gate has a much bigger gate capacitance (double-layer capacitance) so that a small gate-voltage can result in a larger carrier density change in the semiconductor channel, hence affect its conductance greatly. The tip gate capacitance is small; hence it needs a bigger voltage to reach the same switch effect.

The ability of an FET to accurately capture cellular signals, especially the low-amplitude sub-threshold potentials, depends on its sensitivity and noise level. The sensitivity is determined by the transconductance, which is tunable by the doping profile of the conduction channel.

Each FET's gate terminal was electrically coupled with the ionic solution, so ionic flows in the solution would change the electrical field and thus conductance in the conduction channel of the FET by electrostatic interactions. An FET sensed the electric field potential on its gate terminal and translated the value by its current readout through its conduction channel. The translational factor is defined by the transconductance of the FET, which we also used to define an FET's sensitivity. The transconductance gm is defined as:

$$g_m = \frac{\Delta I_{ds}}{\Delta V_g}, (1)$$

where Ids is the current in the conduction channel of the FET and V_g is the electric field potential on the gate, which also represents the membrane potential in recording the cellular signals. After measuring the transconductance of the FET, we can correspond the current in the conduction channel to the gate potential by the following formula:

$$I_{ds} = V_g \times g_m, (2)$$

In the case of cell membrane potentials, it can be written as:

$$I_{ds} = V_m \times g_m, (3)$$

where V_m is the membrane potential, i.e., the action potential. The FET sensor was cascaded to a current preamplifier where the current was amplified and converted into a voltage reading and fed into the downstream data acquisition (DAQ) system. The DAQ then digitalized the voltage signal as the computer readout, which could be expressed as:

$$V_r = I_{ds} \times \beta, (4)$$

where V_r is the voltage readout in the DAQ and β is the amplification of the preamplifier. We can establish the relationship between the membrane potential, V_m, and the voltage readout, V_r, by substituting equation (3) into equation (4):

$$V_r = V_m \times g_m \times \beta, (5)$$

Or

$$V_m = \frac{V_r}{g_m \times \beta}, (6)$$

The amplification β is a known value, which was pre-set at its design period. The transconductance, gm, can be determined by the slope of the line plot of I_{ds}-V_g in the water-gate characterization of the FET sensor. Therefore, we can accurately obtain the recorded intra- or extra-cellular membrane potentials by the voltage readouts.

The FET's sensitivity and noise level were analyzed and computed in MATLAB. The sensitivity was represented by the slope of the FET's water-gate characterization plot. To obtain the slope, a linear fitting of the plot was performed. The noise amplitude was calculated from the same plot. First, we substituted every gate potential (x-coordinate) into the fitting function to get a new set of values, which represented the recordings without noise. Second, we subtracted the new values from the originally recorded (y-coordinate) values and got the pure noise signals. Third, the difference between the maximal and minimal values of the noise signals represented the peak-to-peak amplitude of the noise.

Lower doping concentrations typically yield higher sensitivities[64]. However, noise level also increases with sensitivity, especially in the low-frequency regime[1]. Therefore, the sensitivity-

to-noise ratio is used to characterize the FET performance. By tailoring the doping time, we can precisely control the sheet resistance and thus doping concentrations in different regions of the FET, leading to a selectively doped N^+NN^+ structure.

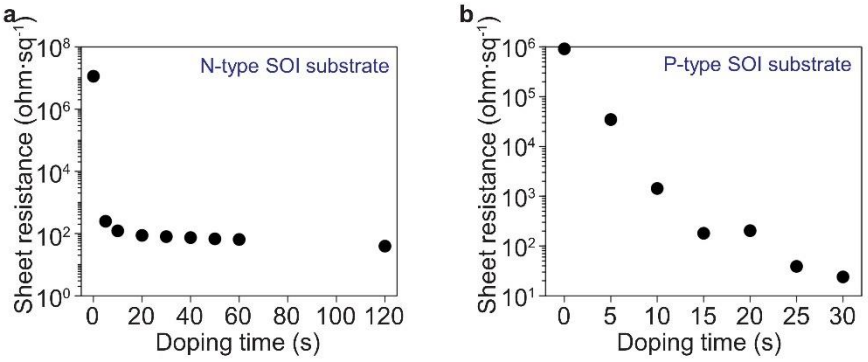

Figure 19. Tuning doping concentration by changing annealing time.
Sheet resistances of (**a**) antimony doped SOI (N-type) and (**b**) boron doped SOI (P-type) wafers, determined by high-temperature doping with phosphorus dopant (P509) at 950 °C for various doping times (Δt), which is defined as the period that the apex temperature was held during annealing.

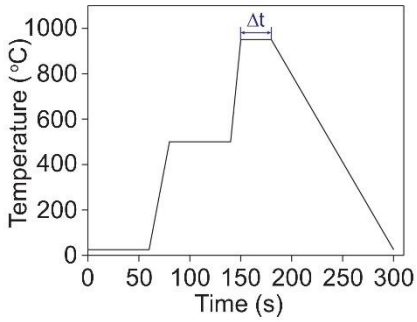

Figure 20. A typical temperature profile for driving the phosphorus dopants into the SOI wafer.
The most effective doping period was at the highest temperature (950 °C), as indicated by Δt. A longer Δt generates a smaller sheet resistance of the SOI. We applied a two-step doping process: the first light doping was for the whole SOI that determined the FET's conduction channel's doping concentration; and the second heavy doping was for the whole SOI except the conduction channels. The resultant FET had an N^+NN^+ structure and worked under a depletion mode.

The N^+NN^+ structure is crucial for high sensitivity and operational reliability at zero gate bias because it operates at the "ON" state with zero gate bias, which avoids the irreversible faradaic reactions induced by the high gate voltage during signal recording with other FET structures.

For the FET geometry in Figure 17, we optimized the doping time using the profile in Figure 20 to get the highest sensitivity-to-noise ratio (Figure 21).

The sensitivity-to-noise ratios of the selectively doped FETs are much higher than those of FETs with low uniform doping (i.e., only background doping from the substrate) or high uniform doping (Figure 22). The reflection coefficient of the microwave signal varies depending on the dielectric properties of the sample at each scanned point; hence the conductivity can be mapped. In the experiment, we particularly tuned the reference setting so we could verify if the corresponsive relationship between the reflection coefficient and the uncalibrated conductivity was positive or negative.

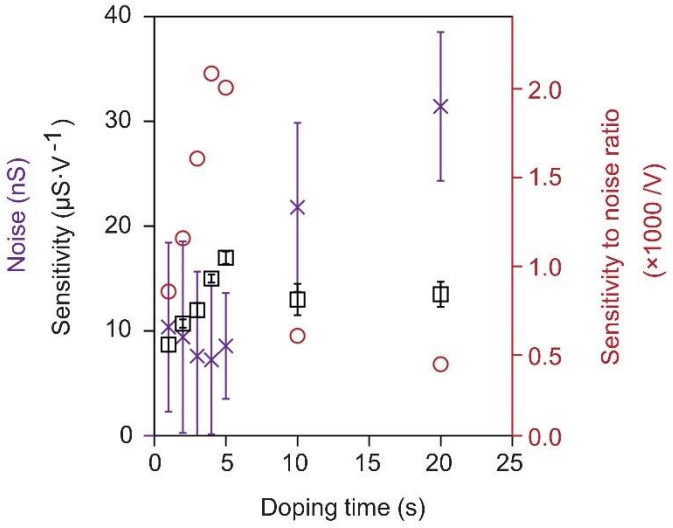

Figure 21. Optimization of FET's sensitivity to noise ratio.
The FET's sensitivity-to-noise ratio as a function of the doping time in the lightly doped region. A doping time <4 s leads to a lower current in the conduction channel. A doping time >4 s results in higher noise, because of a larger number of traps generated by the doping-induced defects.

The significant difference between a depletion-mode and an enhancement-mode FET is whether it is "ON" at zero gate bias, where the depletion-mode FET already has charges in the conduction channel ("ON") without a gate bias. The feature is beneficial for the FET biosensors to operate in an aqueous environment because we can avoid the large gate bias required to turn on the FET, which would generate irreversible faradaic reactions such as the electrolysis of water. Further, the depletion-mode FETs show high sensitivity and thus have been extensively used to detect weak signals in biological systems[65].

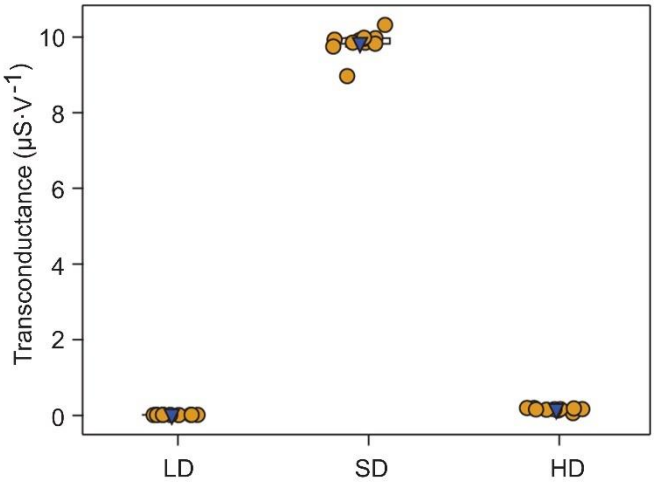

Figure 22. Sensitivity of FET determined by the doping condition.
Calculated transconductances of three devices with different doping profiles, showing the FET structure is crucial for the high sensitivity: low doping (LD, uniform doping at ~10^7 Ohm·sq^{-1} from the silicon-on-insulator substrate), selective doping (SD, light doping at ~10^4 Ohm·sq^{-1} in the gate, and heavy doping in the drain and source), and heavy doping (HD, uniform doping at ~10^2 Ohm·sq^{-1}).

We prepared p-type and n-type depletion-mode FET arrays (Figure 24). These two arrays had the same structure and dimensions. Each array had ten FETs with heavily doped source and drain regions (p-type: ~10 ohm·sq^{-1}; n-type: ~10^2 ohm·sq^{-1}) and an undoped gate region (p-type: ~10^6 ohm·sq^{-1}; n-type: ~10^7 ohm·sq^{-1}). In Figure, transfer characteristics of both devices showed

that the n-type FETs demonstrated about six times larger sensitivity than the p-type FETs. Therefore, we chose the n-type depletion-mode FET in this work.

Optimizing the doping levels in the drain, source, and gate regions of the N^+NN^+ FET yielded the largest sensitivity-to-noise ratio of the FETs. In this process, we lightly doped the gate region for 1~20 seconds (Figure 21). Before doping, the SOI wafer had a background doping level (antimony doped), making its sheet resistance ~10^7 ohm·sq^{-1}. The sheet resistances of lightly and heavily doped silicon were 10^4 ohm·sq^{-1} and 10^2 ohm·sq^{-1}, respectively.

To improve the sensitivity-to-noise ratio, ideally, we want to increase the sensitivity and, in the meantime, decrease the noise level of the FET. However, these two properties would show a positive relationship between each other. In electrophysiological experiments, electrical measurement noises can arise from current fluctuations in the cell membrane, the sensors, the preamplifier electronics, and/or external sources such as power lines, computers, monitors, and many other devices located in the vicinity of the measurement setup.

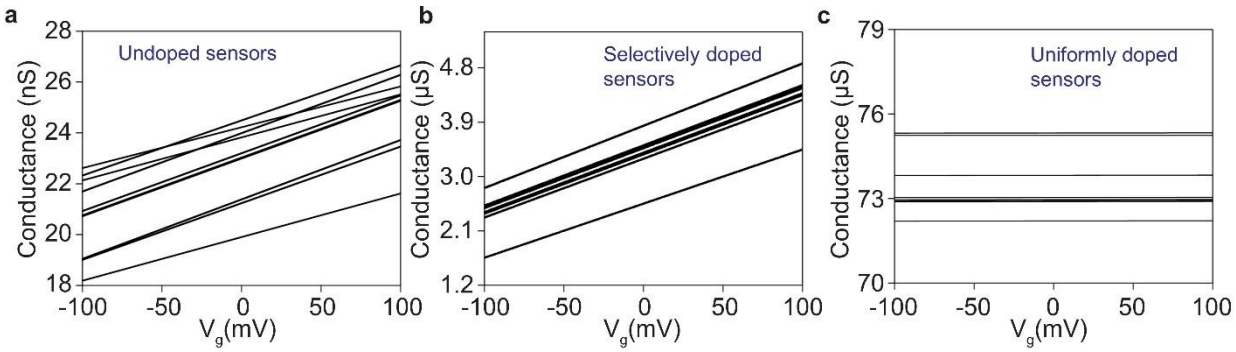

Figure 23. Transfer characteristics of devices by various doping conditions.
Transfer characteristics of devices by various doping conditions, including (**a**) undoped, (**b**) selectively doped, and (**c**) heavily uniformly doped sensors.

External noises can be largely reduced by the application of electromagnetic shielding, such as using a faradaic cage to isolate the cells and sensors from the surrounding electronics. However, internal noises represented by current, or voltage signal fluctuations cannot be avoided. These noises often show in low-frequency regions, so-called low-frequency noise. Generally, thermal noise, shot noise, pink noise (i.e., flicker noise or 1/f noise), and generation-recombination noise represent the common internal noises in a transistor sensor[66]. Pink noise and generation-recombination noises are frequency-dependent and are high in the low frequency.

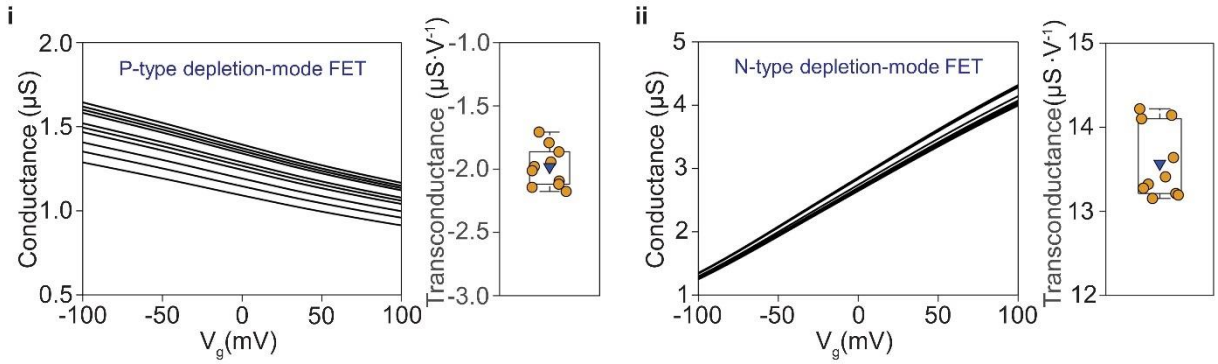

Figure 24. Transfer characteristics of p-type and n-type transistor.
Transfer characteristics of (**i**) p-type and (**ii**) n-type depletion-mode FETs, showing that the n-type FETs demonstrate about six times larger transconductances (i.e., sensitivities) than those p-type FETs. Therefore, we chose n-type depletion-mode FETs in this work.

The positive relationship between the noise level and the FET's sensitivity is in two aspects. First, there was external noise during the electrical measurement even a faradaic cage was implemented. These noises were amplified by the FETs. Thus, a FET of higher sensitivity leads to a higher level of noise. Second, in a model describing the sensitivity of silicon nanowire transistors to the gate charge, the transistor's sensitivity would increase by decreasing the doping concentration[64]. At the same time, lower doping concentration would elevate the noise level of the

transistor. Therefore, we can conclude a positive relationship between the transistor sensitivity and the noise.

2.6 Electrical Characterization of the Soft Platform.

We characterized the transport behavior of a 10-FET array in a water gate configuration (Figure 25). The FET's sensitivity was obtained by measuring the FET's transfer characteristics. In the water-gate characterization, the corresponding FET's conductance was measured under a fixed positive bias (e.g., 200 mV) at the source and a potential sweep (from -100 to 100 mV) at the gate.

The measurement system is illustrated in Figure 25, where the FET was connected to preamplifiers, DAQ (e.g., DigiData 1440A), and downstream to a computer graphic user interface (GUI; for example, Axon pCLAMP 10 Software Suite).

The ionic solution such as the phosphate-buffered saline (PBS; Sigma-Aldrich, pH = 7.4; temperature = 37 °C) or typical Tyrode's solution (NaCl 140 mM, KCl 4 mM, $CaCl_2$ 1.8 mM, $MgCl_2$ 1 mM, HEPES (4-(2-hydroxyethyl)-1-piperazineethanesulfonic acid) 10 mM, glucose 10 mM, pH = 7.35 with NaOH, temperature = 37 °C) was added on the FET's gate surface. An Ag/AgCl electrode was immersed in the solution and applied a potential sweep from -100 mV to 100 mV to the solution. In the meantime, a positive potential (e.g., 200 mV) was fed to the FET's source terminal.

The FET's drain terminal conducted currents to the downstream preamplifier. With a change in the gate potential, the corresponding change in the source to drain current could be

recorded and plotted in the GUI. The FET's sensitivity was finally defined by the slope of the FET's transfer characteristic plot.

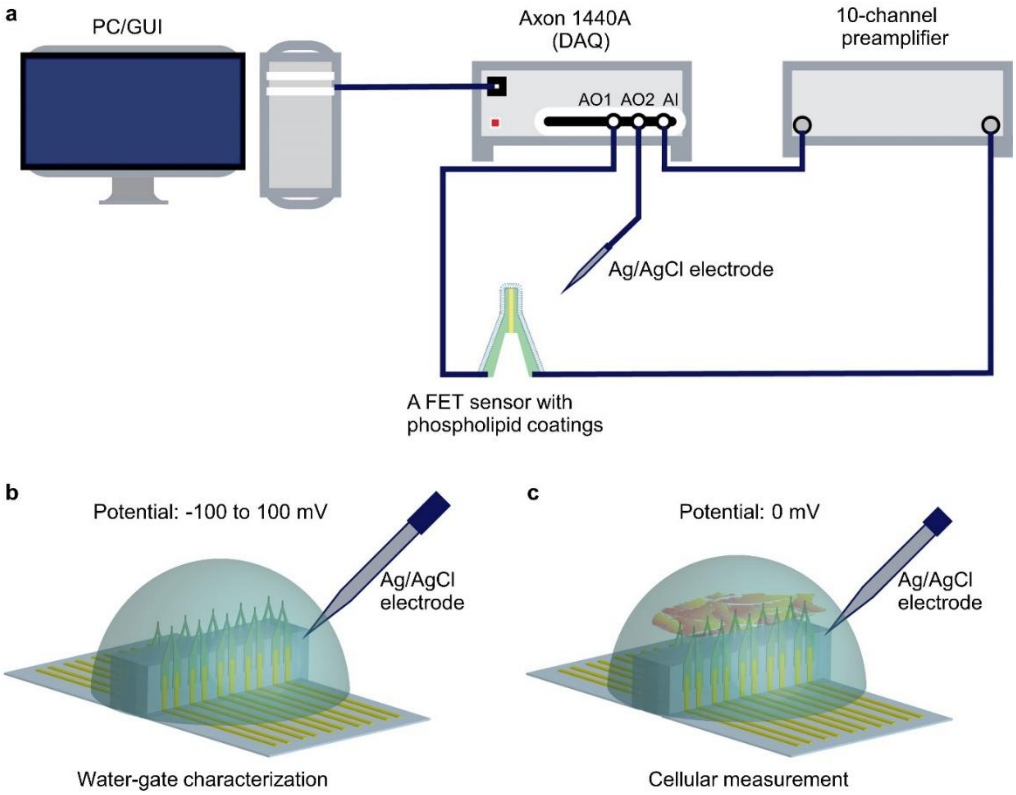

Figure 25. Experimental setup for recording cellular electrophysiology by the arrayed FETs. **a,** The setup includes a computer with an installed commercial program (Axon pCLAMP 10 Software Suite), which is used to control the other electronic equipment to acquire the analog signals and to display the converted digital data. The computer is connected with a DAQ that can convert digital to analog or analog to digital signals. One analog output (AO1) channel is connected to the source terminal of all arrayed FETs that share the same potential. Another analog output (AO2) channel is connected to the Ag/AgCl electrode. While performing the water-gate characterization, a potential sweep was applied on the Ag/AgCl electrode. In the cellular signal measurements, a zero potential was applied to that electrode to provide a reference potential of the extracellular medium. The DAQ has a total of 16 analog input (AI) channels. Each channel is connected to one output channel of the preamplifier. The preamplifier's inputs are connected to the drain terminals of the arrayed FETs. **b**, A schematic showing the experiment setup during the water-gate characterization of the FETs. On the Ag/AgCl electrode, a potential is swept from -100 mV to 100 mV. The solution used in this experiment is either PBS or Tyrode's solution. **c**, A schematic showing the experimental setup during cellular signal recording. A zero-gate potential is applied to the Ag/AgCl electrode during measurements. The solution is the extracellular medium of the specific cells being measured.

The output characteristics of an FET in the array illustrate its typical n-channel properties under various gate biases (Figure 26a). The FET exhibits large conductance under various drain potentials at zero gate bias (Figure 26b), which is crucial for sensing cellular electrophysiological signals.

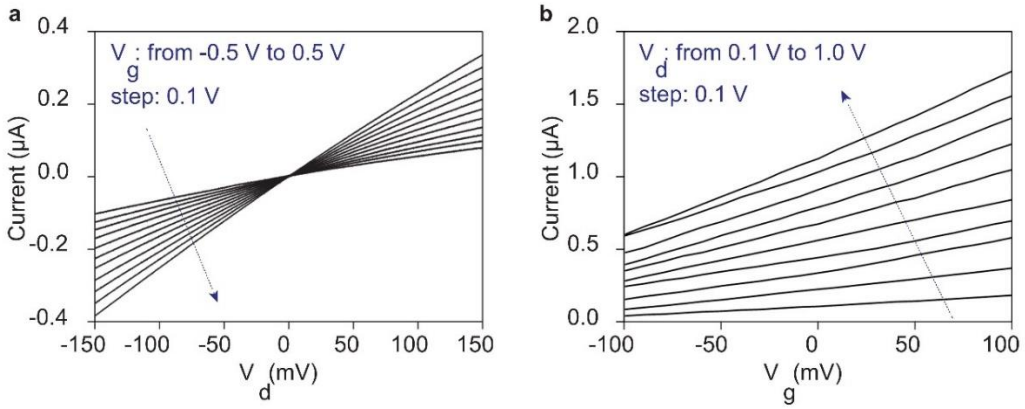

Figure 26. Electrical characterization of an FET.
a, Output characteristics of the n-channel FET in the linear region under different applied gate voltages. **b,** Transfer characteristics of the FET under different drain voltages. The FET is in a depletion-mode, which is "ON" at zero gate voltage. It shows a high transconductance in the -100~100 mV regime. V_d: drain voltage; V_g: gate voltage.

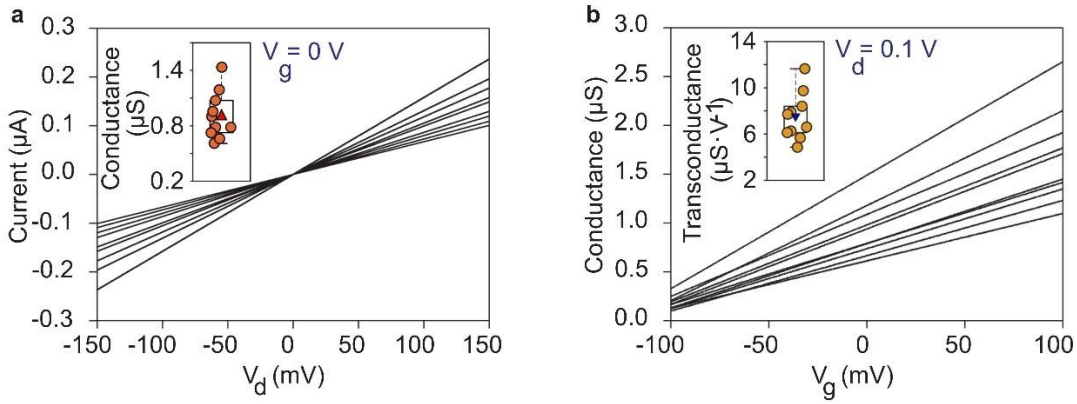

Figure 27. Electrical characterization of ten FETs in the same device.
a, Output characteristics of each FET in a 10-FET array. Inset, distribution of the FETs' conductance. **b,** Transfer characteristics of each FET in the array. Inset, distribution of the FETs' transconductance.

The 10 FETs have an average conductance of 0.9 ± 0.3 μS (Figure 27a) and an average transconductance of 7.5 ± 2.0 $\mu S \cdot V^{-1}$ (Figure 27b).

The transconductance is greater than, and its relative standard deviation (i.e., coefficient of variation) is comparable to those of devices synthesized by bottom-up methods[67], which can be attributed to the high material quality of the device-grade Si and controllable fabrication process. The high performance allows the FETs to record low-amplitude sub-threshold cellular signals[39].

It was notable that in the FET's temporal response to rapid signals (Figure 28a), sometimes there was an overshoot, which was caused by the capacitance between the metal wires, dielectric layers, and the ionic solution.

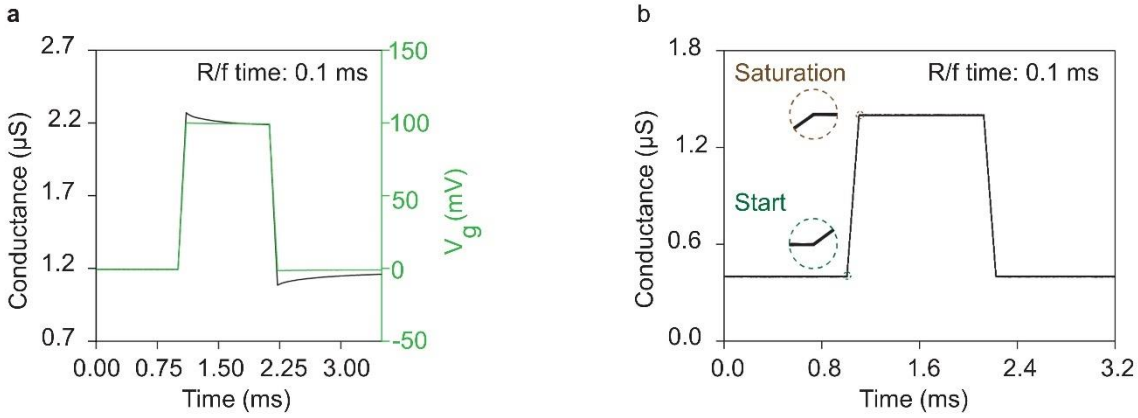

Figure 28. Temporal response of the FETs to gate signals.
a, A 100 mV pulse (rising/falling (R/f) times: 0.1 ms; duration 1 ms, green curve) is applied to the gate. The corresponding conductance of the FET (black curve) exhibits changes coincident with the input signal without any noticeable delay. **b,** Repeated characterization of the same FET 10 times with an input gate signal at 100 kHz sampling rates (0.01 ms resolution). The FETs show no observable jitter (<0.01 ms) in the data acquisition system.

These three layers formed a parallel plate capacitor. In the water-gate characterization, the ionic solution and thus the gate signal was covered everywhere. Therefore, the metal-induced capacitance would affect the characterization result. However, in the cellular measurement, the

local cellular signal is applied to the FET locally, but not on anywhere else, so we could safely neglect the capacitance effect in the cellular measurements[41].

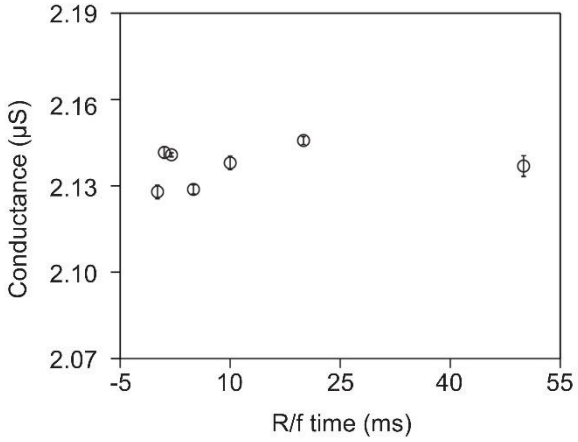

Figure 29. FET conductance with various rise/fall time of the input signal.
The FET's conductance is reliable and independent from the rising/falling times of the input signals.

To ensure we can record the dynamic and transient ionic signals, we characterized the temporal response of the FETs. Pulse signals with a rise and fall time of 5 ns – 50 ms were applied on the gate, and the channel signals of the FETs were recorded. The FET shows a short intrinsic response time to the input gate signals (≤712 ns), which is shorter than previously reported values due to its optimized small gate dielectric thickness[68] (Figure 30).

Due to the limit of the sampling rate of the digitizer (100 kHz maximum), the entire recording system has a temporal resolution of 0.01 ms, and thus the recorded channel signal shows a response time of 0.1 ms (Figure 29a), which is sufficient to accurately record common ionic activities (typically >1 ms)[69].

Note that there is a capacitance-induced overshoot on the rising and falling edges of the response. The capacitance was from the electrode-ionic solution coupling, which could be

neglected in cellular measurements because of the localized coupling between the membrane potential and the FET[41].

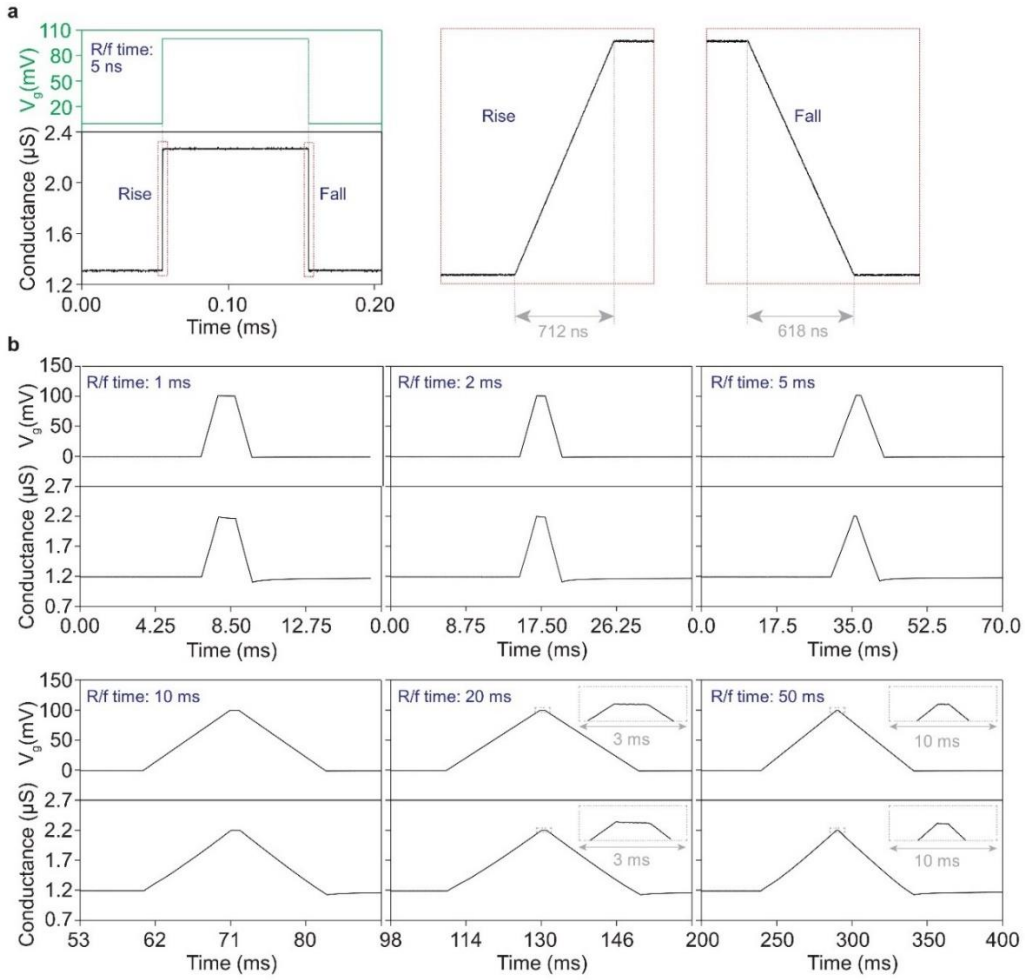

Figure 30. The FET's response characteristics to rapid and slow signals.

a, The FETs respond quickly to the rapid signal applied on its gate (rising/falling (R/f) time 5 ns, duration 0.1 ms, amplitude 100 mV, Model 3390, Keithley). The FETs' response time to the rapid signal is hundreds of nanoseconds (Rising: 712 ns; Falling: 618 ns), recorded at a 2 GHz sampling rate (PicoScope 6000) and analyzed in MATLAB. b A 100 mV pulse (rising/falling time ranging from 1 ms to 50 ms, duration 1 ms) is applied on the gate by an Ag/AgCl electrode. The corresponding conductance of the FET remains the same trends to the input signals, which manifests its fast and stable response to various signals. The ionic solution-FET gate coupling is influenced by the ionic solution-metal electrode coupling in the water-gate measurement. The induced capacitance responds differently to various AC (fast and slow) inputs and slightly changes the FET's conductance. The induced capacitance can be safely ignored in cellular measurements due to the very localized membrane potentials to the FET gate. These results demonstrate the FET's fast response and large bandwidth for cellular measurements.

In repeated measurements, the start and saturation times of the FET's response remain unchanged, showing that it can accurately follow the rapid input signals (Figure 29b).

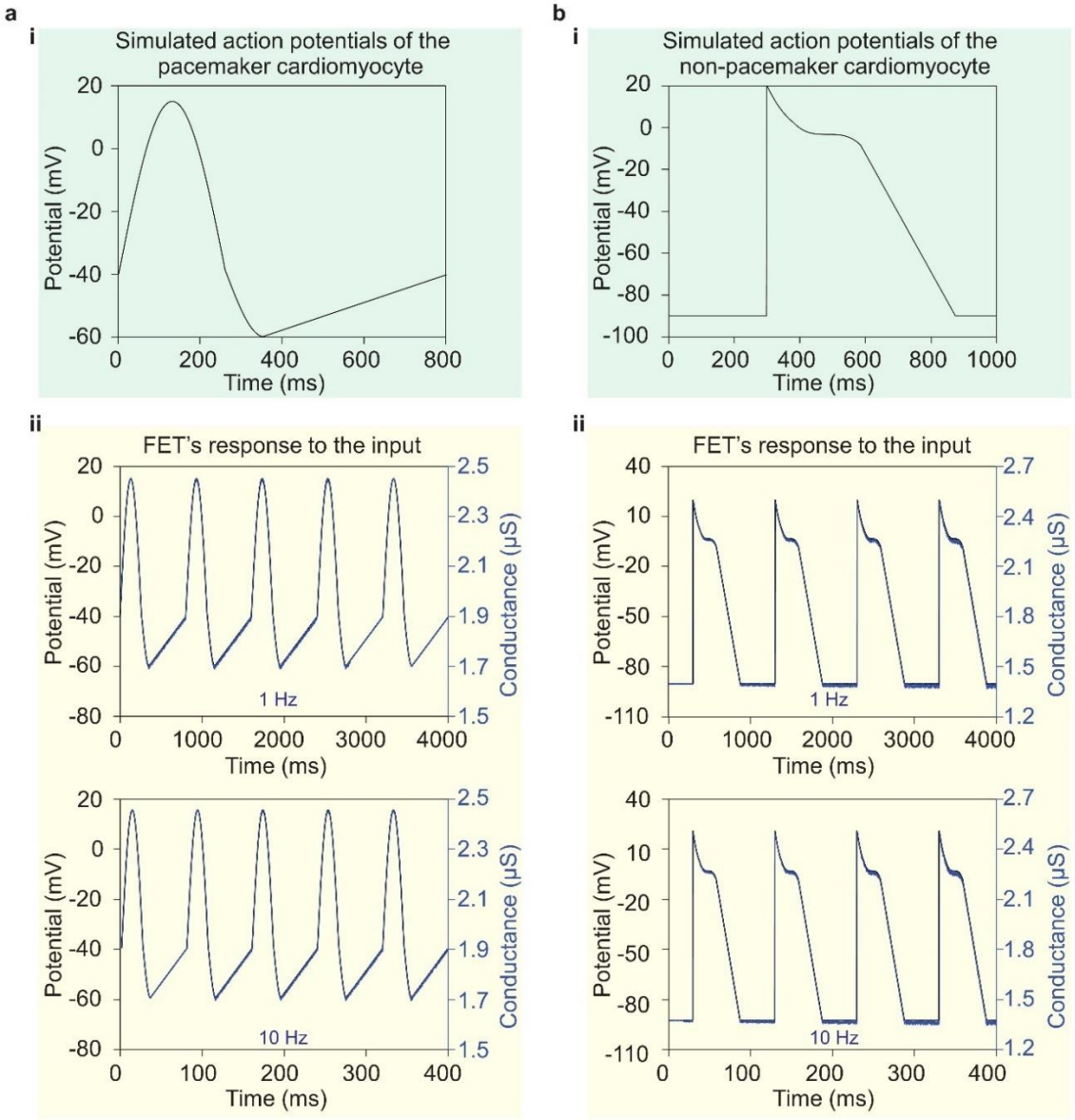

Figure 31. The FET's response to simulated cellular action potentials.
a,**b**, Simulated action potentials for (**a**) pacemaker and (**b**) non-pacemaker cardiomyocyte. Using the water-gate characterization setup and applying the simulated signals on the FET's gate at 1 Hz, and 10 Hz, corresponding to the action potential frequencies of various mammals' cardiomyocytes. Corresponding signals recorded by an FET are plotted in the same figures, with high fidelity to the original signals' morphologies at these frequencies.

With different rising/falling times (0.1–50 ms) of the input signal, the conductance changes are within ~1.5%, which is typical for FETs (Figure 30). Additionally, the FETs can faithfully record simulated cellular action potentials resembling those produced by pacemaker and non-pacemaker cardiomyocytes, with frequencies over 1~10 Hz, covering the typical firing frequencies of electrogenic cells (Figure 31).

The response time of an FET shows its switching characteristics. The typical switching frequency of the silicon FET is in the megahertz range, corresponding to the response time of hundreds even tens of nanoseconds[70]. The response time of an FET is primarily affected by the input capacitance (such as the gate-source capacitance and gate-drain capacitance)[41]. For an FET sensor that interacts with cells, the FET must accurately retain fast and slow cellular signals, including opening and closing of rapid sodium ion channels (~1 ms)[71], initiation of an action potential of cardiomyocytes (~1 ms)[71,72], and activation of fast transient outward current of potassium ions and chlorine ions (<10 ms)[69,71]. It herein requires the FET to show the fast response to cellular signals with a wide bandwidth, which means the frequency range that the biosensor can maintain a stable amplitude of the detected signals. Within this range, the amplitude of the recorded signals by the FET is almost fixed with little fluctuations.

Here, we characterized the FET's response time by applying a rapid signal on its gate terminal using a similar configuration to that of the water-gate characterization. We used an arbitrary waveform generator (Model 3390, Keithley) to generate a pulse signal (rising/falling time: 5 ns, duration: 0.1 ms, amplitude 100 mV) and fed it to the FET. In Figure 30a, the corresponding FET's output signal indicated a response time of 600~700 ns, much shorter than the recorded signal

latencies between FETs, which were in the microsecond range. It proved the FET sensor had a sufficiently fast response to external signals and therefore could faithfully record rapid cellular electrical signals.

2.7 Stability Test in Biological Environments.

After transforming from 2D to 3D, the 10 FETs showed a <0.2% variation in conductance and a <0.5% variation in transconductance (Figure 32), which validates the 3D FET's mechanical and electrical robustness.

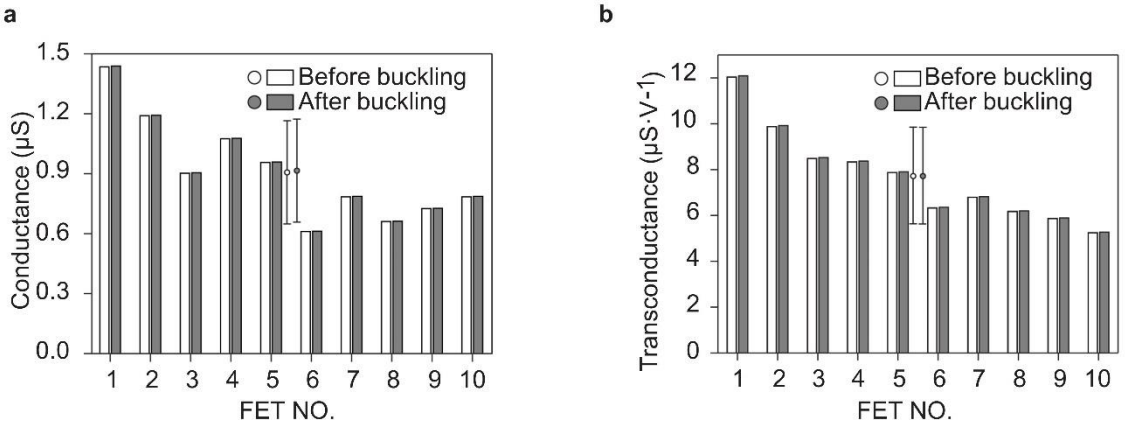

Figure 32. Mechanical robustness test of an FET array.
Comparisons of the 10-FET array's (**a**) conductance and (**b**) transconductance before and after compressive buckling, illustrating that the buckling process has no impact on the FETs' electrical performance. The circles and error bars show the mean and standard deviations of the ten FETs' properties.

The 10 FETs exhibit comparable conductance before and after immersion in saline solution (Figure 33), showing neglectable changes in surface charges and minimal current leakage through the insulation layers.

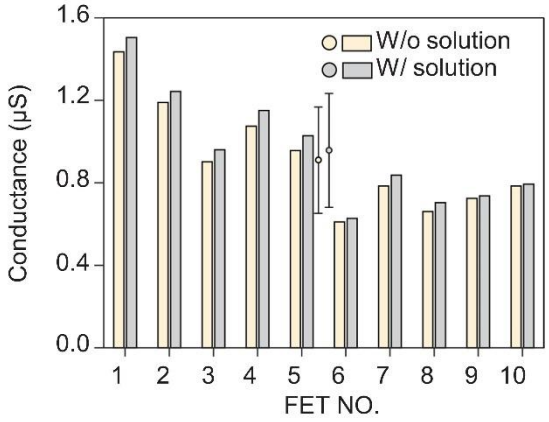

Figure 33. Conductance of FET with and without saline solution on the gate terminal.
Comparison of the FETs' electrical conductance with and without a saline solution on the gate terminal, showing minimal current leakage of the FETs. The circles and error bars show the mean and standard deviations of the ten FETs' properties. The ionic solutions induce slightly more carriers (due to surface absorbed H^+) and thus slightly higher conductance in the conduction channel.

Moreover, the FETs exhibit consistently high sensitivities over a range of pH (from 6.7 to 7.6) and temperatures (from 21 to 50 °C), demonstrating their tolerance for chemical and thermal conditions in various cell culture media (Figures. 34 and 35).

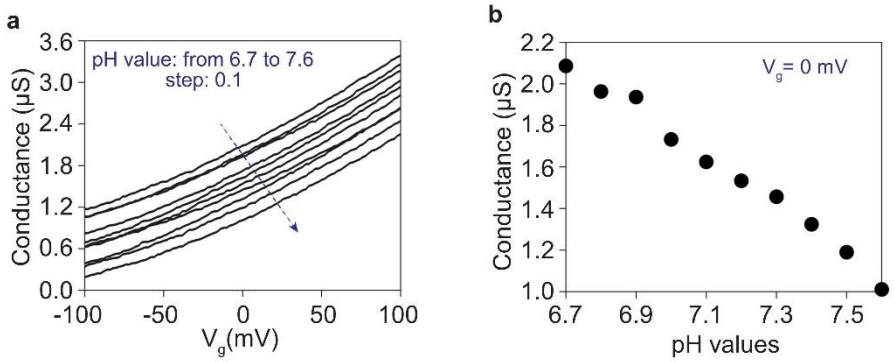

Figure 34. FET's stability test in solutions of various pH values.
a, An FET's conductance with different pH of the gate solution. The transfer characteristics show high similarities, proving the high reliability of the FET under various pH. The common pH for cell culturing is 7.4. **b,** Extracted data points at zero gate bias, showing the conductance decreases with increasing the pH, giving another evidence of the n-type conductivity of the FET.

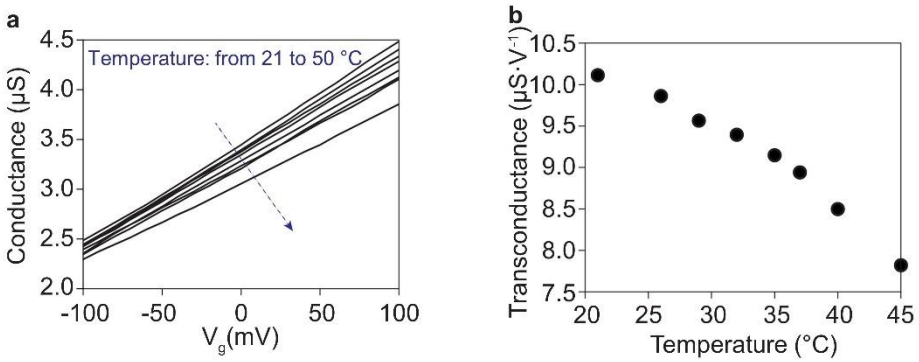

Figure 35. FET's stability test in solutions of various temperatures.
a, An FET's transfer characteristics under different temperatures of the gate solution, showing the FET has excellent thermal stability and reliability under various temperatures. The common temperature for cell culturing is 37 °C. **b,** Calculated transconductances showing the FET's transconductance decreases with increasing the temperature, which is due to the effectively reduced mobility of the charge carriers in the conduction channel.

The stability of the FETs is primarily attributed to the insulating gate dielectric materials. The type of gate dielectric materials will not affect the FETs' sensitivity (Figure 36).

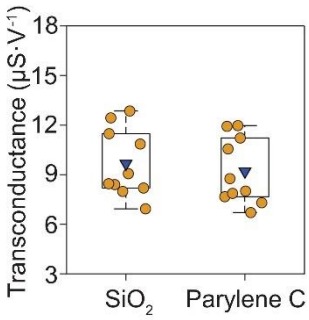

Figure 36. FET's stability test with various gate dielectric materials.
Parylene C was used as an additional gate dielectric material on top of the SiO_2 in the FET, considering SiO_2 might be soluble in biological fluids, such as extracellular solutions of cardiac muscle cells. The FETs' transconductance (i.e., sensitivity) barely changed after coating the Parylene C.

2.8 Functionalization of the FET to Facilitate Cell Insertion.

We coated a phospholipid bilayer on the FETs to facilitate the internalization into the cells[44] and to enable good sealing at the FET-cell interface. Either small unilamellar vesicles of exacted

red blood cell membranes or synthetic phospholipid bilayer materials (1,2-dimyristoyl-sn-glycerol-3-phosphocholine) were used[44,73].

Phospholipid coating on the FET surface facilitated the cell internalization process, by spontaneous fusion, to achieve direct contact with the cells' cytosols. Briefly, large phospholipid vesicles in aqueous solutions were broken into small unilamellar vesicles by consecutive freeze-and-thaw treatments, sonication, and filter extrusion. These high-surface-energy vesicles would form uniform phospholipid coatings on the FET surface by self-assembly.

Two types of phospholipid bilayers were used in the experiments including a synthetic lipid bilayer and a natural cell membrane. These two types of lipid bilayer membranes had different advantages and were preferred in different applications. The natural cell membranes were structurally and functionally similar to those of the host cells so they could express specific cellular biomarkers (e.g., CD47) in the membranes to mimic the cellular surface to the greatest extent[73]. Hence, we could use these natural cell membranes without additional modification. Red blood cell membranes have been widely used for nanoparticles coatings in fields of drug delivery, vascular injury repair, and tumor imaging because of the simplicity of the isolation process[74-78]. On the other hand, synthetic phospholipids showed higher flexibility for engineering and modification and superb stability. Besides, synthetic lipids were usually less expensive than natural cell-derived membranes.

The synthetic lipid bilayer was made of DMPC (1,2-Dimyristoyl-sn-glycero-3-phosphocholine) from Avanti, and the extracted red blood cell membranes were obtained by

following established protocols[41,74]. We added the fluorescent material into the phospholipid bilayers for characterization purposes (Figure 37).

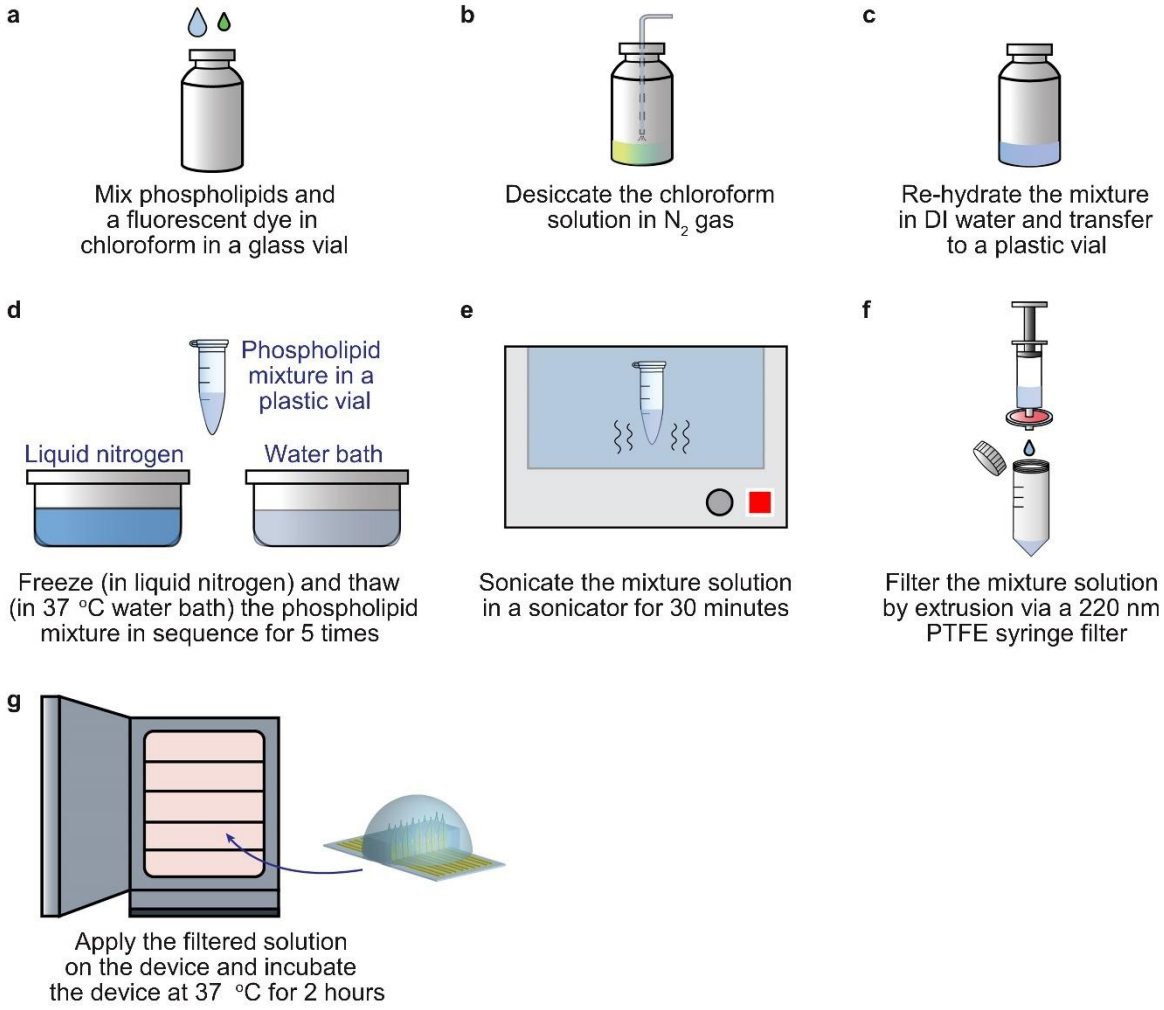

Figure 37. The schematic process of functionalizing the FET surface with phospholipids. To prepare the lipid solution, the phospholipids as received are dissolved in the chloroform solution. The chloroform needs to be removed entirely before the lipids get re-hydrated in DI water. The mixture in the aqueous solution then undergoes a freeze-and-thaw process at least five times to break the multi-lamellar into unilamellar lipid vesicles. Later, sonication disperses the lipid vesicles in the solution and eliminates any aggregates of small lipid vesicles. The final step is to extrude the mixture solution through a PTFE syringe filter. Only the small unilamellar vesicles would be left in the solution. Then the lipid solution is applied on the FETs, which are put in an incubator at 37 °C for at least two hours. After that, removing excessive lipid solutions gently by DI water completes the functionalization. Note that the above processes only work for synthetic phospholipids. For natural cell membranes, they are naturally in a bilayer structure and vesicles. Therefore, only the extrusion step (**f**) is needed to produce small unilamellar vesicles.

We skipped this step when preparing the phospholipid coatings on the FET sensors used for signal recordings. Ideally, the lipid bilayer could naturally merge with the cell membrane. However, in reality, spontaneous fusion would get affected by other materials in the cellular context, such as collagen. The fusion process took some time to form a perfect interface. Plus, the cell could expel the FET out of its body even after the sensor internalization (called the elastic response from the cytoskeleton)[79,80]. The coatings could be repeatedly used for intracellular measurements of different cells about three times. After that, the phospholipid coating became worn and torn, making it difficult to get stable intracellular recordings, or even no signals at all.

The critical step in the preparation of the phospholipid bilayers was to generate high-surface-energy small lipid vesicles that could spontaneously form a lipid coating layer on the FET surface. A step-by-step description of the coating process is introduced below.

First, the received synthetic phospholipids were dissolved in chloroform solutions in glass vials. We removed the chloroform solvent and prepared aqueous lipid solutions. To achieve that, purging nitrogen gas overnight desiccated the chloroform thoroughly in a glass vial.

Second, the phospholipids were re-hydrated with the DI water and immediately transferred to a plastic vial. Here, importantly, using the plastic vials specifically was to prevent the hydrophilic segment of the phospholipid bilayer from attaching to the glass vial walls.

Third, the mixture in the aqueous solution underwent a freeze-and-thaw process (freeze in the liquid nitrogen and thaw in a water bath of 37 °C) for at least five times to break the multi-lamellar lipid vesicles into unilamellar vesicles. The later sonication treatment was also employed to disperse the lipid vesicles separately in the solution and eliminate any aggregation of small lipid

vesicles. The next step of preparing the lipid solution was to extrude the mixture solution through a PTFE syringe filter. Only the small unilamellar vesicles would be left in the prepared solution. These SUVs had high surface energy so they could self-assemble to become a uniform lipid coating on the FET surface. Note that for natural red blood cell membranes, they are in bilayered vesicle structures upon collection for natural cells. They only need to undergo this extrusion process to generate unilamellar small vesicles.

Fourth, to coat the lipid bilayers on the FETs, we applied the lipid solution to the FETs and put them in an incubator at 37 °C to sit for at least two hours. Spontaneous lipid fusion took place at such a higher temperature than the lipid's transition temperature (24 °C for DMPC). After that, removing the excessive lipid solutions gently by DI water completed the functionalization.

Fluorescent images confirm the successful coating of the phospholipids on all FETs before and after buckling (Figure 38).

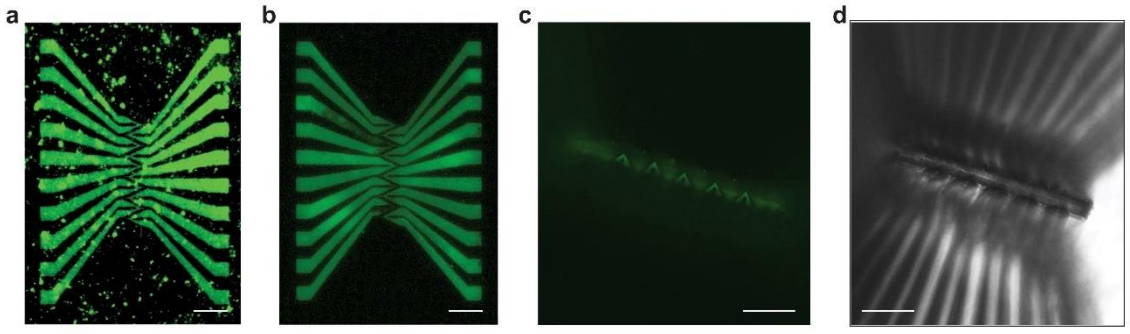

Figure 38. Functionalization of the FET surface with phospholipids.
a,b, Fluorescent images showing coatings of (**a**) natural phospholipids of red blood cell membranes and (**b**) synthetic phospholipid (DMPC) on the gate oxide of the FETs. These coatings promote the FETs' internalization into the cell body by spontaneous fusion of the phospholipids and the cell membrane. Scale bars: 100 μm. **c,d,** (**c**) A fluorescent image and (**d**) the corresponding transmitted optical image showing successful phospholipid coating on the 3D FETs. All FETs are coated by the phospholipids as shown by the intense fluorescence of the FET tips. Scale bars: 50 μm.

To illustrate the internalization process, when the FET is near the cell, it records the membrane potential extracellularly.

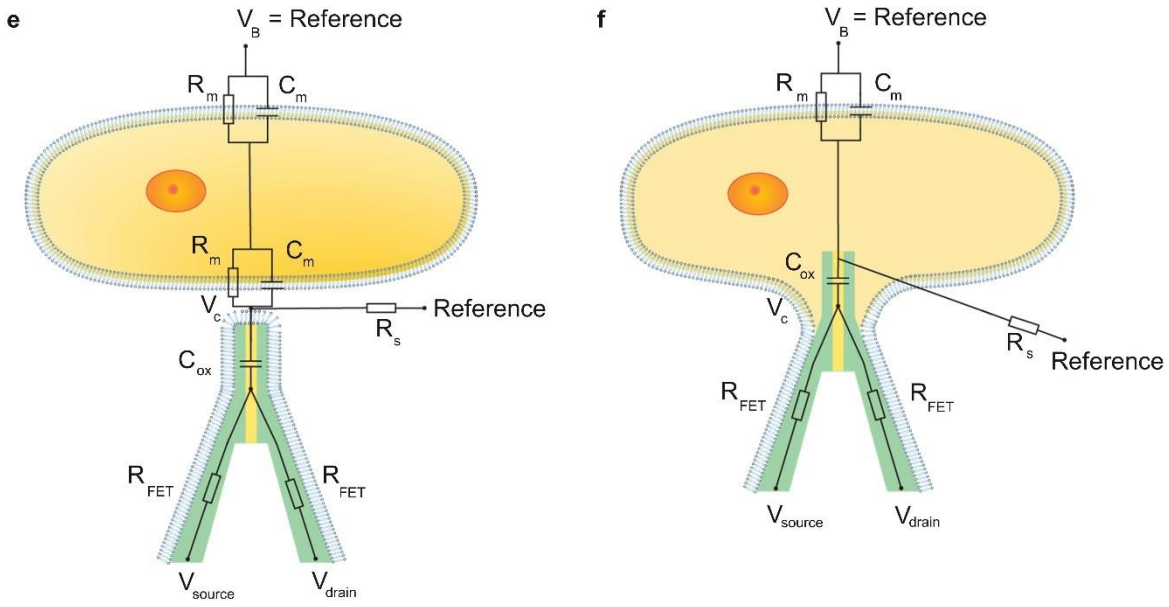

Figure 39. Equivalent circuit models of cellular measurements before and after FET internalization.

Equivalent circuit models of a functionalized FET-cell interface for (**e**) extracellular and (**f**) intracellular interrogations of a cardiomyocyte. Before the phospholipids fuse, the FET sensor is extracellularly recording the membrane potential. The circuit is composed of the FET resistance (R_{FET}), the FET gate oxide capacitance (C_{ox}), the spreading resistance due to the cleft between the cellular membrane and the FET surface (R_s), the cellular membrane capacitance (C_m), the cellular membrane resistance (R_m), the potential applied at the source terminal of the FET (V_{source}), the potential at the drain terminal (V_{drain}), the potential at the extracellular medium (V_B), and the potential in the middle of the conduction channel of the FET (V_c). V_c doesn't represent the recorded potential of the cellular membrane. For an FET, the real cellular potential needs to be converted from the recorded conduction channel current and the transconductance of the FET calculated in the water-gate measurements. With closer proximity to the cell, the cell membrane spontaneously fuses with the phospholipid coating on the FET, realizing biological entrance of the FET and intracellular sensing of the transmembrane potential. These models were built based on widely adopted electrical models of cell membranes and FET[81]. The extracellular signals are attenuated and distorted by the membrane impedance, showing a distinct shape to the intracellular signals.

The equivalent circuit model reveals an attenuated signal (V_c) due to the membrane impedance (R_m and C_m) and the shunt via the small spreading resistance (R_s). As the FET

approaches the cell, the phospholipid coating spontaneously fuses with the cell membrane with minimal invasiveness to the cell, realizing intracellular sensing. The tight interfacial sealing maximizes the spreading resistance R_s (i.e., minimizes leakage current).

2.9 Fabrication of The Multi-Electrode Array (MEA).

The multi-electrode array, composed of Au electrodes, an SU-8 insulation layer, and a glass substrate, was fabricated using the standard micro/nanofabrication techniques.

The MEA in this study had multiple conductive electrodes that were extracellularly contacting cellular membranes and recording the membrane potentials. We used these devices to verify the cardiomyocytic electrophysiological activities. The collected extracellular signals served as a control for those recorded by the FET.

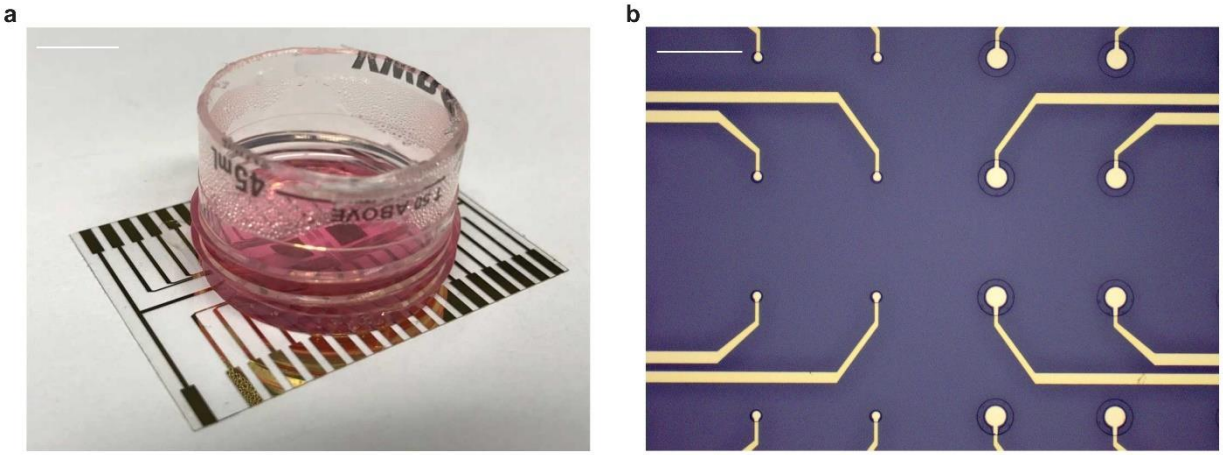

Figure 40. Fabrication of a MEA.
a, A picture of the MEA with a customized container filled with the Claycomb Medium for HL-1 cell growth. Cells are growing on the MEA surface inside the tube for 3–4 days in an incubator at 37 °C, 5% CO_2 before they reach confluency. Scale bar: 10 mm. **b,** A closeup optical microscope image showing the metal pads and the covered connection wires by a layer of insulating SU-8. Only the circular areas of the metal pads are exposed to contact the cells. Scale bar: 200 μm.

The first step was to clean cover glass slides (35 mm by 50 mm by 0.13–0.16 mm; FisherbrandTM) to remove all organic contaminants and particles in stabilized sulfuric acid and hydrogen peroxide mixture solution (Nano-Strip; VWR International, heating up to 80 °C for half an hour), followed by rinsing with DI water and drying with nitrogen gas.

A lift-off process allowed forming metal connection patterns on the glass slides. The process involved photolithography (photoresist NR-3000PY: spin-casting at 4,000 r.p.m. for 60 s, baking on a hotplate at 150 °C for 60 s, UV irradiance at 220 $mJ \cdot cm^{-2}$, post-exposure baking at 100 °C for 60 s, and developing for ~20 s with developer RD6) and then sputtering (chromium: 200 W, 3.0 mTorr, 5 sccm Ar, 30 s, ~5 nm; gold: 200 W, 3.0 mTorr, 5 sccm Ar, 5 min, ~100 nm). The samples were soaked in acetone overnight to thoroughly remove all photoresists and lift off the metals on the top of the photoresists.

A thin layer of SU-8 was coated to insulate most of the metal wires and only expose the metal electrode pads, by photolithography (SU-8 2000.5: spin-casting at 4,000 r.p.m. for 30 s, baking on a hotplate at 95 °C for 60 s, UV irradiance at 100 $mJ \cdot cm^{-2}$, post-exposure baking at 95 °C for 60 s, and developing for ~60 s with SU-8 developer). Hard baking at 180 °C for an hour cured the SU-8 completely so that the SU-8 was safe and compatible with cells during measurements.

A conical centrifuge tube (FalconTM) was cut at 3 cm apart from the threaded dome. The flat top surface was adhered to the center of the MEA using a low toxicity silicone adhesive (Kwik-SilTM, World Precision Instruments) to build a container for the cell culture medium.

We used silver epoxy (8831, MG Chemicals) to connect the metal leads of the MEA to flexible cables and the backend circuit. The device was sterilized in 70% ethanol for 5 hours before use.

2.10 Conclusion.

In this chapter, we elaborate on the comprehensive method to fabricate the soft FET array. Using the conventional micro/nanofabrication techniques made the multilayered precursor on a planar substrate. A unique transfer printing and compressive buckling technique realized the 3D structure of the FET array. Electrical characterization of the FET shows it has excellent sensitivity and small noise, which are the prerequisite of sensing cellular electrical activities, especially subthreshold membrane potentials. We also introduced a method to functionalize the FET surface by application of phospholipid bilayer materials, which greatly facilitate the internalization process of the FET into the cell body.

Chapters Two, in full, is a partial reprint of the materials: 'Three-dimensional transistor arrays for intra- and inter-cellular recording, Yue Gu, Chunfeng Wang, Namheon Kim, Jingxin Zhang, Tsui Min Wang, Jennifer Stowe, Rohollah Nasiri, Jinfeng Li, Daibo Zhang, Albert Yang, Leo Huan-Hsuan Hsu, Xiaochuan Dai, Jing Mu, Zheyuan Liu, Muyang Lin, Weixin Li, Chonghe Wang, Hua Gong, Yimu Chen, Yusheng Lei, Hongjie Hu, Yang Li, Lin Zhang, Zhenlong Huang, Xingcai Zhang, Samad Ahadian, Pooja Banik, Liangfang Zhang, Xiaocheng Jiang, Peter J. Burke, Ali Khademhosseini, Andrew D. McCulloch, Sheng Xu, accepted in Nature Nanotechnology, 2021'. The dissertation author was the first author of this paper.

Chapter 3. Electrophysiological Recordings of Single Cells.

3.1 Cardiomyocytes Cultivation.

We followed the standard cell culture protocol provided by Sigma-Aldrich. All materials and solutions were from Sigma-Aldrich. The cells were cultivated in the supplemented Claycomb medium after pre-coating the substrates with templating materials. We prepared the cell cultures on PDMS sheets for signal recording, on cell culture flasks for cell proliferation, and on cell culture dishes for Ca^{2+} sparks screening.

The HL-1 cardiomyocytes were purchased from Sigma-Aldrich, in Figure 41. To prepare the cells for signal recordings, the cells were cultivated on thin PDMS sheets (base material: curing agent = 10:1; prepared by spin-casting the mixed precursors on a 4-inch wafer at 500 r.p.m. for 60 s, baking in a convection oven at 80 °C for 4 hours).

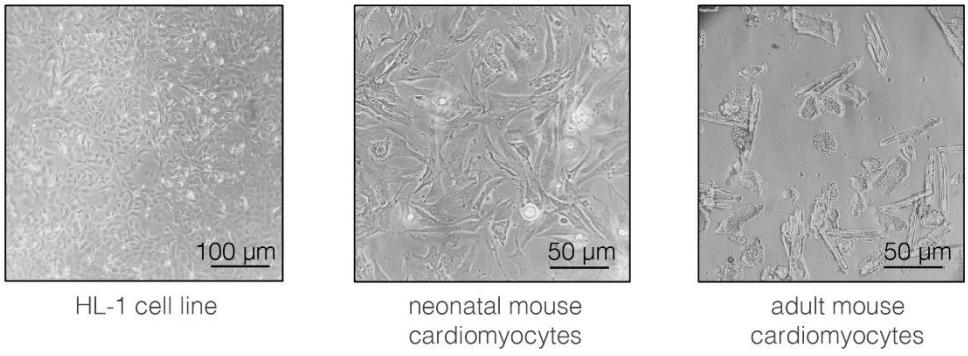

Figure 41. Optical images of a cell line and two primary cells in this work.
HL-1 cell line and cardiomyocytes of the neonatal or adult mouse were used in this work. They were cultivated on glass coverslips or PDMS membranes.

Before cell plating, the PDMS sheet was cut into 3 cm by 3 cm square and placed in a 35 cm cell culture dish. The PDMS sheet was soaked in 70% ethanol for 30 min, followed by

ultraviolet sterilization for 1 hour. Fibronectin/Gelatin (5 μg·ml^{-1} fibronectin in 0.02% gelatin solution, 1 ml) was coated on the pre-treated PDMS surface for at least 1 hour before seeding the cells.

After removing the coating agent, the cells (at a density of ~1 × 10^5 cm^{-2}) were plated and maintained in the supplemented Claycomb medium (10% fetal bovine serum, norepinephrine 0.1 mM, L-Glutamine 2 mM, and penicillin/streptomycin 100 U·ml-1/100 μg·m^{-1}, 2 ml) in an incubator at 37 °C and 5% CO_2. The cell culture medium was replaced by a 2 ml fresh medium every day until the cells reached confluency in 3–4 days.

Sterilizing the MEA and the FET before plating the cells followed the same procedure as the abovementioned. Fibronectin/Gelatin was coated on the MEA surface before cell seeding to enhance cell attachment.

Neonatal mouse ventricular myocytes were isolated from 1~2-day old Black Swiss mouse pups purchased from Charles Rivers Labs. Adult mouse single ventricular myocytes were isolated from the mouse ventricles using the enzymatic digestion method by Langendorff. The cells were obtained by digesting the ventricles in buffered solutions. After removing the fibroblast cells and blood from the vasculature, the cardiomyocytes were cultured on laminin templated PDMS sheets or cell culture dishes for signal recordings.

The neonatal mouse ventricles were predigested in HBSS (Hank's Balanced Salt Solution) (0.5 mg·ml^{-1}) containing Trypsin (0.5 mg·ml^{-1}) at 4 °C on an orbital shaker at 80 r.p.m. for overnight, and then were thoroughly digested in collagenase (330 U·ml^{-1}) and HBSS (0.8 mg·ml^{-1}) mixed solution.

Isolated cells were suspended in the cell culture medium (Dulbecco's Modified Eagle Medium: M199 = 4:1 in volume, penicillin/streptomycin 120 $U \cdot ml^{-1}$/100 $\mu g \cdot m^{-1}$, L-Glutamine 2 mM, HEPES 10 mM, 10% Horse Serum, 5% Fetal Bovine Serum). The cells were plated in a T-75 flask to remove the adherent fibroblast cells.

The suspended cardiomyocytes were transferred to a PDMS sheet in a 35-cm dish pre-coated with laminin (1 $\mu g \cdot ml^{-1}$ laminin in sterile 1X PBS). The cells were incubated at 37 °C in a humidified incubator with 10% CO_2. The medium was replaced on a daily basis.

Adult mouse hearts were isolated via aortic perfusion with a buffered perfusion solution (NaCl 113 mM, Na_2HPO_4 0.6 mM, $NaHCO_3$ 12 mM, KCl 4.7 mM, $KHCO_3$ 10 mM, KH_2PO_4 0.6 mM, $MgSO_4 \cdot 7H_2O$ 1.2 mM, HEPES 10 mM, Taurine 30 mM, phenol red 0.032 mM, glucose 5.5 mM, temperature = 37 °C; pH = 7.35 with NaOH) to fully remove all blood from the vasculature. A 1mg/mL collagenase type 2-containing digestion buffer digested the matrix of the heart during perfusion at a rate of 3 $ml \cdot min^{-1}$. Once the heart was sufficiently digested, the ventricles were removed and minced with scissors before being triturated in a warmed solution (90% perfusion solution, 10% fetal bovine serum, 12.5uM calcium chloride) with a transfer pipette. Cells were strained through 100 μm mesh and stepwise, slowly brought to 1mM calcium concentration. Then they were transferred to a 35 cm dish pre-coated with laminin (1 $\mu g \cdot ml^{-1}$ laminin in sterile PBS solution). The cells were incubated at 37 °C in a humidified incubator with 5% CO_2 for 4 hours before measurements.

To test the cytotoxicity of the FET or MEA devices to the cells, we performed a live/dead assay with FET or MEA devices placed with cells for a certain period of time.

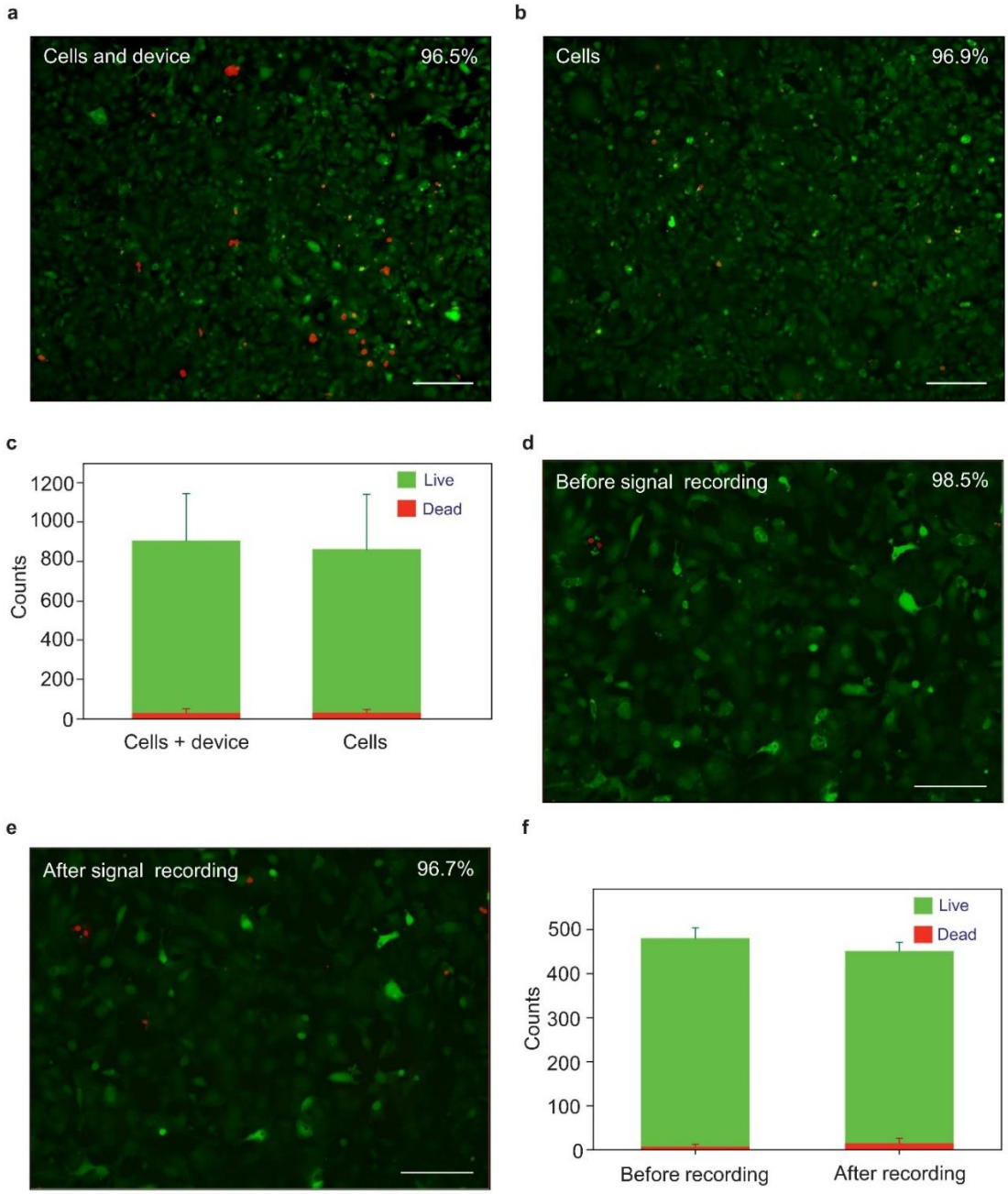

Figure 42. Tests of cell viability.

a,b, Confluent HL-1 cells (**a**) with and (**b**) without an FET device in the culture for two days. Fluorescent imaging results of live (green)/dead (red) cells show ~97% viability in these confluent cell cultures. **c,** Statistics of 8 cell cultures show that the FET has no cytotoxicity to the cells. **d,e,** Fluorescent imaging results of the same region of a confluent HL-1 cell culture (**d**) before and (**e**) after signal recording with 98.5% and 96.7% of cells alive, respectively. The FET shows little harm to the cells. **f,** Statistics of 3 cell cultures show that the recording process has negligible cytotoxicity to the cells. All scale bars: 200 μm.

Cell viability test results proved that neither the construction materials nor the signal recording of the FET showed cytotoxicity towards HL-1 cardiac muscle cells (Figure 42).

3.2 Verification of Cell's Electrical Properties.

A Ca^{2+} spark assay confirmed the HL-1 cells' electrophysiological activities (Figures 43 and 44).

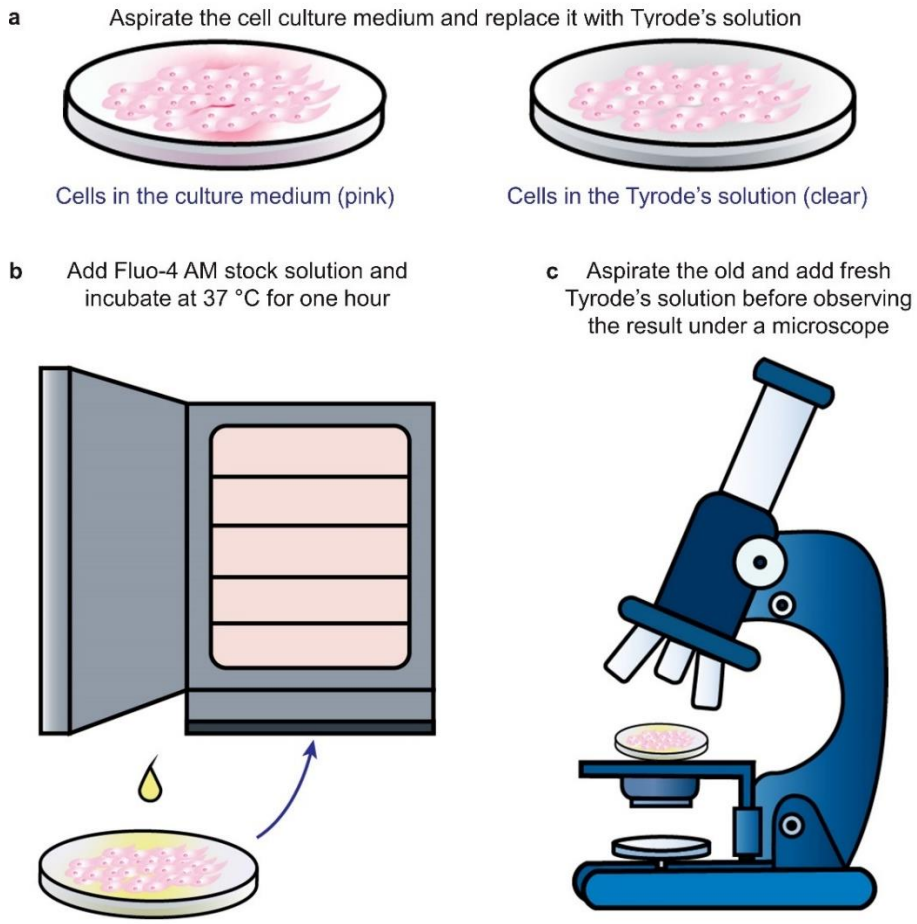

Figure 43. The schematic process of Ca^{2+} sparks screening assay.
a, HL-1 cells are cultured in a petridish filled with the supplemented Claycomb medium. The medium is removed by aspiration and Tyrode's solution is added with Ca^{2+} and glucose (pH: 7.35 at 37 °C). **b,** The Fluo-4 AM stock solution is added in the cells that are incubated for one hour. After that, the old solution is aspirated, and the fresh Tyrode's solution is added. **c,** Fluorescent Ca^{2+} sparks can be immediately observed under a microscope.

Figure 43 illustrate the process of staining Ca^{2+} and monitoring their transient activities under the fluorescent microscope.

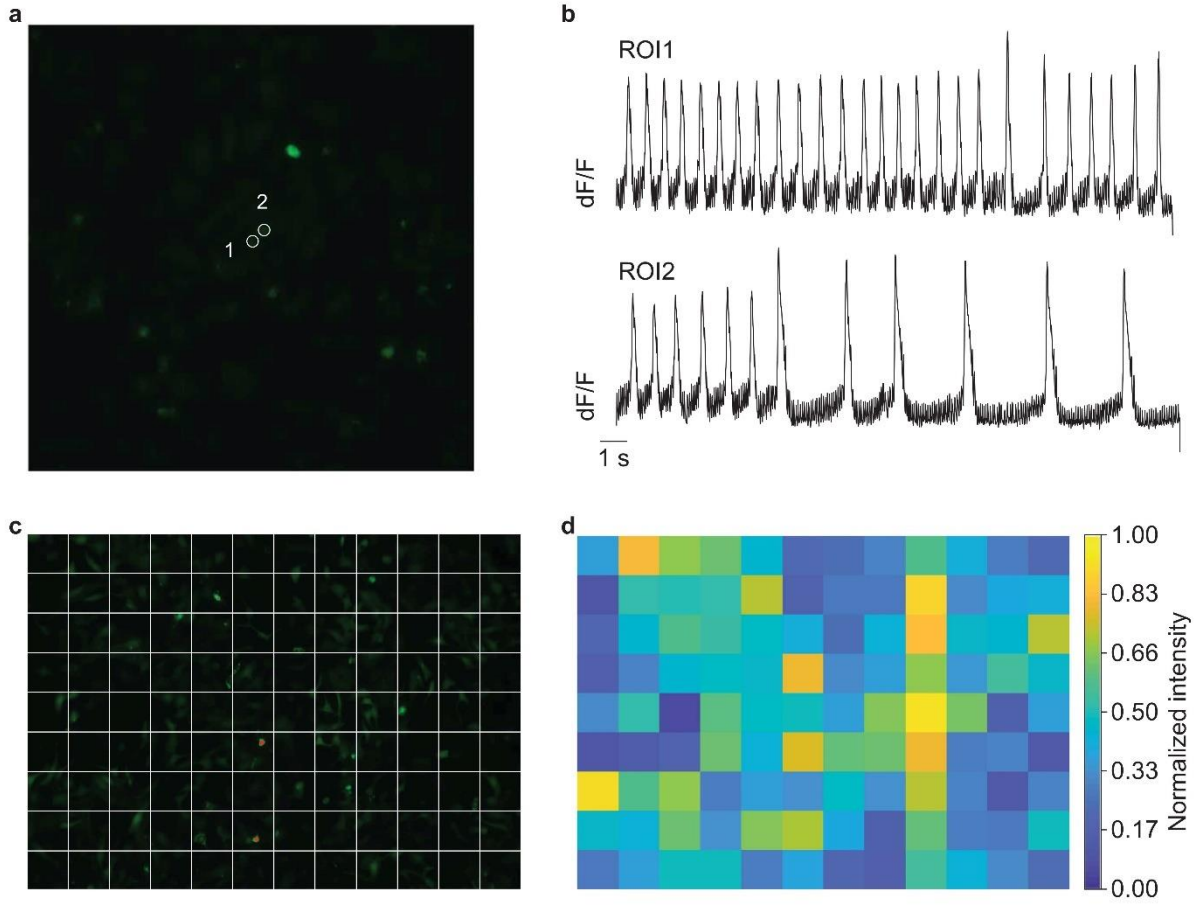

Figure 44. Ca^{2+} sparks assay illustrating HL-1 cells' action potentials and mapping field potentials in the whole cell culture.

a, A single snapshot from a video of an HL-1 cell culture stained with the Fluo-4 AM fluorescent dye. Two circles outline the two regions of interest (ROIs) to be analyzed, as marked by 1 and 2. **b,** Quantitative fluorescent intensity analysis of the ROI1 and ROI2 showing the transient Ca^{2+} signals. Quantifications are performed on stacked snapshots extracted from the video, which would clearly illustrate the spiking rate and the signal conduction pathways in the whole 2D cell culture. Calculating the fluorescent intensities of ROI1 and ROI2 of every snapshot provides the digitized fluorescent intensity to render the plot. **c,** Mapping the fluorescent intensities of the whole observation region reveals the positions that are showing the Ca^{2+} sparks at the corresponding time to that image. Quantification and replotting the fluorescent intensity amplify the intensity contrast for displaying the Ca^{2+} distribution. Each snapshot is sectioned into 12 by 9 ROIs, and each ROI's average fluorescent intensity is digitized. **d,** A heatmap showing the quantified intensity results of the image in (**c**). The Ca^{2+} sparks appear in those yellow regions.

First, the HL-1 cells were cultured in a supplemented Claycomb medium. We removed the cell culture medium by aspiration and added clear-color typical Tyrode's solution. Second, we added the Fluo-4 AM (InvitrogenTM) stock solution to the cells and incubated it for an hour to facilitate the loading of calcein dyes. Then, we removed the old solution and refilled it with fresh Tyrode's solution. Finally, we monitored the Ca^{2+} signals under a microscope with a 480 nm excitation filter and a 525 nm emission filter.

To quantify the fluorescent imaging results, we extract many frames from the captured video and analyze the light intensity of selected regions, called the region of interest (ROI). By plotting the quantified values of the same region from a series of frame images, we can plot a curve of the signal magnitude change with time, shown in Figure 44b. We can also perform the quantification analysis on the whole frame. To do so, we divided the frame into 12 by 9 regions, and each region is regarded as a pixel. The light intensity of individual pixels was calculated and analyzed on each frame. A heatmap in Figure 44d shows the normalized fluorescent intensity of each pixel. After we recombine these heatmaps, we can clearly see the signal propagation path by tracking the position of the highest intensity in yellow color.

In conclusion, quantification and replotting the fluorescent intensity amplifies the intensity contrast for displaying the Ca^{2+} distribution. Each snapshot is sectioned into 12 by 9 ROIs, and each ROI's average fluorescent intensity is digitized.

3.3 Sensing Intracellular and Extracellular Potentials of Cardiomyocytes.

Full-amplitude signals contain quantitative information on ionic activities inside the cell[30,41,44]. The full amplitude depends on many factors, including the type, culture conditions, and physiological status of the cell[41,44,45]. The FET arrays in this work can measure full-amplitude signals comparable to those acquired by the whole-cell patch-clamp[41,82].

Whole-cell current patching on HL-1 cells and primary cardiomyocytes were performed at 35 °C with cells plated on a PDMS sheet superfused with an external solution (Figure 44). A glass micropipette filled with the solution in the lumen was attached to the cell membrane, forming a giga-seal. After that, the membrane patch got ruptured by negative pressure in the pipette, which established the whole-cell configuration. Action potentials were recorded with a holding potential at -80 to -40 mV and evoked by injecting currents to the cells.

Whole-cell current patching on HL-1 cells and primary cardiomyocytes were performed with external solution (for all types of cells: NaCl 140 mM, KCl 4 mM, $MgCl_2$ 1 mM, HEPES 10 mM, glucose 10 mM, temperature = 37 °C; for HL-1 cells: $CaCl_2$ 1.8 mM, pH = 7.35 with NaOH; for primary cells: $CaCl_2$ 1.0 mM, pH = 7.4 with NaOH).

Glass pipettes were pulled from borosilicate glass using a micropipette puller (Model P-87, Sutter Instrument Co.). The as-pulled glass pipettes were then filled with an internal solution (NaCl 10 mM, KCl 10 mM, K-Aspartate 120 mM, $MgCl_2$ 1 mM, HEPES 10 mM, MgATP 5 mM, pH = 7.2 with KOH). The glass pipettes had an average impedance of 2–5 MΩ measured in the cell medium bath.

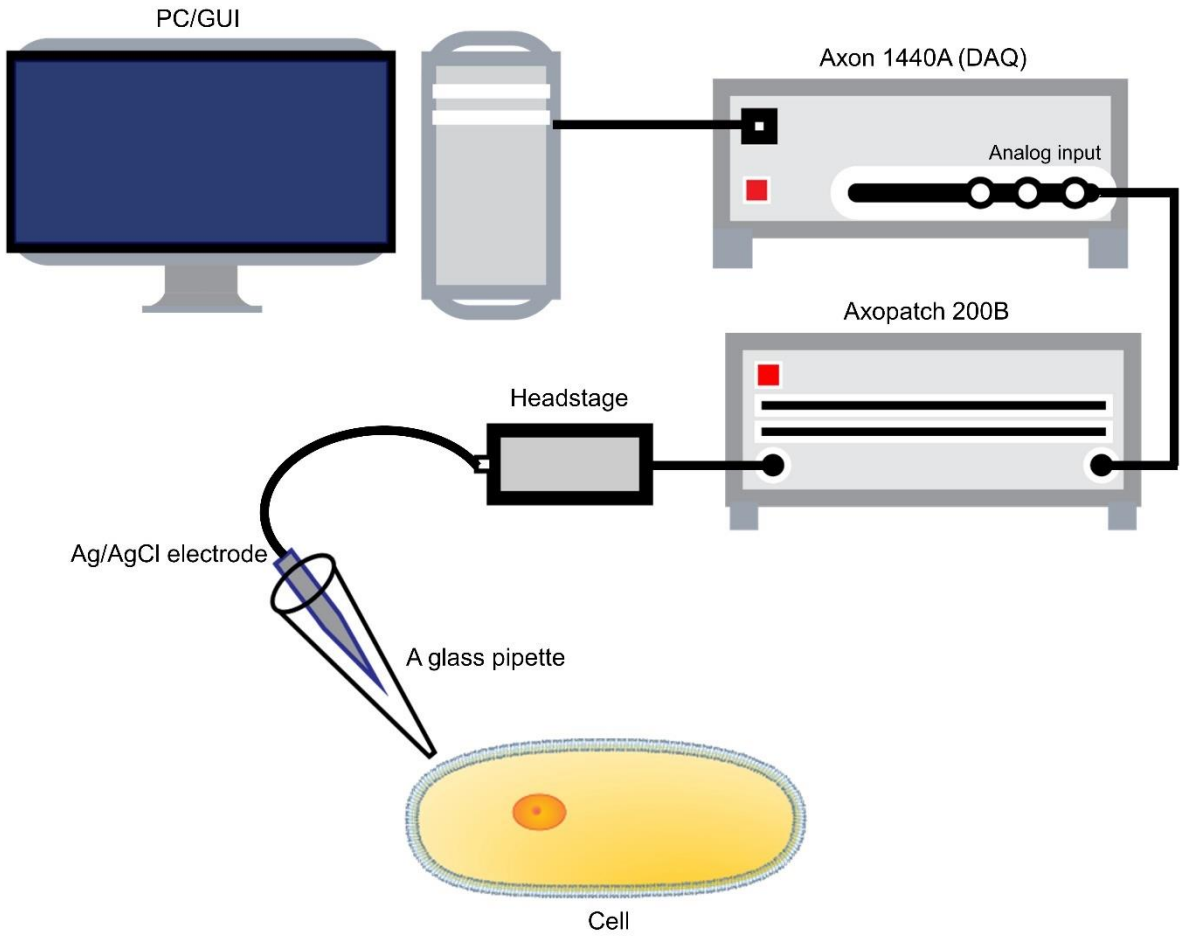

Figure 45. The schematic experimental setup of using the patch-clamp to record intracellular signals of a single cell.

The setup includes a computer that installs a commercial program (Axon pCLAMP 10 Software Suite), which is used to acquire, convert, and display the analog signals from the cells. The computer is connected with a DAQ that can realize digital to analog or analog to digital signals conversion. One of the DAQ's analog input channels is connected to a commercial preamplifier (Axopatch 200B). The preamplifier's input is linked to a headstage that can eliminate the system noise and stabilize the recorded signals from an Ag/AgCl electrode. The Ag/AgCl electrode is housed in a glass pipette of as small as 1 μm in tip size. The pipette is filled with saline solution. The small pipette tip can clamp to a small patch of the cellular membrane. The whole-cell patch is performed when the cellular membrane at the patch gets ruptured and a giga-seal is formed between the pipette and cellular membrane.

Junction potentials were zeroed before the formation of the membrane–pipette sealing. Several minutes after the seal was formed, the membrane was ruptured by gentle suction to establish the whole-cell configuration for current clamping. Cell capacitance was measured by

integrating the capacitive transient evoked by applying a 5 mV hyperpolarizing step from a holding potential of -40 mV.

Figure 45 illustrates the electrical system of the patch-clamp platform, including an Ag/AgCl electrode connected with a headstage for amplifying the recorded signals by a feedback circuit. The headstage connected to an amplification system (Axonpatch 200B) and a data digitalization module (DigiData 1440A, Axon). Current-clamp command pulses were generated by a digital-to-analog converter (DigiData 1440A, Axon) controlled by the pCLAMP software (10.3, Axon). After the cells were stimulated by an injection current, action potential spikes could be recorded and shown in the GUI.

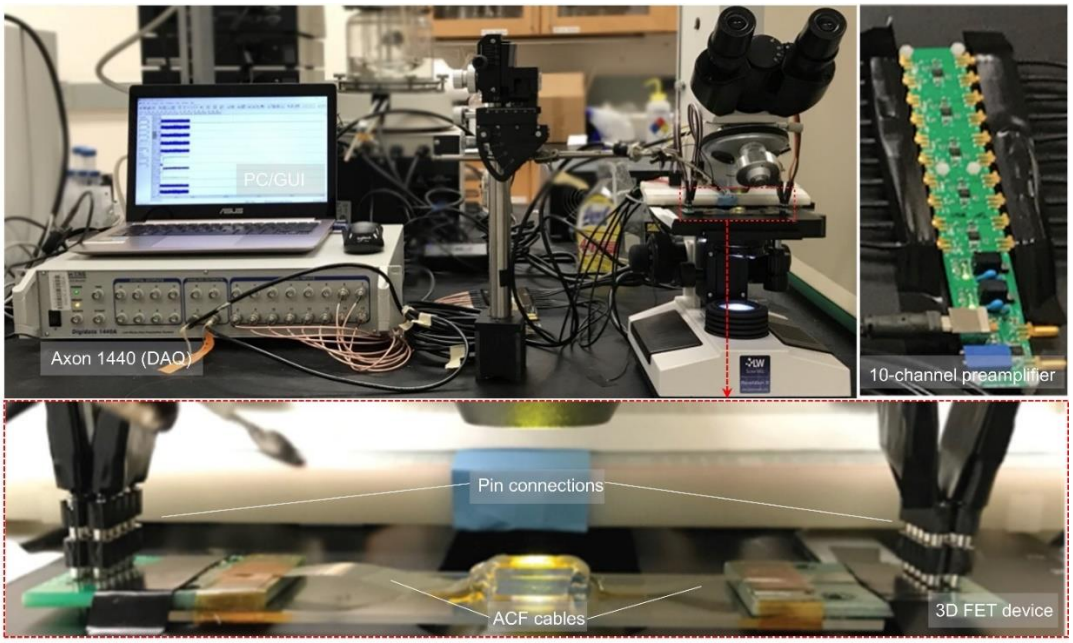

Figure 46. Pictures of the experimental setup for cellular electrophysiology recording using the arrayed FETs.
Using an ACF cable, the FET array is connected to the amplifier, analog-to-digital converter (ADC), and PC sequentially. During measurements, we can either place a sheet of PDMS with cardiomyocytes on the FETs or fix the FET to a manipulator and approach to cell cultures in the dish. During signal recording, an Ag/AgCl electrode is inserted into the culturing solution to maintain the extracellular potential at zero bias.

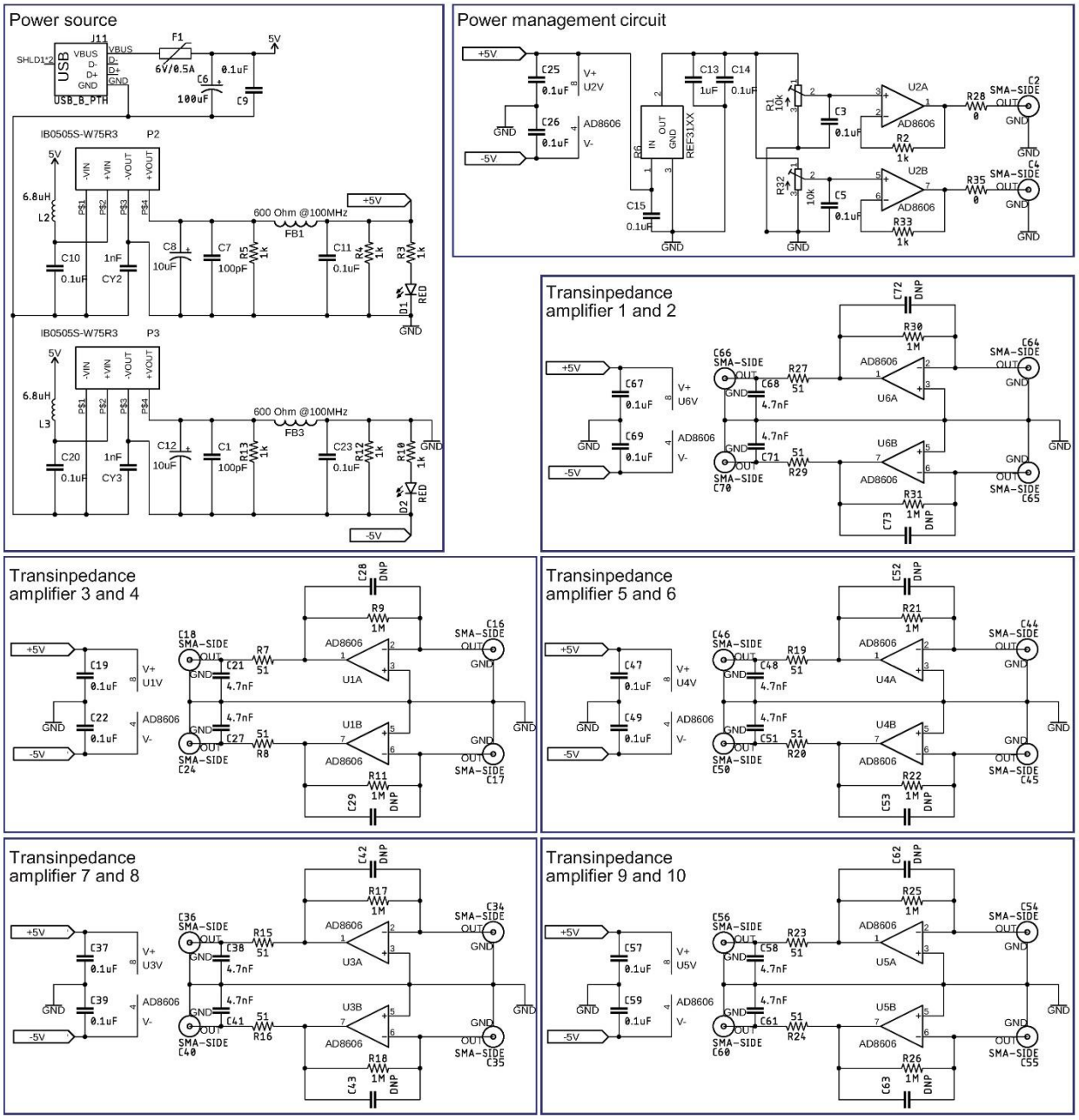

Figure 47. The circuit design of the customized 10-channel current preamplifier.

The current amplifier contains a USB power source and a power regulation circuit that can stably output +5 V and -5 V constant voltages to the entire circuit. A power management circuit is designed to stabilize the output voltage further to be +5 V or -5 V accurately. Also, it can regulate the output voltage to be in the range from 0 to 2 V. The amplifier circuit integrates ten independent transimpedance amplifier circuits that can function individually.

The experimental setup for sensing cellular electrophysiology by the 10-FET array consisted of a commercial DAQ system (DigiData 1440A) and a customized 10-channel preamplifier shown Figures 46 and 47. The setup was similar to that used for water-gate characterization, where cells were placed on the FET with a zero bias from the Ag/AgCl electrode. The sampling rates applied for the recordings were within the range from 10 to 100 kHz.

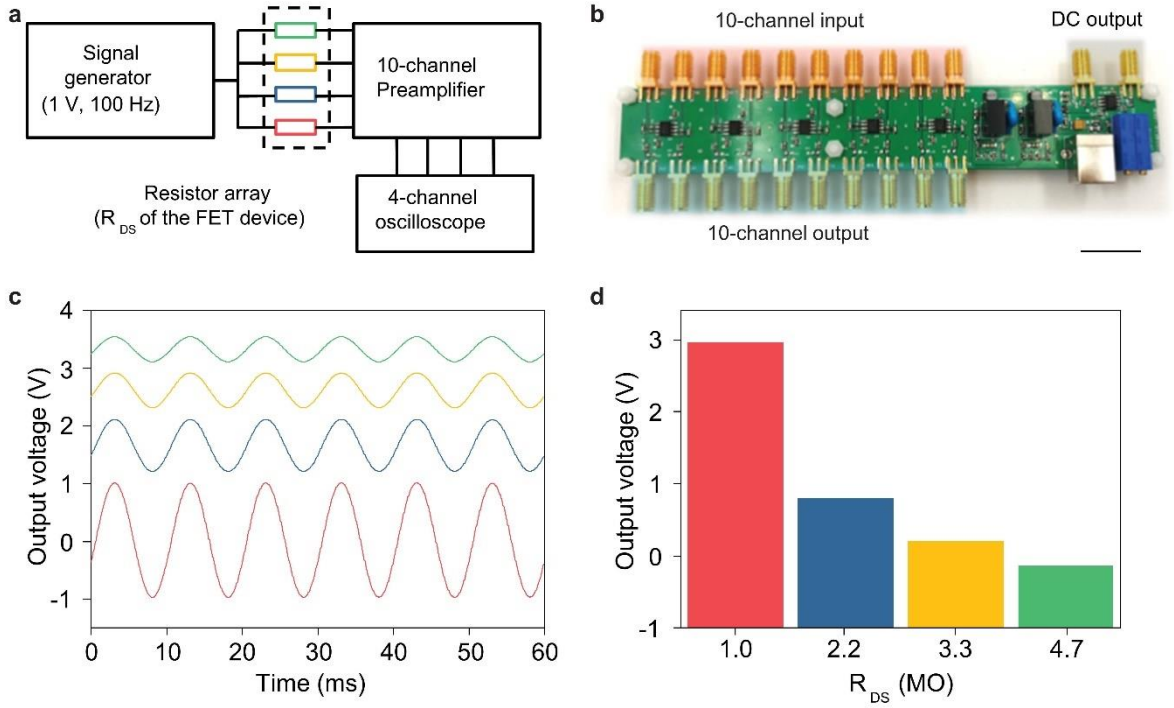

Figure 48. Electrical properties of the customized 10-channel current preamplifier.
a, The electrical setup to characterize the multi-channel amplifier. A generated signal is exerted on four parallelly connected resistors. The other ends are input into four different channels of the preamplifier. An oscilloscope displays the amplified and digitalized signals. **b,** A picture of the customized 10-channel preamplifier, labeled with input and output terminals. Scale bar: 2 cm. **c,** Amplified signals in corresponding colors. The amplitude differences are from the different values of the four resistors. **d,** The amplitude of each output signal is different from each other, which demonstrates the four channels are functioning independently, with no crosstalk.

Electrical characterization showed no crosstalk between different channels in the preamplifier (Figures. 48-50).

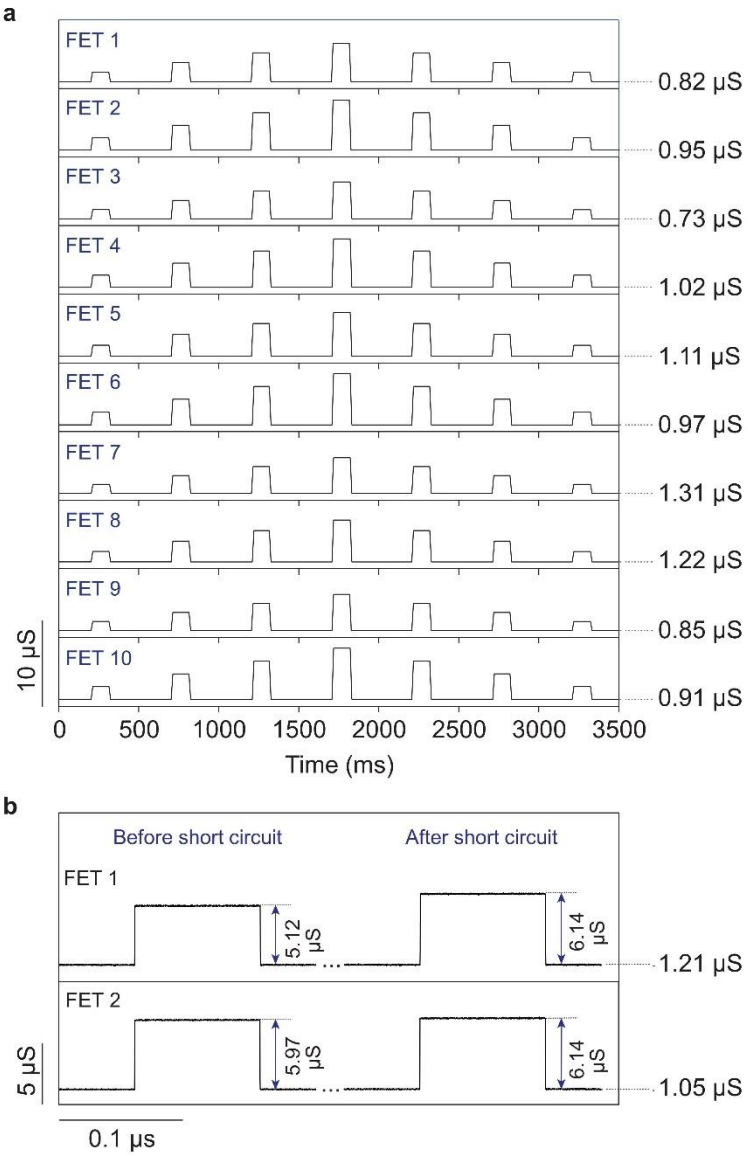

Figure 49. Verifying the arrayed FET device's crosstalk.

a, The same signal, containing seven pulses (from 100 mV to 400 mV and then back to 100 mV, with a step size of 100 mV, rising/falling time of 0.1 ms, duration of 100 ms), is applied to the gate solution of all 10 FETs. Each FET is separately connected to an individual channel of the preamplifier. The 10 responses recorded by the 10 FETs show different signal amplitudes, illustrating the variance of their sensitivities. The conductance of each FET under zero gate potential is shown in the far-right column. Each FET is recording signals independently, with no crosstalk during operation. **b,** When two FETs are shorted, their recordings become identical, which further proves that those small signal latencies result from the cellular activities.

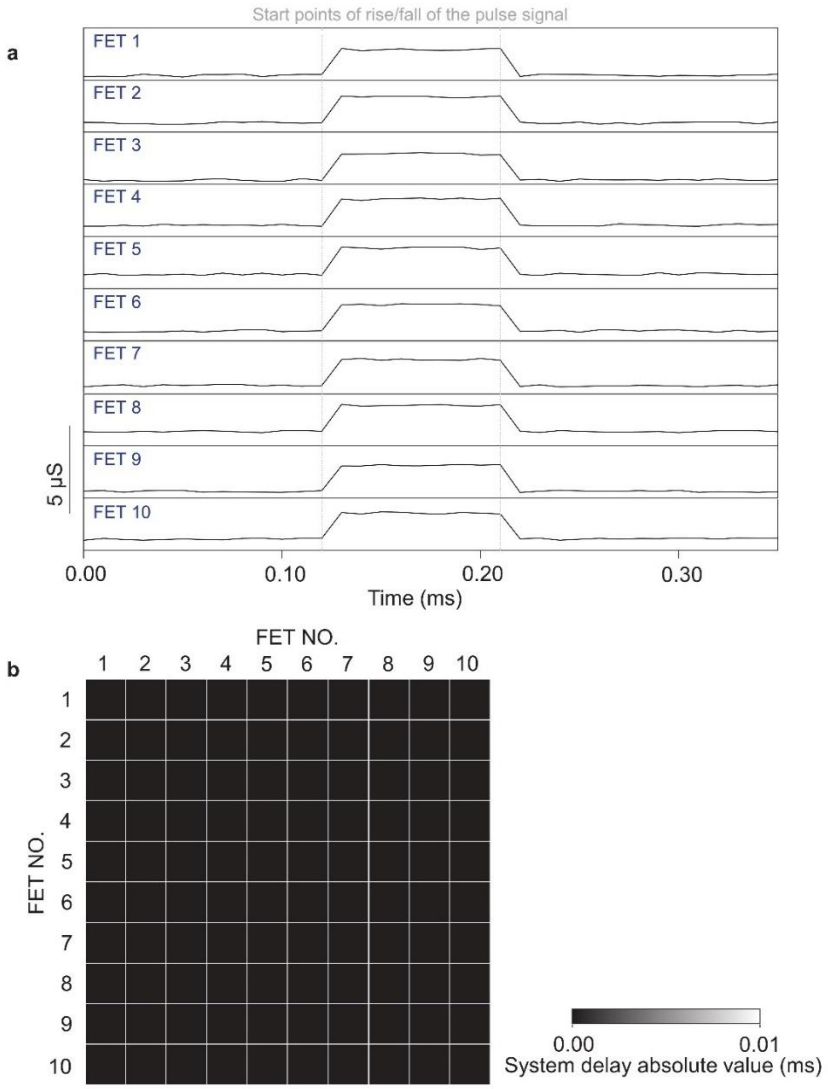

Figure 50. Characterization of the electrical signal delay introduced by the measurement system.

The same method as that used to characterize an FET's temporal response to dynamic signals is adopted to measure the delay between any two FETs in an array. A 100-mV pulse (rising/falling time of 0.01 ms, duration of 0.1 ms) is applied on a 10-FET array. The FETs' responses to the input pulse signal are simultaneously recorded at a 100 kHz sampling rate. **a,** Responses of the 10-FET array to the same input signal showing each FET is working independently. The dash lines mark the starting points of the rise and fall edges of the pulse. **b,** The cross-correlation method is used to calculate the latencies between any two channels showing that the system delay over the whole device is negligible. It proves that multiple FETs in an array exhibit the same characteristics to dynamic signals. Further, the system-induced electrical delay is negligible compared to those generated from cellular ionic dynamics.

By hooking up the preamplifier to the DAQ, PC, and the 10-FET array, each FET in the array operates independently, showing no crosstalk with each other (Figure 50).

The DAQ system consisted of a DDC264 (Texas Instruments) and a customized acquisition interface to the evaluation board (Figure 51).

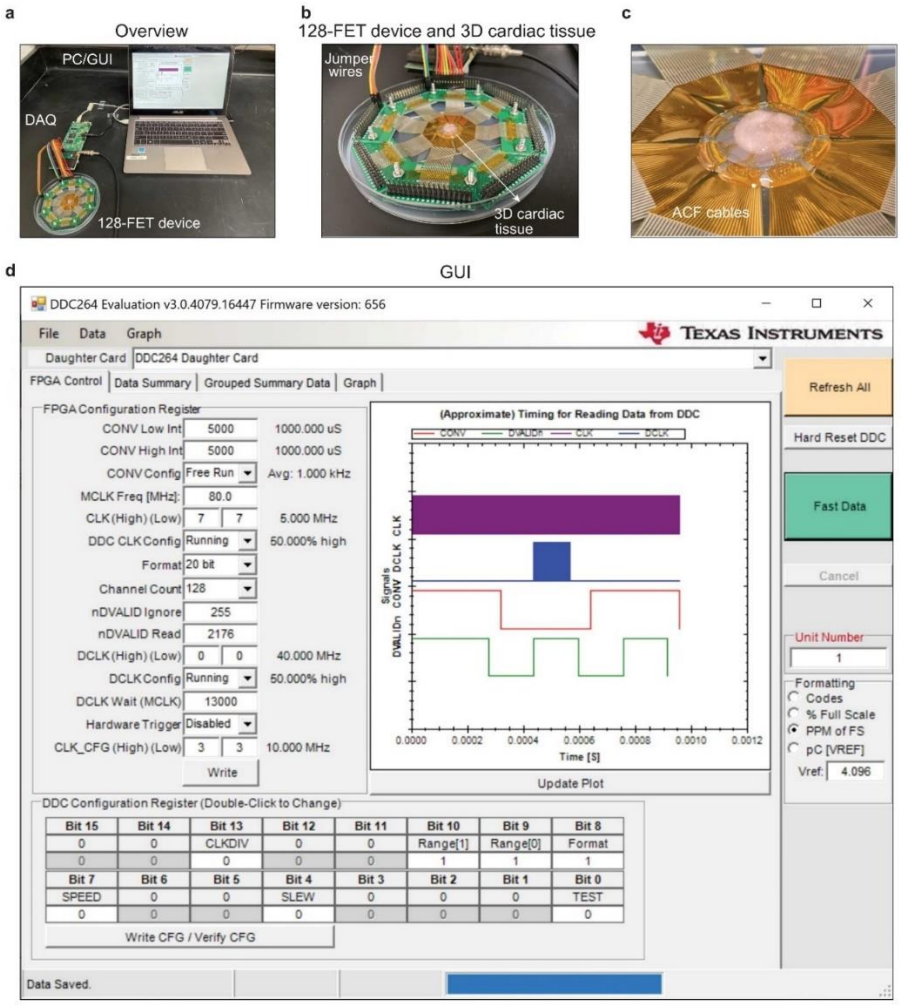

Figure 51. Pictures of the experimental setup of recording electrophysiology of the 3D cardiac tissue by the 128-FET array.

a, The measurement setup includes a 128-FET array connected to a flexible print circuit (FPC, uxcell) with flexible ACF cables, a customized DAQ board (Texas Instruments DDC264), and a GUI (provided by Texas Instruments). **b,** A closeup of the 128-FET array interfacing a 3D cardiac tissue. Signals transmit from the front-end sensors to the DAQ board via jumper wires. **c,** The 128-FET array fans out to the external circuits via flexible ACF cables. d, The DDC264 evaluation software is the interface used to command the DAQ board for data acquisition and storage.

The DAQ was connected to the FET sensor arrays using ACF cables and an adaptive printed circuit board. Customized software (Texas Instruments) controlled the DAQ system. All recordings by the 128-FET array in this study used a sampling rate of 500–1,000 Hz, which was large enough to ensure the signal's fidelity, and small enough to meet the limited capacity of the chip memory for onboard data storage.

Full-amplitude action potentials were stably recorded by both the FET and a whole-cell patch-clamp (Figures. 52 and 53).

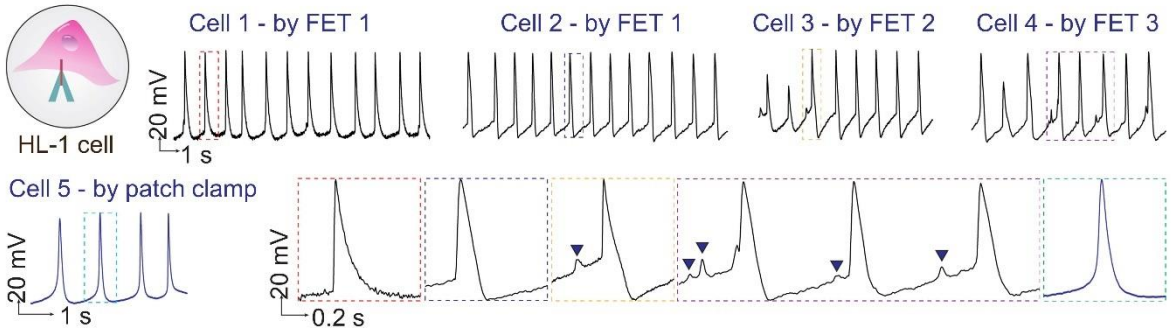

Figure 52. Intracellular recordings on HL-1 cells.
Periodic spikes can be recorded from different HL-1 cells by different FETs (top panels). The results are validated using the whole-cell patch (lower left panel). Enlarged regions of the recordings by the FET and the patch-clamp represent typical pacemaker action potentials of the HL-1 cells (lower right panels). The mean and standard deviation of the action potentials measured by the FET are 121.4 ± 1.3 mV, which are close to the 122.0 ± 4.0 mV measured by the patch-clamp, showing the FET's capability for recording full-amplitude action potentials. Sub-threshold signals (e.g., cell membrane oscillations of 5~15 mV) are captured in the recordings of cells 3 and 4, as highlighted by the black triangles.

The amplitudes, morphologies, and firing patterns of the acquired potentials by those two techniques highly correspond to each other, showing the ideal coupling and faithful recording of the intracellular signals by the FETs.

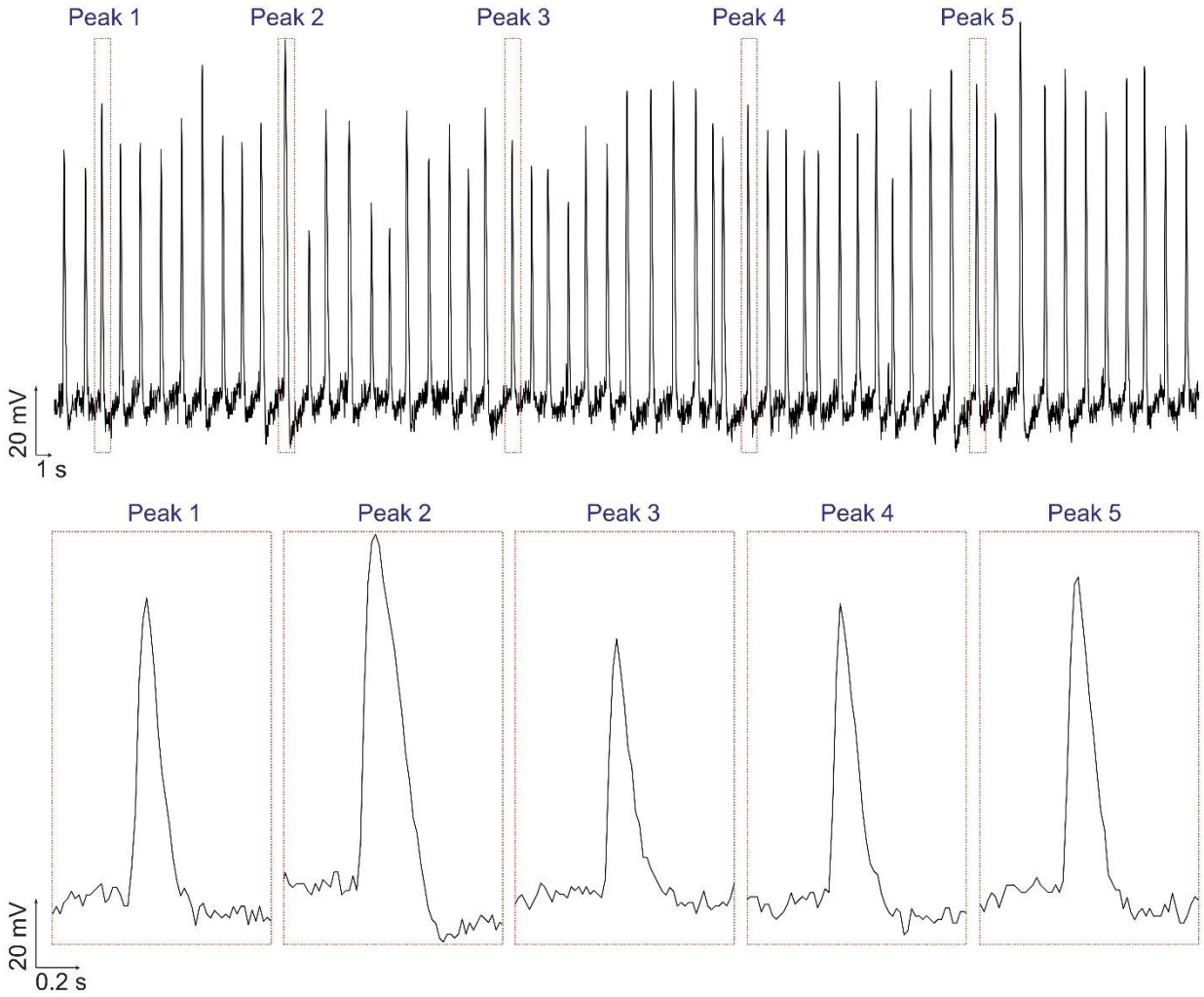

Figure 53. Extended intracellular recordings of an HL-1 cell.
Intracellular recordings of an HL-1 cell can maintain stable with periodic spikes for 71 seconds. The cells' activities are influenced by temperature, solution pH, and/or ion concentration disturbance during the measurement, which typically limit the possibility of long-time monitoring. What we demonstrate here is a considerably long duration among all reported active FETs for intracellular recordings[45,82].

The minor discrepancies are within the standard fluctuations due to differences in cellular physiology and measurement setups[12,45]. Cells show different physiological characteristics even though they are of the same type or even in the same cell culture. For example, in the same culture, some cells are contractile, but some are not; also, some cells are spontaneously firing action

potentials, but some are not. Their actual action potential shapes of different cells would have slight differences as well[83]. Plus, like a cancerous cell line, HL-1 cells would mutate during proliferation and reproduction, so their physiological characteristics would vary from different cell passages (i.e., how many times they have reproduced themselves)[84]. In different literature, the action potential morphologies of HL-1 cells were not identical[42,85-87].

Importantly, the FETs could record sub-threshold signals, due to their high sensitivity-to-noise ratios.

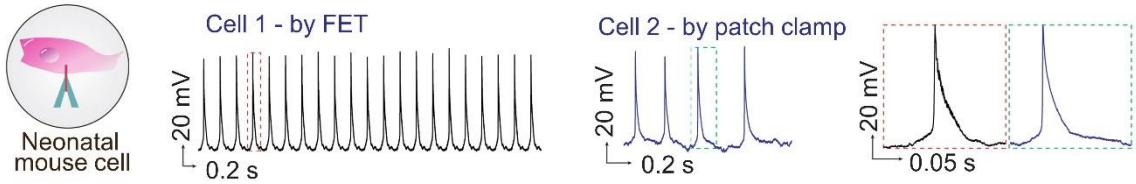

Figure 54. Intracellular recordings on neonatal mouse cells.
Intracellular recordings from neonatal mouse atrial cardiomyocytes.

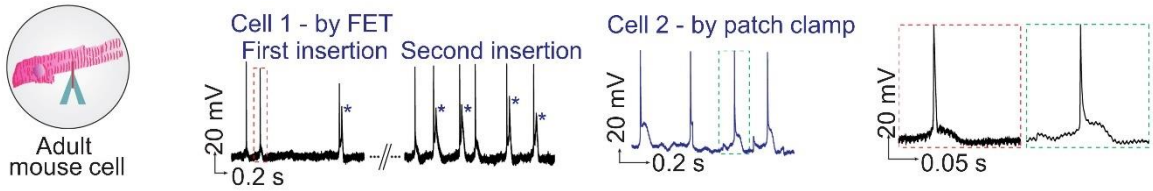

Figure 55. Intracellular recordings on adult mouse cells.
Intracellular recordings from adult mouse ventricular cardiomyocytes. The relatively larger noise is induced by the contraction of the adult mouse cells during measurements. In some spikes, an upstroke can be observed during repolarization, as marked by the asterisks, indicating abnormal Ca^{2+} influxes, which is also likely caused by the contraction.

Primary cells exhibit natural and primitive electrophysiological characteristics akin to their intrinsic states in live animals. The FET could record action potentials from spontaneously firing neonatal and adult mouse cardiomyocytes with results similar to those by the whole-cell

patch[12,28,83] (Figures. 54 and 55). The amplitude of each spike in the same recording fluctuates due to the contractile movements of the cells[82].

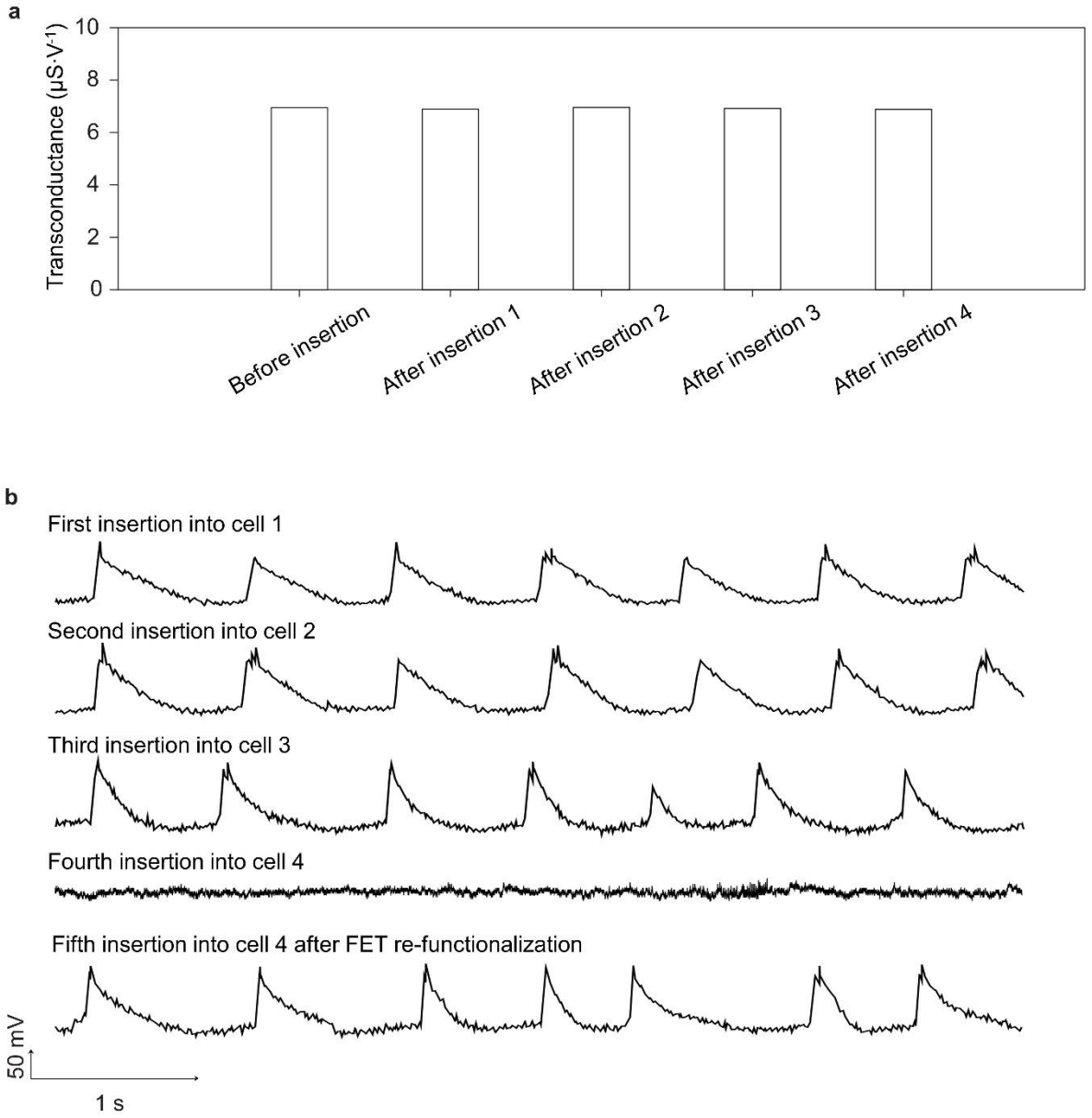

Figure 56. Durability test of functionalized FETs for intracellular recording.
a, The FET's transconductance was measured before the first and after each cell insertion, showing its stability. **b,** Intracellular recordings of four different cells show that cell insertion becomes unsuccessful after three cell insertions. After re-functionalization of the same FET, intracellular action potentials were obtained from the fourth cell, which revealed that the failed intracellular recording in the fourth insertion was because of the damaged lipid bilayer on the FET surface.

The phospholipid coating on the FETs plays a crucial role in intracellular recording. Continuous intracellular signal recordings on HL-1 cells could be extended to over 70 seconds (Figure 53), the longest reported by an intracellular FET sensor. A phospholipid coating could last through three times of cell insertion before re-functionalization was needed to fulfill a stable intracellular recording (Figure 56).

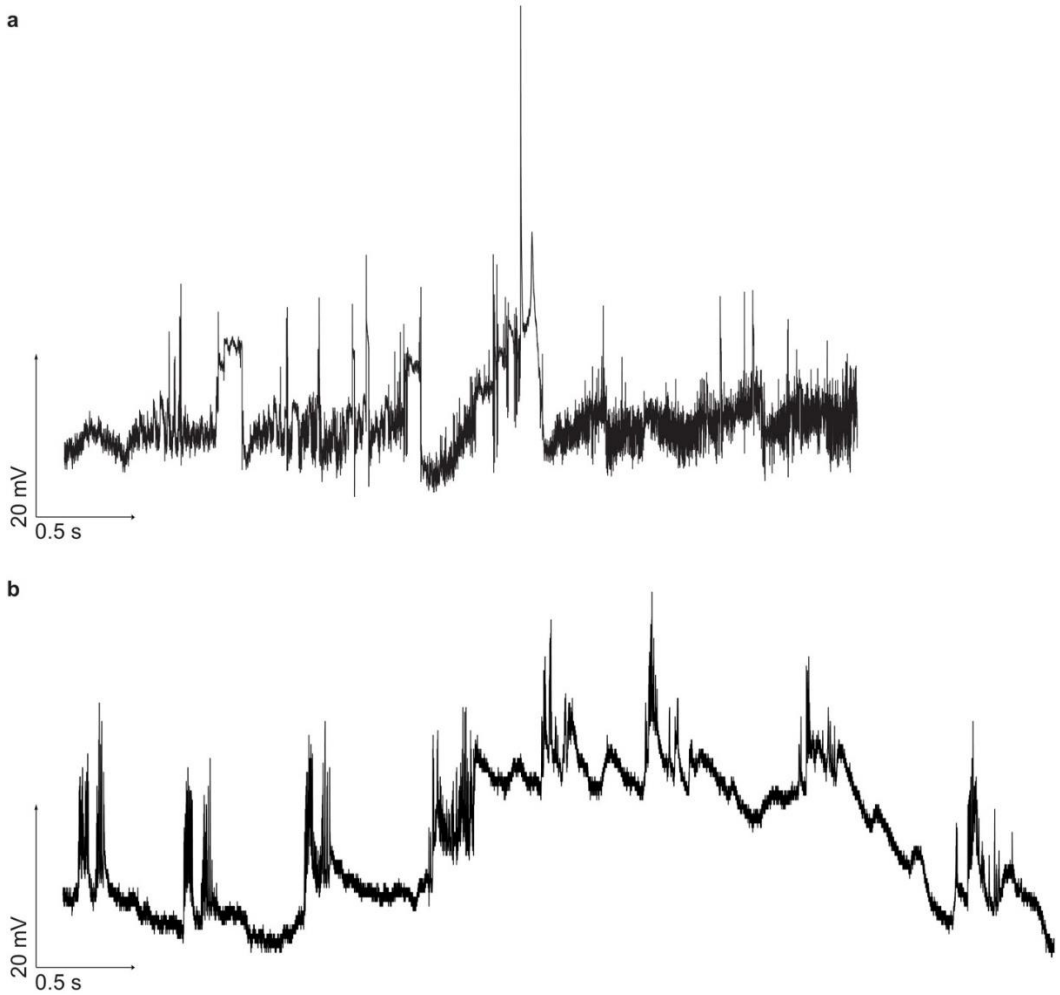

Figure 57. Recorded action potentials of adult mouse cardiomyocytes without phospholipids coatings.

a,**b**, Two sweeps of intracellular signal recordings on adult mouse cardiomyocytes without lipid functionalization on the FET surface, with (**a**) considerable noise or (**b**) fluctuating baselines during the recordings due to the unstable FET-cell membrane interfaces.

Without the phospholipid coating, the FET could still mechanically rupture the cellular membrane and access the cytoplasm sometimes. However, those recordings showed higher noise levels, lower signal amplitudes, and fluctuating signal baselines due to the highly unstable FET/cell interface (Figure 57).

Signals recorded without phospholipid gradually transformed from intracellular to extracellular, probably because the ruptured cell membranes fused again and expelled the FET[82] (Figure 58).

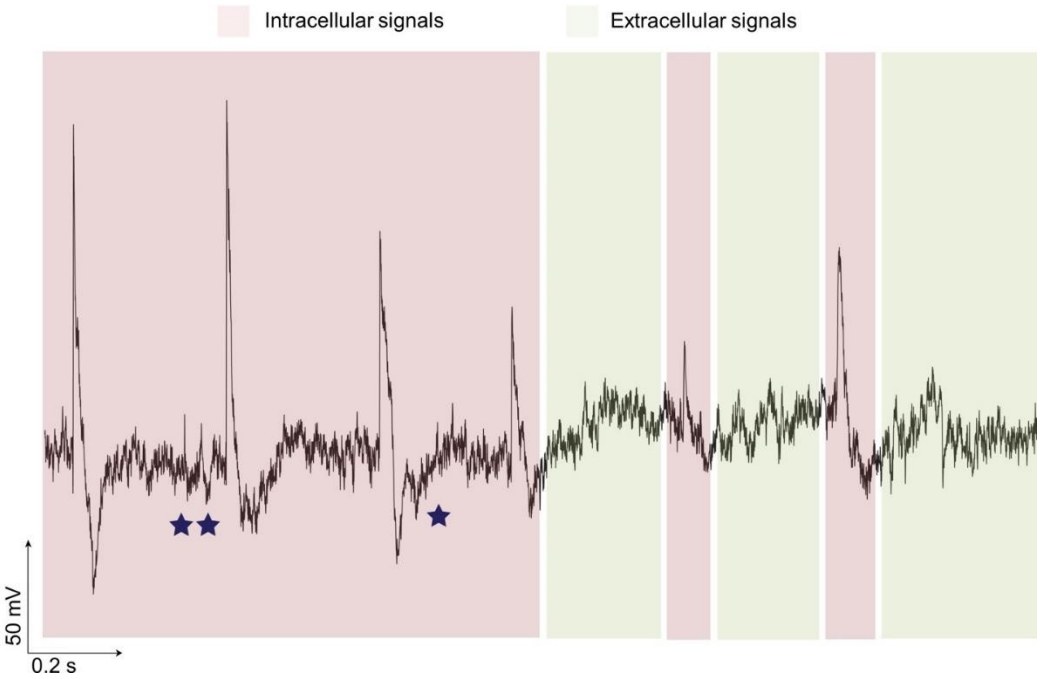

Figure 58. The process of transitioning from intracellular to extracellular recordings.
In this case, the intracellular recording of the HL-1 cell is achieved by mechanically rupturing the cell membrane. However, the sensor-cell interface is unstable. The cellular membrane will gradually fuse again and expel the FET. Thus, the signals sometimes show a transitioning process from intracellular (red shaded areas) to extracellular (light green shaded areas) recordings. Intracellular subthreshold events are recorded as marked by the stars. These low-amplitude signals cannot stimulate the all-or-none action potentials but can reflect the membrane potential oscillations due to ionic activities across the cellular membrane. For instance, these subthreshold potentials can influence sodium ion channels (i.e., the h gate) to open or close, generating a refractory period when the action potentials cannot be triggered[88].

When the FET is interfacing the outside of the cell membrane, it will record distorted signals, called extracellular signals, shown in Figure 59.

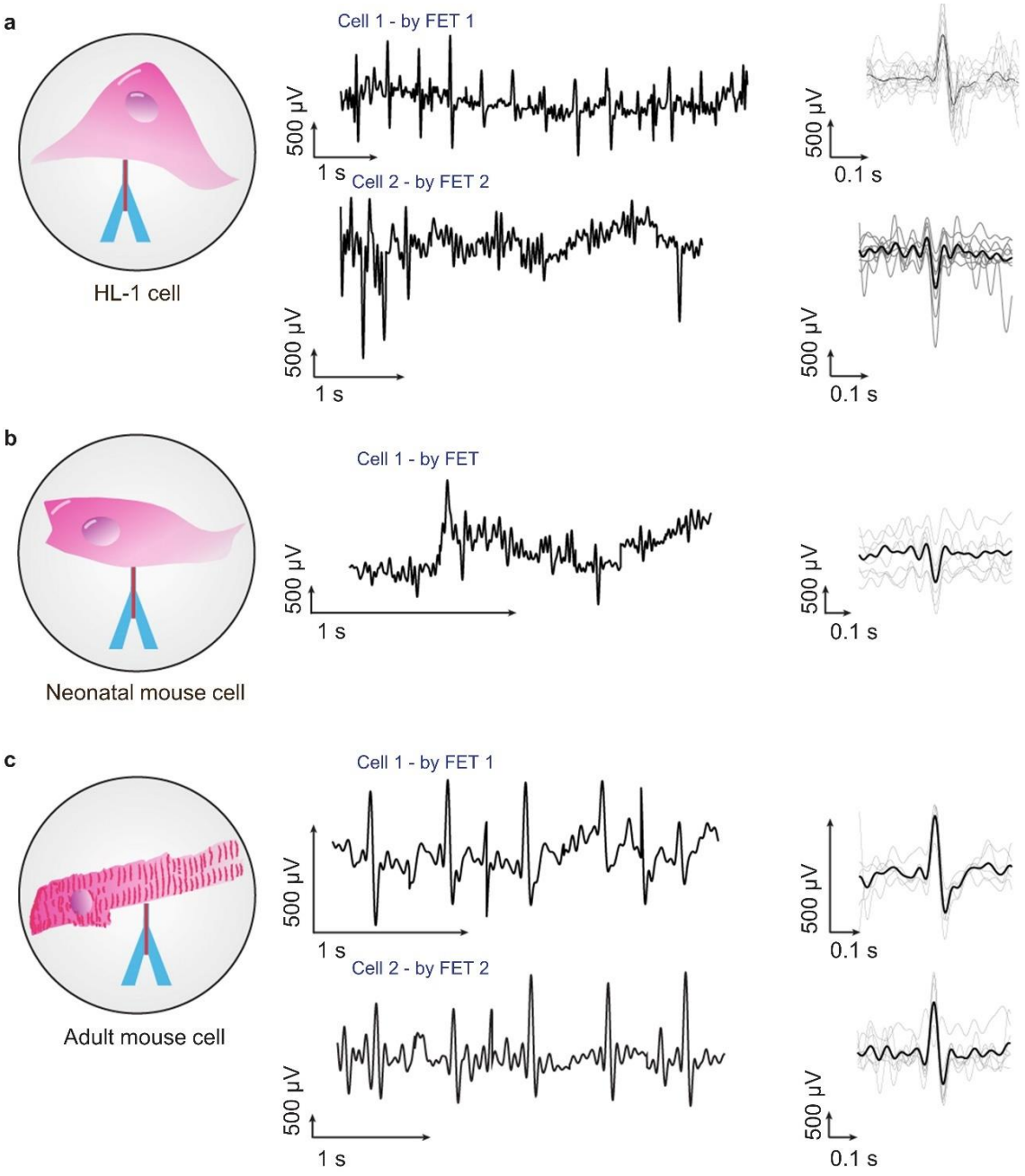

Figure 59. Extracellular field potentials of cardiomyocytes recorded by the FETs.
a–c, Before penetrating the cell membranes, with close contact, the FETs can record periodic spikes from (**a**) the HL-1 cells and (**b, c**) primary cells. These low-amplitude extracellular signals are characteristic extracellular field potentials of the cardiomyocytes[39,89].

We also verify these extracellular recordings by those recorded using the MEA device (Figure 60).

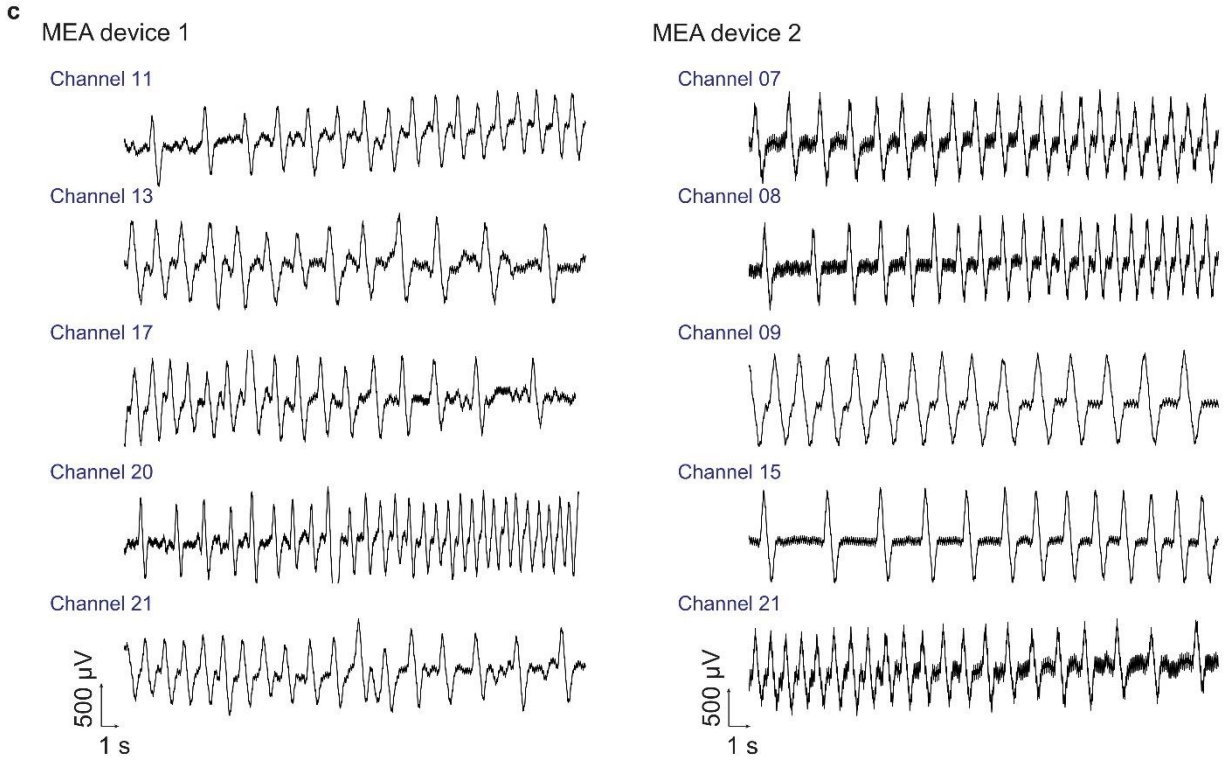

Figure 60. Extracellular field potentials of HL-1 cells recorded by the MEA.
A closeup optical microscope image showing the metal pads and the covered connection wires by a layer of insulating SU-8. Only the circular areas of the metal pads are exposed to contact the cells. Scale bar: 200 µm. c, Representative extracellular field potentials of the HL-1 cells from two MEAs. The signals have been processed by a bandpass filter (0.5–30 Hz) in MATLAB.

3.4 Pathological Studies of the HL-1 Cells.

We tested the FET performance by verifying the HL-1 cells' response to extracellular solution composition and ion channel blocking drugs.

Changing the ion concentrations in the extracellular medium would impact cellular electrophysiological characteristics. For instance, abnormal solutions with above normal potassium concentration (a.k.a. hyperkalemia) or below normal sodium concentration (a.k.a.

hyponatremia) in the culture medium can interfere with the proper electric signals. In this experiment, we prepared solutions containing doubled concentrations of potassium ions for hyperkalemia and half concentrations of sodium ions for hyponatremia studies.

Figure 61 shows the effect of hyperkalemia or hyponatremia on the recorded electrophysiological behaviors of cardiomyocytes, including the beating rhythm, resting membrane potential, and action potential duration. Abnormally high potassium or low sodium ion concentration would vary the cell's action potential shape by shortening the duration and decreasing the amplitude[90,91].

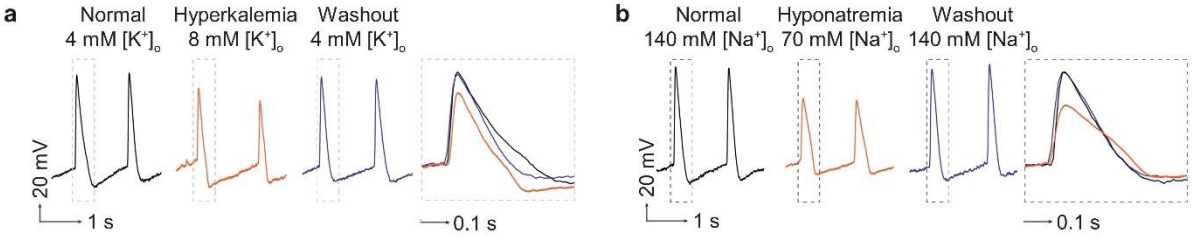

Figure 61. Pathological studies of the HL-1 cells by modulating ionic concentrations in the culture solutions.
Both (**a**) the hyperkalemia and (**b**) the hyponatremia cells exhibit a decreased signal amplitude, a shortened action potential duration (APD), and a longer refractory period compared to the normal cells, as recorded by the FET. The recorded action potentials recover when the culture solutions are switched back to the Tyrode's solution.

3.5 Effects of Ion Channel Blockers on Cellular electrophysiology.

Cellular electrophysiology can be modulated by drugs. These drugs act as ion channel blockers that can affect ionic influx and/or efflux across the cellular membrane so they can modulate cellular electrophysiology that can be reflected by the action potential morphology. In this work, the cells' responses to nifedipine or tetrodotoxin (TTX) were studied. Nifedipine is an

L-type calcium ion blocker and TTX is a sodium ion blocker. To prepare the drug solutions, we added nifedipine or TTX to the typical Tyrode's solution.

Figure 62 shows the measured responses of HL-1 cells to ion channel blockers with modulated action potential amplitude and duration. The results show that nifedipine or tetrodotoxin lowers the amplitude and reduces the action potential duration at 50% or 90% repolarization (APD50 or APD90). The effect is reversible after the extracellular solution was swapped back to normal compositions.

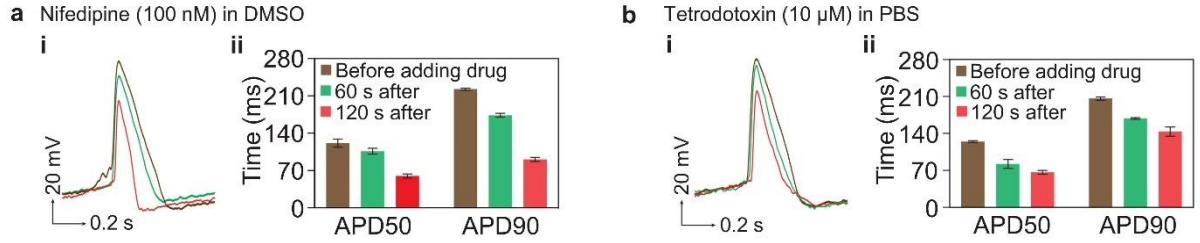

Figure 62. Effects of ion channel blocking drugs on (i) action potential morphologies of HL-1 cells recorded by the FET and (ii) corresponding quantitative analysis.
Cells exposed to (**a**) 100 nM nifedipine exhibit a lower spike amplitude and shorter APD50 or APD90 (action potential duration at 50% or 90% repolarization, respectively). The cells repolarize very fast because nifedipine is an L-type Ca^{2+} channel blocker, which diminishes the influx of Ca^{2+} into the cells. **b,** 10 μM tetrodotoxin acts on the rapid Na+ channels, reducing the spike amplitude and thus shortening the repolarization duration. Error bars are standard deviations of 20 recorded action potentials.

After the drugs or the abnormal solutions were administered to the cells, it took several minutes to affect the action potential recordings. Replacing the solutions with drugs or abnormal concentrations of ions back with the typical Tyrode's solution by perfusion would recover the cell's normal electrophysiological characteristics.

3.6 Conclusion.

In this chapter, we have summarized the approaches of recording a single cell's intracellular and extracellular electrophysiological signals using the FET array. In general, the electrical recordings maintain both the shape and amplitude of the action potentials of HL-1 cells and primary cardiomyocytes. These recordings have been validated by the gold standard patch-clamp. And the phospholipid coatings on the FET surface are critical to forming a stable sensor and cell membrane interface leading to faithful recordings by the FET array. Further, the cells' correspondence to abnormal external solutions or drugs were recorded using the FET array, which further shows the FET's excellent performance in sensing electrophysiological signals, providing promise for applications in drug screening.

Chapters Three, in full, is a partial reprint of the materials: 'Three-dimensional transistor arrays for intra- and inter-cellular recording, Yue Gu, Chunfeng Wang, Namheon Kim, Jingxin Zhang, Tsui Min Wang, Jennifer Stowe, Rohollah Nasiri, Jinfeng Li, Daibo Zhang, Albert Yang, Leo Huan-Hsuan Hsu, Xiaochuan Dai, Jing Mu, Zheyuan Liu, Muyang Lin, Weixin Li, Chonghe Wang, Hua Gong, Yimu Chen, Yusheng Lei, Hongjie Hu, Yang Li, Lin Zhang, Zhenlong Huang, Xingcai Zhang, Samad Ahadian, Pooja Banik, Liangfang Zhang, Xiaocheng Jiang, Peter J. Burke, Ali Khademhosseini, Andrew D. McCulloch, Sheng Xu, accepted in Nature Nanotechnology, 2021'. The dissertation author was the first author of this paper.

Chapter 4. Signal Propagation Behaviors in 2D Cell Cultures.

4.1 Simultaneous Recordings of Spontaneously Firing Cells.

Simultaneous recording intracellular signals from multiple cells is always a challenge for the patch-clamp and other nano-devices. Using the soft FET array, we can insert different FET sensors in different cells. We used a 3D 10-FET array with well-defined spacing (Figure 63) to record intercellular signal conductions, which is related to the electrical coupling states between cells[32].

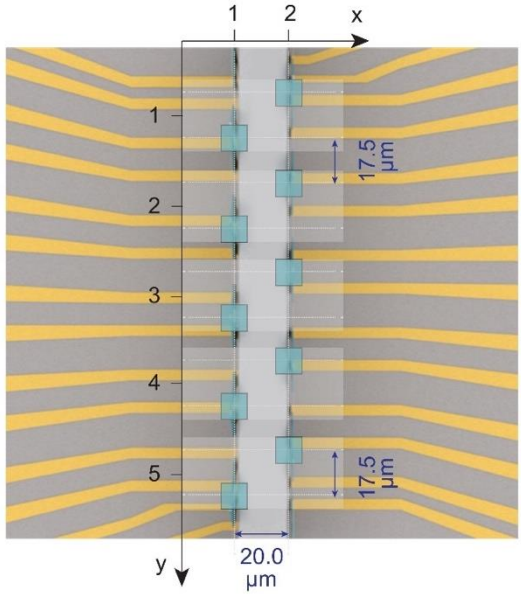

Figure 63. Intracellular recording on a 2D HL-1 cell culture by a 10-FET array.
Schematic top views of a 10-FET array. The spacing between each FET is accurately defined by lithography. A coordinate system is used to denote the position of each FET, as indicated by the green squares.

When a common electrical pulse is provided, the FETs exhibit the same characteristics, and the electrical signal delay between any two channels is no greater than 0.01 ms, suggesting that the system-induced electrical delay is negligible (Figure 50). A layer of spontaneously firing

HL-1 cells cultured on a PDMS sheet was laminated on the FET array. Attributed to the high sensitivity and low noise of the FET, each FET recorded intracellular signals, as shown in Figure 64.

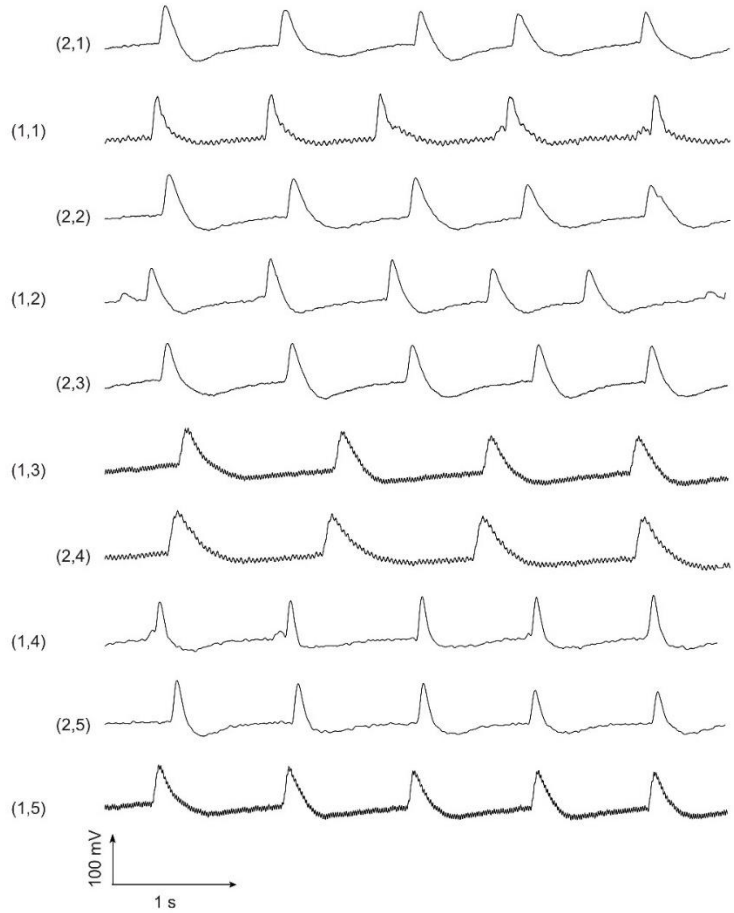

Figure 64. Recordings of spontaneous firing HL-1 cells by a 10-FET array.
Cells communicate on the basis of intercellular electrical coupling by gap junctions, particularly ion channels. Ions (e.g., K^+) can travel from one cell to its neighboring cells via these gap junctions, triggering the donor cells' action potentials. Without pacing the cells (e.g., by a platinum stimulation electrode), the FETs can also form stable FET-cell interfaces and record action potentials from different cells. However, the action potentials show arrhythmic firing patterns, which means the period of action potentials is varying. Also, the action potential's propagating behaviors become irregular because the locations and firing patterns of those spontaneously firing cells (i.e., pacemaker cells) in the culture are stochastic and inconsistent. Therefore, the signal conduction direction among these cells will alter according to the signals of the pacemaker cells.

4.2 Signal Propagation in Stimulated Cell Cultures.

We used electrical stimulation to regulate HL-1 cells' firing patterns to study the direction and velocity of intercellular signal conduction. Four electrodes were placed in the cell culture on the four corners, and a stimulation pulse was applied to one electrode in each measurement (Figure 65).

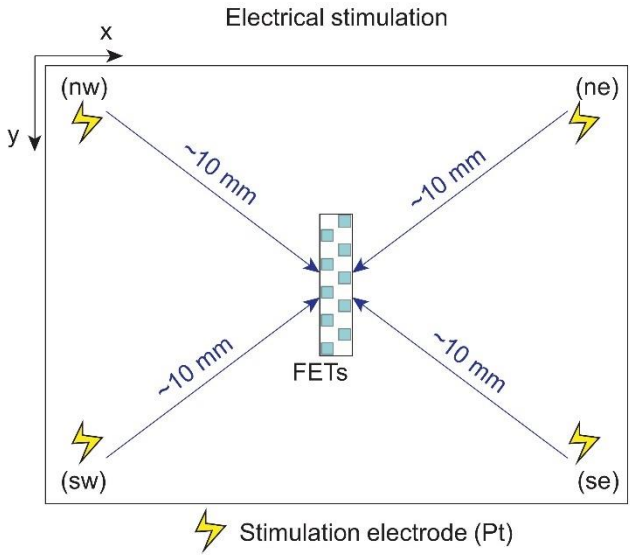

Figure 65. Cell stimulation configuration.
The schematic setup for stimulating the HL-1 cells, with four Pt electrodes placed in the cell culture on each corner. A stimulation pulse was applied to a single electrode in each measurement. We used biphasic pulses, so the net injection current was zero. The frequency, width, and amplitude of the pulses were 1 Hz, 1 ms, and 1 V, respectively, to effectively pace the cells.

Under electrical pacing, spontaneous arrhythmic action potentials are suppressed[85], and the corresponding recorded cellular signals are in Figure 66.

We calculate the signal latencies between the FETs by cross correlating the recorded action potential profiles (Figure 67).

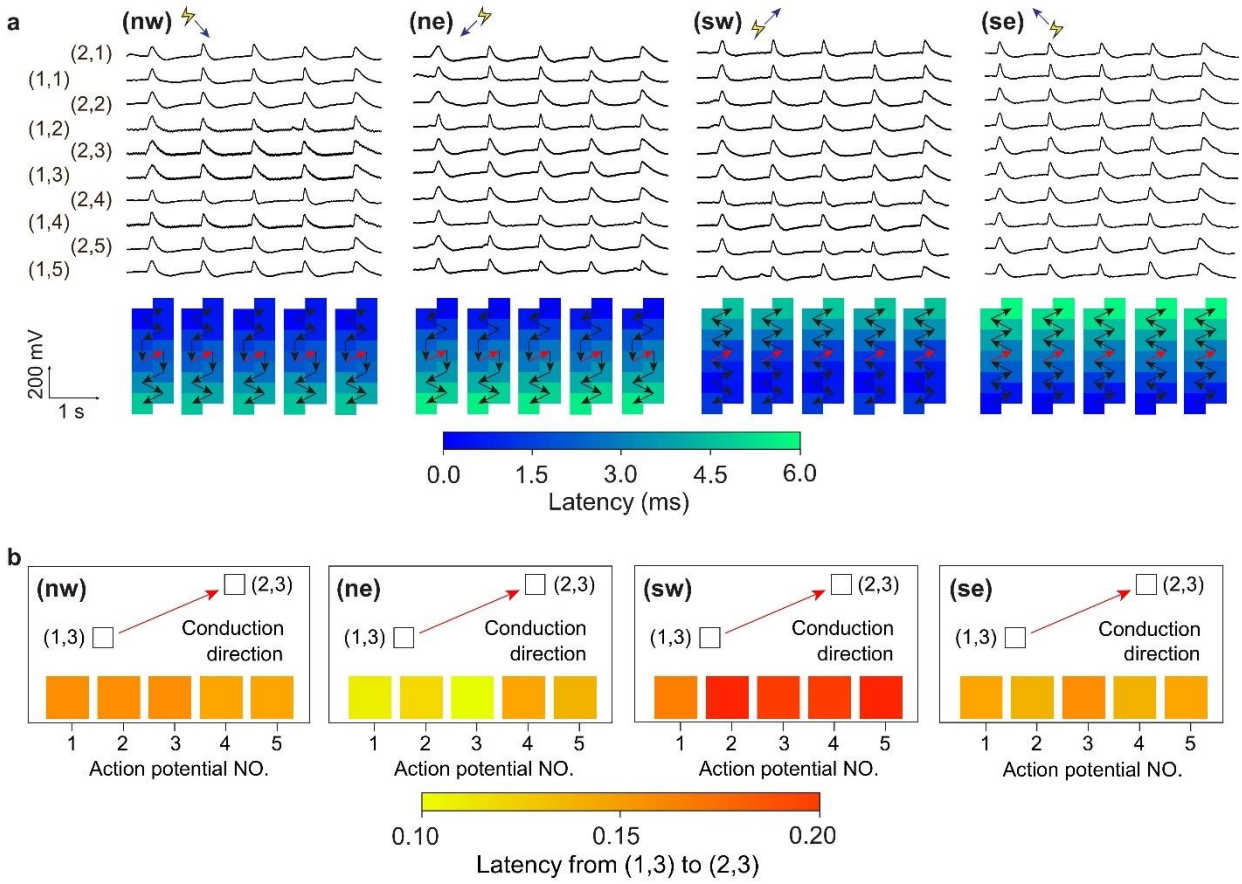

Figure 66. Recordings of HL-1 cells' action potentials by a 10-FET array under electrical stimulation.

a, Changing the stimulation electrode orientation from northwest (**nw**) to northeast (**ne**), southwest (**sw**), and southeast (**se**) will shift the directions of intercellular signal conductions. The first signal appeared in the FET that is relatively closer to the stimulation electrode and propagated among the cells per their coupling states, as indicated by the black arrows. The intercellular signal conduction velocity under electrical stimulation is from 35.1 to 39.3 $\mu m \cdot ms^{-1}$. The variations in the velocity are caused by the fluctuations of temperature, pH value, and ion concentration in the cell culture medium. In all scenarios, the directions of intracellular signal conductions, as indicated by the red arrows, are always the same, i.e., from (1,3) to (2,3). **b,** Schematics showing the latencies of intracellular signal conductions from (1,3) to (2,3).

Figure 67 introduces the cross-correlation method to calculate the latency between two action potential spikes. The computation was conducted in MATLAB using the cross-correlation function.

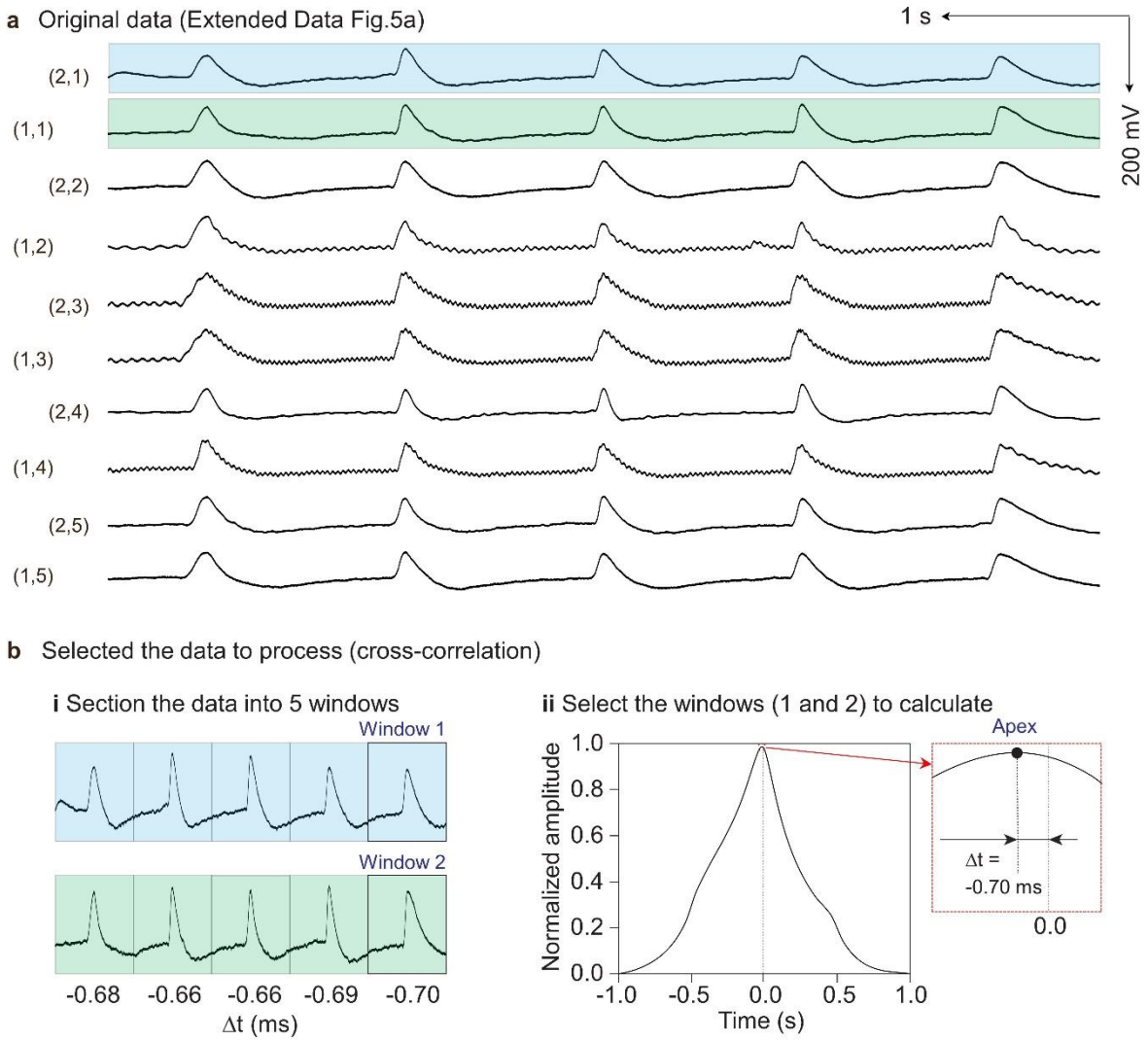

Figure 67. The cross-correlation method.

a, An example data set that is the same as those in Figure 66a. **b**, We select the signals of (2,1) and (1,1) and section the data into five windows. Each window is one-second-long and includes one action potential spike. We choose the fifth pair of windows to conduct the cross-correlation and use the action potential spike as the reference point. Cross-correlation calculated in MATLAB in the right plot shows a -0.70 ms latency (τ) from (1,1) to (2,1). By calculating the other four pairs of windows, we find the average latency from (1,1) to (2,1) is -0.68 ms. Similarly, latencies between any other two FETs can be accurately calculated, and the action potentials' propagating characteristics are faithfully revealed.

To calculate the latency between any two action potentials, we first chose the simultaneous recordings from different FET sensors, such as (2,1) and (1,1) in Figure 66. We selected a fixed

duration of data that contained an action potential recorded by (2,1) and (1,1). The latency between these two data sections was calculated by the cross-correlation method.

A heat map visualizes the action potential conduction direction among the cells, as indicated by the arrows. Based on the conduction latencies and the predefined distances between the FETs, the intercellular signal conduction velocity is calculated to be 35.1~39.3 μm·ms^{-1}, comparable with the results from other studies on HL-1 cells[89] (Figure 68). Long-period recordings show the robustness of the measurements by the FET array (Figure 69).

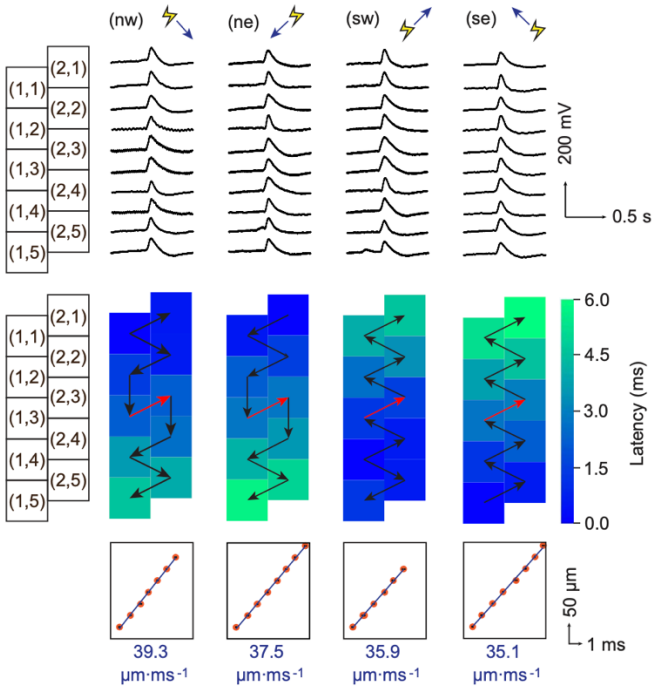

Figure 68. Calculation of conduction velocity between cells.
Simultaneous intracellular recordings from a 2D HL-1 cell culture under electrical pacing at different orientations to the FETs. All FETs recorded periodic intracellular action potentials of 95~116 mV. Heat maps illustrate the latency of action potentials among the cells. Arrows indicate the possible signal conduction paths among cells, where the black arrows mean intercellular and the red arrows mean intracellular signal conductions. In all measurements, the signal first arrives at the cell closest to the stimulation electrode and then transmits subsequentially to the neighboring cells. The average intercellular conduction velocity is 35.1~39.3 μm·ms^{-1}. Regardless of the stimulation orientation to the FETs, the intracellular signal conduction is always from (1,3) to (2,3).

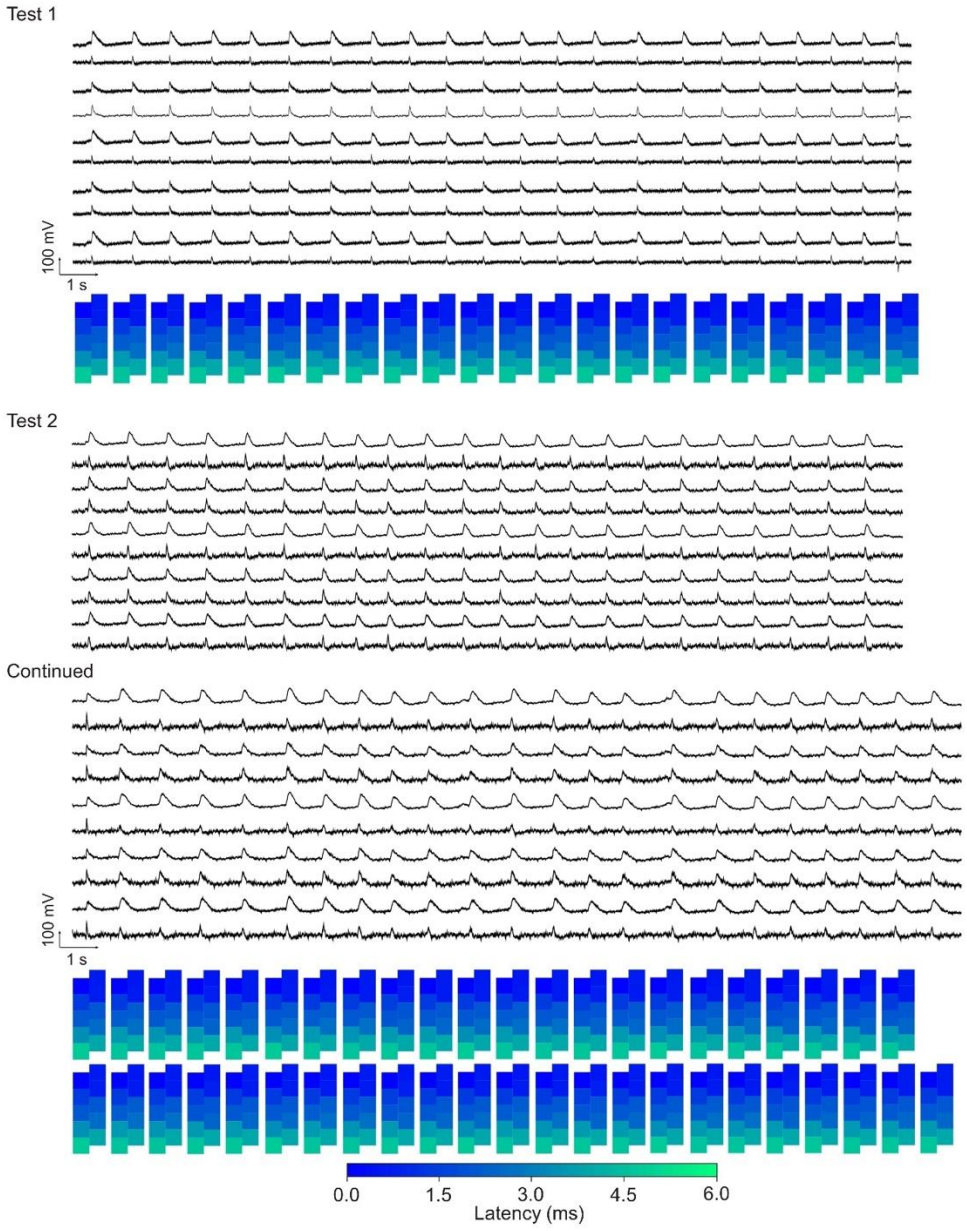

Figure 69. Long-period recordings of intracellular signals of paced HL-1 cells by the 10-FET array.

The stimulation electrode is ~10 mm to the northwest corner of the FET array. Heatmaps elucidate the action potentials' latencies and the occurrence sequence among the cells. Signals of tests 1 and 2 show continuous recordings for 25 and 50 seconds, respectively, which is the longest among all arrayed FET-based intracellular probes in the literature. The extended intracellular recordings prove the stable performance of each one of the FETs in the array.

4.3 Signal Conduction inside One Cell.

Intracellular signal conduction in cardiomyocytes corresponds to various forms of subcellular ionic activities[92]. However, it is challenging to record intracellular conductions in cardiomyocytes because it is difficult to interface two or more patch clamps with one cardiomyocyte[93]. Also, the short signal latency inside the cardiomyocyte can be overshadowed by the intrinsic delay of the existing recording systems[94].

In Figure 68, regardless of the orientation of the stimulation electrode, we found the latencies between the FETs at (2,3) and (1,3) to be always ranging from 0.10 ms to 0.20 ms, much shorter than those between the other FETs. Given the distance between these two FETs (26.6 μm), the conduction velocity is calculated to be 182 μm·ms^{-1}, which is about five times the intercellular conduction velocity (Figure 70).

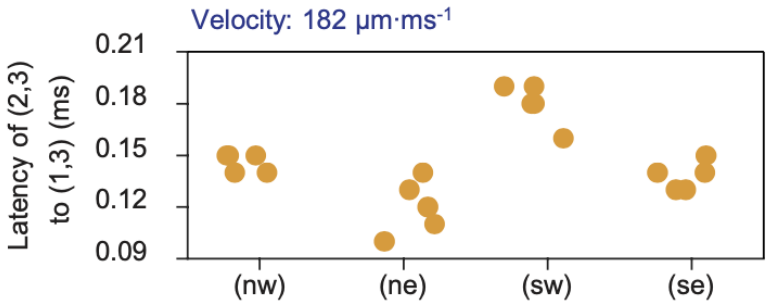

Figure 70. Calculation of intracellular signal conduction velocity.
The average and standard deviation of the latencies between (1,3) and (2,3) calculated from the 20 action potentials in four orientations being 0.146 ± 0.025 ms. The intracellular conduction velocity is 182 μm·ms^{-1}, which is about five times the velocity of intercellular conduction.

To verify the measurement, we used the same 10-FET array to study a different HL-1 cell culture. This time, we found no signal conduction between the FETs at (2,3) and (1,3); but two other FETs, at (1,1) and (1,2), showed a ~0.18 ms latency (Figure 71).

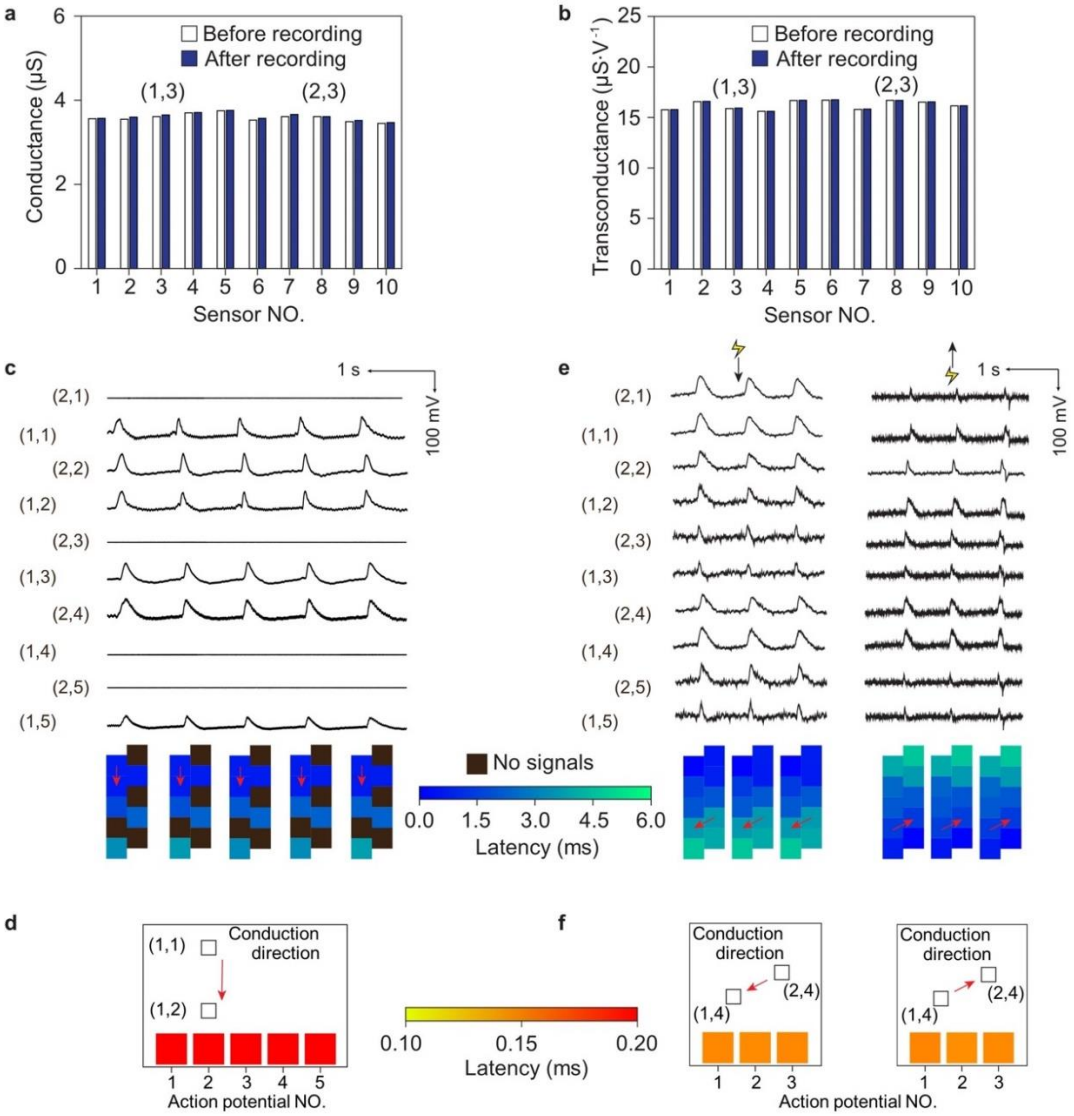

Figure 71. Justification of the intracellular signal conduction inside a HL-1 cell.
a,**b**, Comparable conductance and transconductances of the 10-FET array measured before and after intracellular recordings, showing that the FETs maintain their intact electrical properties and are free from any crosstalk or short circuits between the FETs. The same FET array is used for the recordings in Figure 66. **c**,**d**, With the same electrical stimulation **(nw)**, another recording by the same FET array on a different HL-1 cell culture showing a ~0.18 ms latency between FETs (1,1) and (1,2), which are 35 μm apart. The intracellular signal conduction velocity is ~194 $\mu m \cdot ms^{-1}$ that is close to the measurements (~182 $\mu m \cdot ms^{-1}$) in Figure 70. Such reproducible and reliable results provide additional evidence for the intracellular signal conductions. **e**,**f**, Studying the relationship between intracellular and intercellular signal conduction directions on another recording on HL-1 cell culture. In this case, the intracellular conduction direction from (2,4) to (1,4) varies with the intercellular direction when the stimulation orientation is changed from the north to the south of the FETs. The intracellular signal conduction velocity is ~191 $\mu m \cdot ms^{-1}$, which is on par with the results in other measurements.

To triple check the measurement results, we used confocal microscopy to image live cells while simultaneously recording electrical signals. The results verified that two FETs were in the same cell (Figures 72 and 73). Therefore, the signals we measured between these two FETs indicate intracellular conductions.

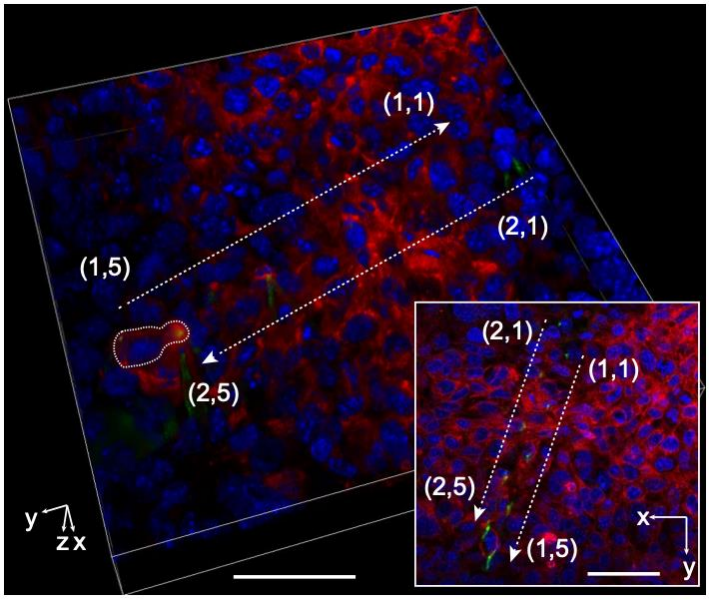

Figure 72. Imaging the cells during electrical recording.
Confocal microscopy images illustrating a 3D view of FETs intracellularly interfacing live HL-1 cells. Inset is the corresponding top view. Green (Rhodamine 6G): the polyimide in the FETs; Red (CellBrite): cell membranes; Blue (NucBlue): cell nuclei. The images clearly show two FETs, (1,5) and (2,5), are interfacing the same cell. Scale bars: 50 μm.

We conducted fluorescence staining and confocal microscopy imaging to show the cell/FET interfaces. In this work, live-cell staining was performed using NucBlue (ThermoFisher Scientific) and CellBrite (Red; Biotium). The HL-1 cells were incubated at 37 °C for 15 minutes and 20 minutes after adding CellBrite and NucBlue dyes, respectively. To visualize the FET device, we mixed 0.1 mg·ml-1 rhodamine 6G dye (Sigma Aldrich) in the PI layer during the device fabrication. The device would emit green fluorescence, as shown in Figures. 72 and 73.

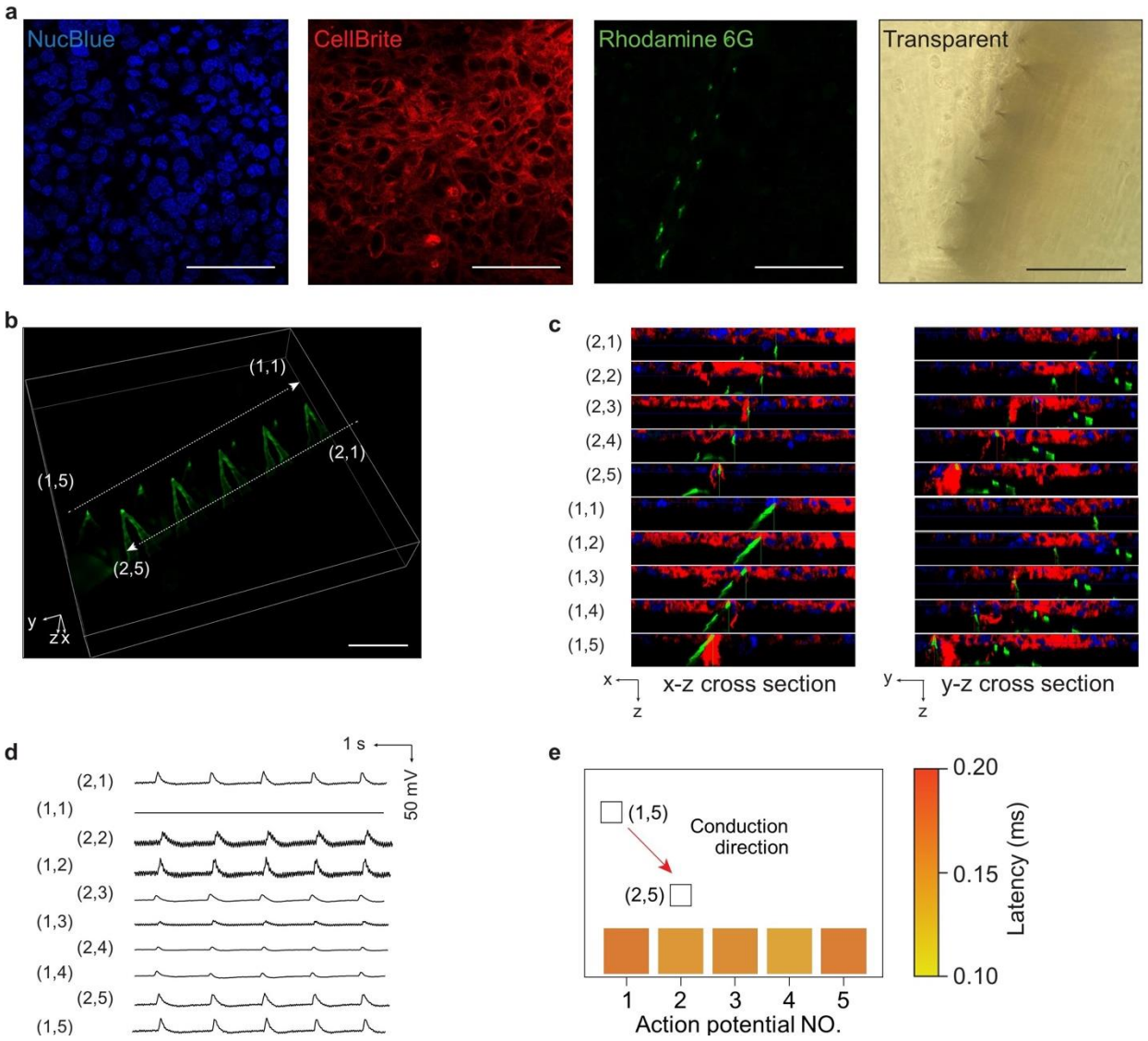

Figure 73. Fluorescent images and simultaneous action electrical recordings of an FET array and HL-1 cells.

a, Fluorescent images of nuclei (NucBlue), cell membranes (CellBrite), and FETs (Rhodamine 6G), as well as a bright field optical image, illustrating features of the cells and FETs. Scale bars: 100 µm. **b**, A 3D view image corresponding to the images in Figure 72, showing the FETs structures and relative spatial locations. Scale bar: 50 µm. **c**, Cross-sectional images of each FET in the x-z and y-z planes, showing well-defined interfaces between the cells and FETs. **d**,**e**, Simultaneous electrical recordings performed with the fluorescent confocal imaging. The intracellular conduction direction is from (1,5) to (2,5). The intracellular signal conduction velocity is ~184 $\mu m \cdot ms^{-1}$.

Confocal imaging was carried out using a Leica SP8 confocal microscope with lightning deconvolution. Confocal images were acquired using 405, 647, and 488 nm to excite components labeled with NucBlue, CellBrite, and Rhodamine 6G fluorescent dyes, respectively. Fiji (ver. 2.1.0/1.53c) was used for analyzing the confocal images.

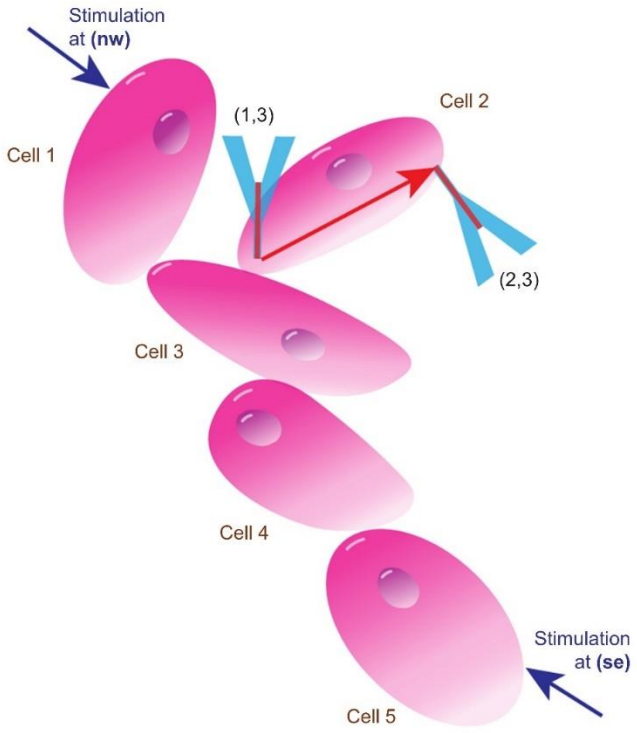

Figure 74. A simplified model illustrating the independence of inter- and intra-cellular signal conduction directions.
Five cells are electrically coupled with each other at the contacted areas. Two FETs record intracellular signals simultaneously from Cell 2. Particularly, Cell 2 is only electrically coupled with Cell 3. When the stimulation is placed at the northwest **(nw)** orientation to the FETs, the intercellular signal propagates from Cell 1 and travels to Cell 3 and Cell 2. The intracellular conduction direction is from (1,3) to (2,3), because (1,3) is closer than (2,3) to the electrical coupling position between Cell 2 and Cell 3. When the stimulation is placed at the southeast **(se)** corner, the intercellular signal propagates from Cell 5 to Cell 4, Cell 3, and then Cell 2. Similarly, the intracellular signal conduction is still from (1,3) to (2,3) due to the same reason. In other words, the incoming signal from the upstream cell always first arrives at a location closer to (1,3) than (2,3), leading to an invariant intracellular signal conduction direction regardless of the intercellular signal conduction directions. In this case, the intracellular signal conduction direction is dependent on cells' coupling positions and FETs' sensing locations on the cell membranes.

The slight fluctuation in the intracellular conduction velocity maybe because of the constantly changing ionic distributions within the cell. The intracellular conduction is much faster than intercellular conduction because the latter is slowed down by ion diffusion processes via gap junctions between neighboring cells[95].

Additionally, in Figure 68, when the stimulation originated from different orientations relative to the FETs, the corresponding intercellular signal conduction direction would change. However, we found that the intracellular conduction direction was always from (1,3) to (2,3) in this case, independent of the directions of intercellular conduction, which was probably related to the positions of the FETs and cells' coupling with the neighboring cells (Figure 74).

4.4 Conclusion

In this chapter, we have demonstrated the results of using ten FET sensors to record multiple cells simultaneously. Each high-sensitivity FET sensor can pick up an intracellular action potential from each cell. The calculated conduction velocity between cells is ranging from 35.1~39.3 $\mu m \cdot ms^{-1}$. Intracellular signal conduction is also recorded, for the first time, and the velocity was calculated to be ~182 $\mu m \cdot ms^{-1}$. Using the confocal microscopy while recording the intracellular signal propagation validates the intracellular recording with two FET sensors. We discover that the intracellular signal propagation direction is related to the electrical coupling states between cells.

Chapters Four, in full, is a partial reprint of the materials: 'Three-dimensional transistor arrays for intra- and inter-cellular recording, Yue Gu, Chunfeng Wang, Namheon Kim, Jingxin

Zhang, Tsui Min Wang, Jennifer Stowe, Rohollah Nasiri, Jinfeng Li, Daibo Zhang, Albert Yang, Leo Huan-Hsuan Hsu, Xiaochuan Dai, Jing Mu, Zheyuan Liu, Muyang Lin, Weixin Li, Chonghe Wang, Hua Gong, Yimu Chen, Yusheng Lei, Hongjie Hu, Yang Li, Lin Zhang, Zhenlong Huang, Xingcai Zhang, Samad Ahadian, Pooja Banik, Liangfang Zhang, Xiaocheng Jiang, Peter J. Burke, Ali Khademhosseini, Andrew D. McCulloch, Sheng Xu, accepted in Nature Nanotechnology, 2021'. The dissertation author was the first author of this paper.

Chapter 5. Signal Propagation Behaviors in 3D Cell Cultures.

5.1 Engineering of 3D Cardiac Tissues.

Compared with 2D cellular cultures, 3D engineered tissue constructs better resemble natural organs in structural complexity and physiological functions. Therefore, they are excellent models for intracellular electrophysiology studies[96].

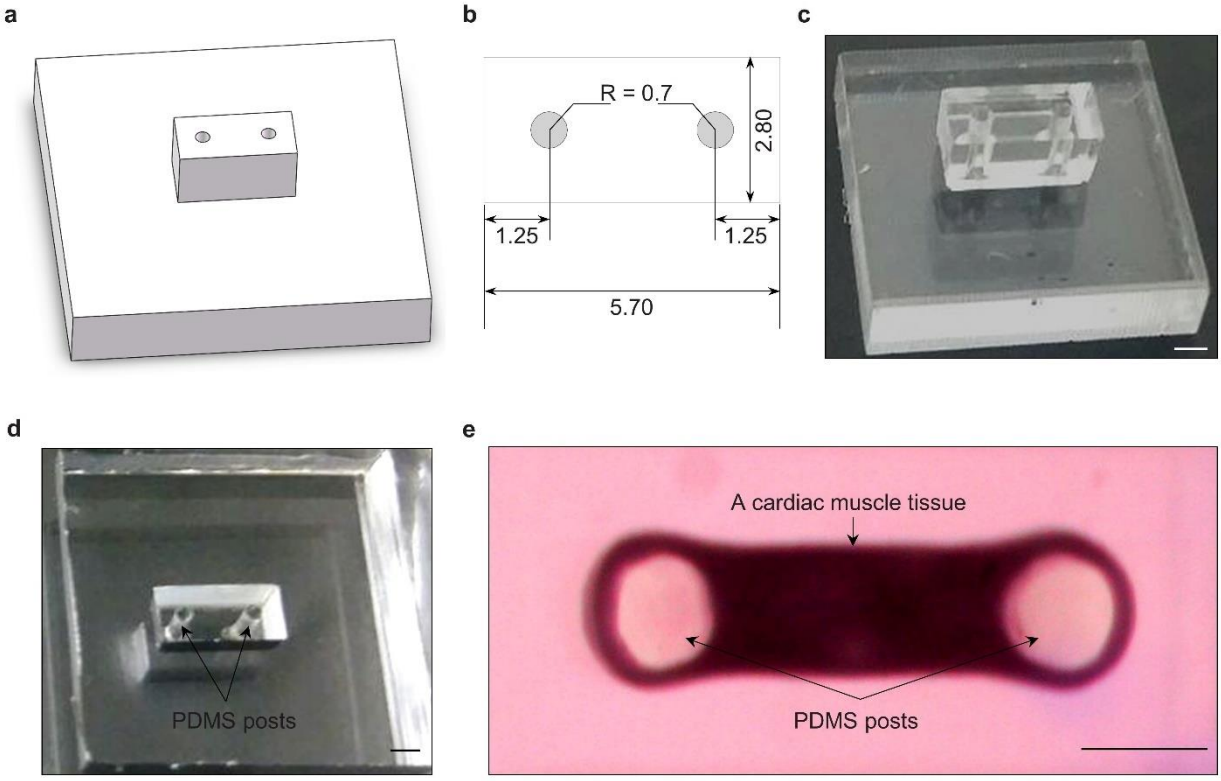

Figure 75. Fabrication processes of the PDMS platform for cultivating cardiac microtissues. **a,** Schematics of the master mold. **b,** The top view of the well and micro-posts. Unit: mm. **c,** The PMMA master mold made by laser ablation. **d,** The PDMS well and two micro-posts made by the PMMA master mold. **e,** A cardiac microtissue around micro-posts and inside the well. All scale bars are 1 mm.

3D microtissues exhibit large similarity to the native tissue in the natural state[97], providing value for studying organ development, disease progression, and effectiveness of certain drugs.

Therefore, it is attracting more attention as the biological model for pathology and pharmaceutical studies of cardiovascular diseases.

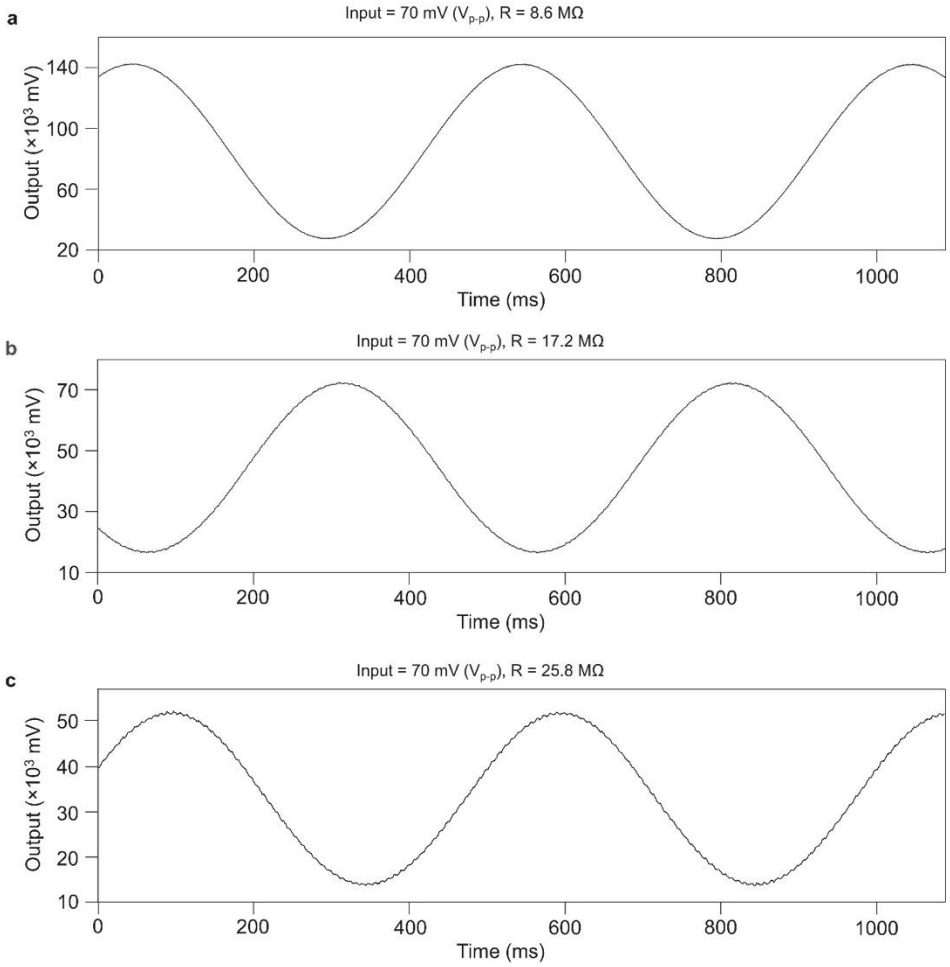

Figure 76. Amplification tests of the DDC264.

a-c, The DDC264 is a current input analog-to-digital converter. To calculate its amplification, a signal (sine wave, $V_{p-p} = 70$ mV) is input into a channel on the DDC264 board and goes through various resistances. The output signal is recorded accordingly, when the resistance is (**a**) 8.6 MΩ, (**b**) 17.2 MΩ, and (**c**) 25.8 MΩ, respectively. The input current is the division of V_{p-p} by the resistance, which is 8.14, 4.07, and 2.71 nA in (**a**), (**b**), and (**c**), and the output voltage reading is correspondingly 111,941, 563,12, and 37,495 mV, respectively. Thus, the amplification of the DDC264 is 13.81 $V \cdot nA^{-1}$, which is used to calculate the FET's current in the conduction channel, and further to derive the membrane potentials during cellular recordings.

The PDMS platform consisted of two or more micro-posts and one well to construct the microtissues was fabricated. A master mold was designed using AutoCAD (Autodesk Inc., USA)

and made of PMMA using laser ablation (Figure 75). Sticking the PMMA to the Petri dish formed a mold for curing PDMS (Dow Corning, Sylgard™ 184, USA, base:curing agent ratio 20:1, heated at 80 °C for 2 hours).

After proper sterilization, the fabricated PDMS platform (within the well and around the microposts) was filled with a collagen-based hydrogel with a density of 3 $mg \cdot ml^{-1}$. The cell culture media was a mixture of Dulbecco's Modified Eagle Medium (DMEM) (Gibco, USA), 10% fetal bovine serum (Gibco, USA), and 1% penicillin-streptomycin (Lonza, USA). Cells were incubated at 37 °C with 5% CO_2.

Measurements were conducted three days after cell seeding in the PDMS platform and forming the tissue compaction (Figure 75e). Figure 51 shows the measurement setup of the 128-FET array, which included a customized DAQ system based on a commercial current input analog-to-digital converter (TI DDC264). Each channel could operate independently with no crosstalk. The system had a fixed amplification of 13.81 $V \cdot nA^{-1}$ (Figure 76).

5.2 Design of a 128-FET Device with Sensors Located on Three Different Heights

Existing devices have limitations in interfacing with 3D tissues; either they can only do extracellular sensing[98], or they have a uniform height for interrogating cells on a common plane only[12,82]. With tunable heights, the 3D FET array provides a unique opportunity to study the electrophysiology of 3D tissues. To this end, we fabricated a stretchable 128-FET array distributed in 40 units of three different heights, capable of interrogating cells at three different depths in a 3D microtissue (Figure 77).

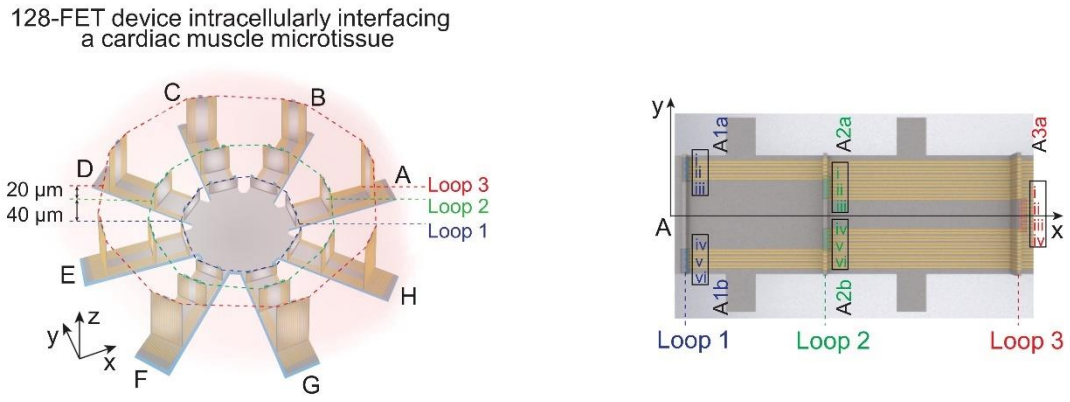

Figure 77. Schematic of a 128-FET array.
Schematic diagrams of the 128-FET array distributed on eight arms. On each arm, there are 16 FETs in five units of different heights, distributed on three concentric loops (left panel). The 16 FETs' relative positions and assigned coordinates are labeled (right panel).

To clearly display each FET's recordings of the 128-FET array, we arrange the data in a pixelized layout, shown in Figures. 78. We can stack the rasterized plot and make a video to show the dynamic change of each FET's properties (Figure 79).

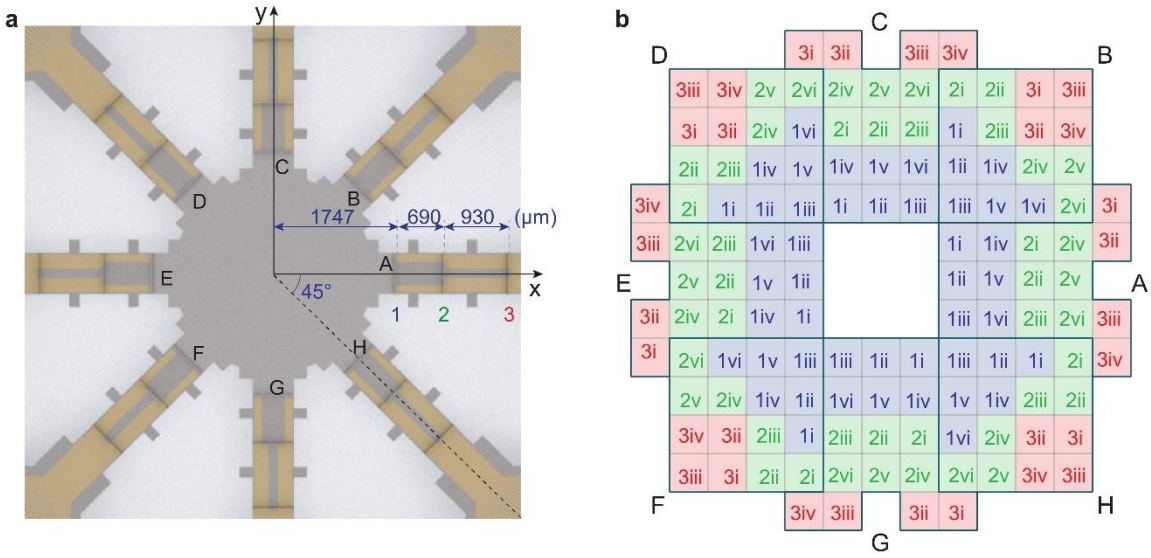

Figure 78. Organization of the 128-FET array and display of data.
a, Schematic distribution of the 128-FET array in eight arms of different directions, labeled counterclockwise from A to H. In each arm, the FETs have different heights distributed in three loops, labeled as 1, 2, and 3. **b,** A raster plot with coordinates of each FET in the array.

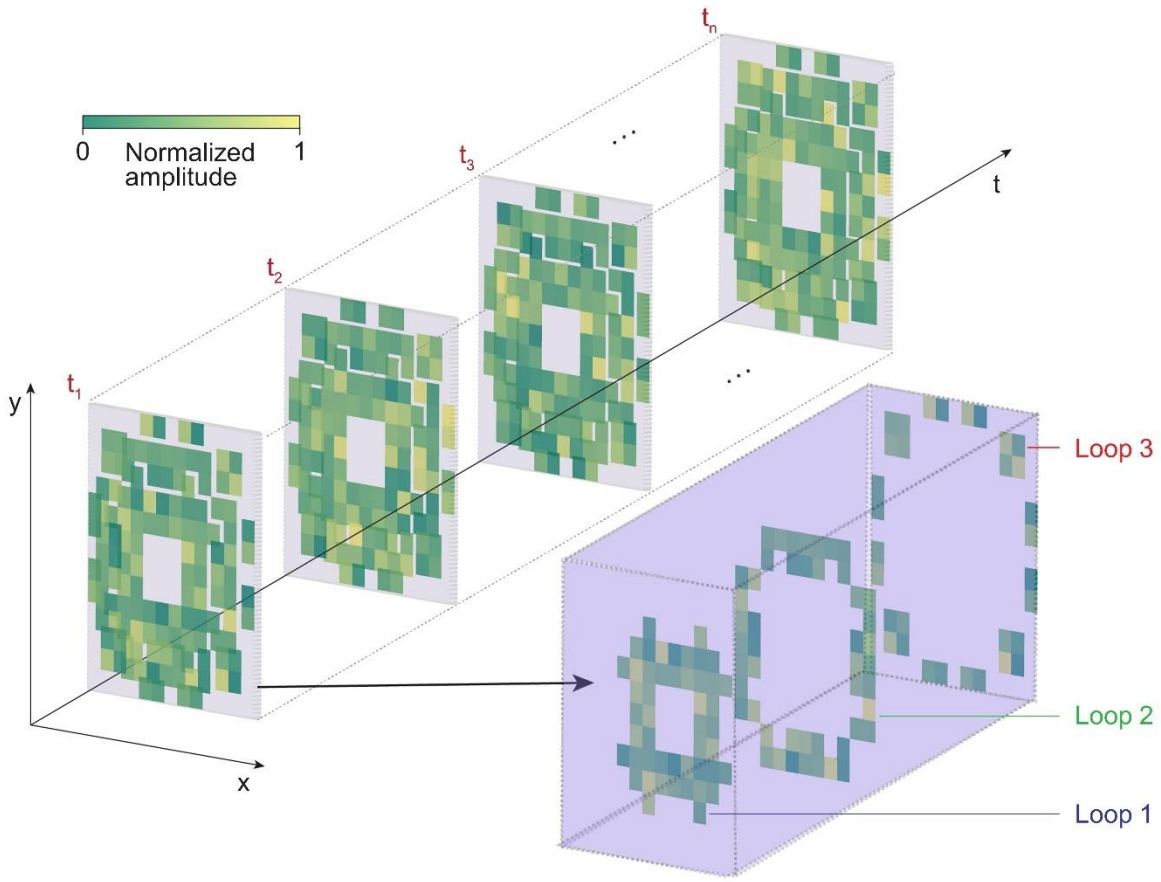

Figure 79. Visualization of the rasterized plot in heatmap.
Heatmaps with the raster layout showing the normalized amplitude of each FET at specific time points, e.g., t_1, t_2, etc. The transient information of each FET's recordings could be animated by stacking many heatmaps of sequential time points.

5.3 Electrical Characterization of the 128-FET Device.

Before we used the FET device to record electrophysiological signals of the microtissue, we characterized the output and transfer properties of each FET in the array, shown in Figure 80. The FETs have very similar conductance and transconductance, proving that the fabrication process is reliable and optimized.

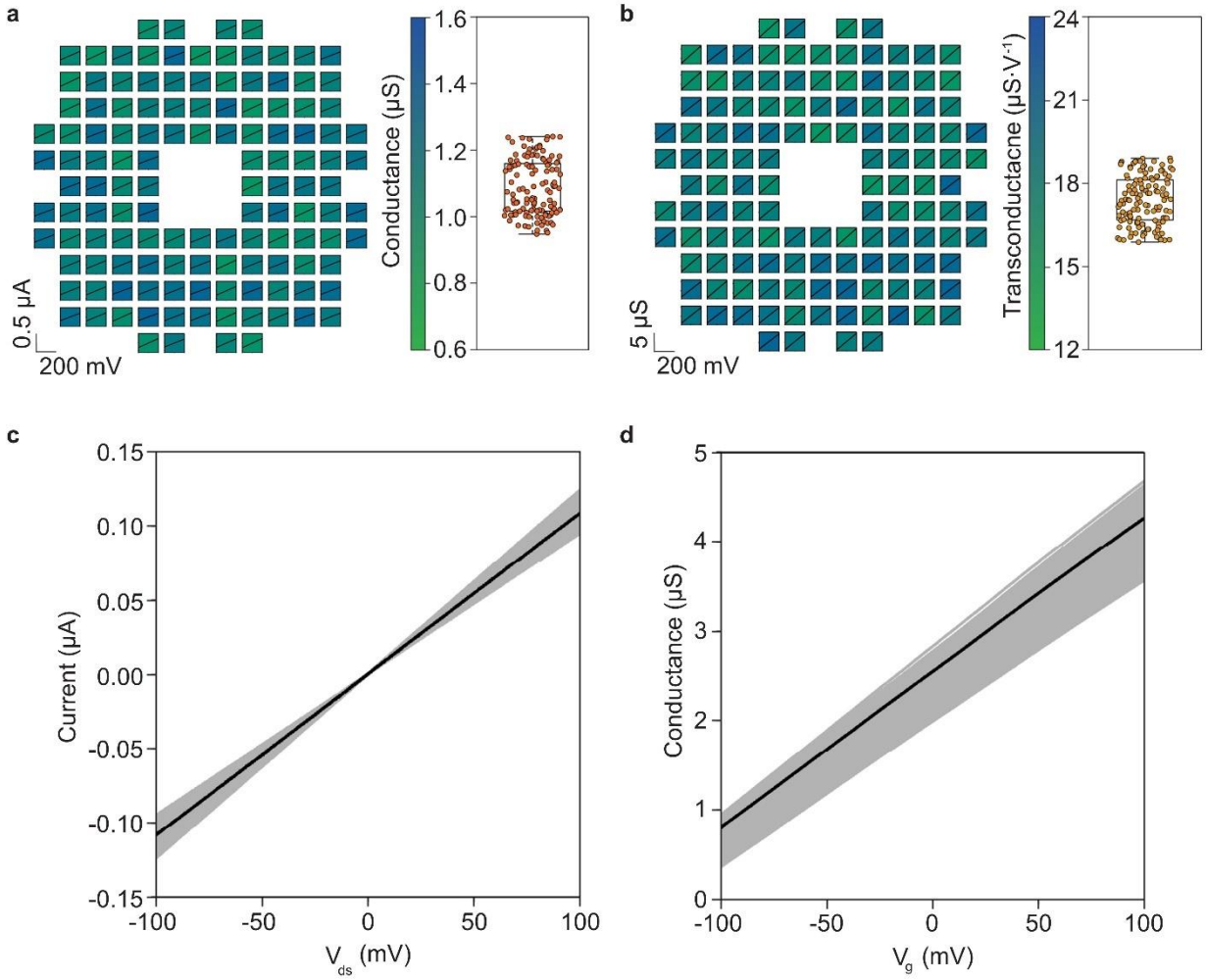

Figure 80. Electrical characterizations of the 128-FET array.

a, Output characteristics of each FET in the array. The measurement is performed with PBS solution (pH: 7.4 at 37 °C) covering the gate regions of all FETs and under a fixed 0 mV potential in the solution by an Ag/AgCl electrode. The background color of each pixel of the raster plot represents the conductance, in accordance with the color bar on the right. A box and whisker plot on the right summarizing each sensor's conductance. The 128 FETs have an average conductance of 1.1 µS. **b,** Transfer characteristics of each FET in the array. The measurement is performed in the same configuration as the water-gate characterization. A 100-mV potential is applied to the source, and the signal is collected at the drain of each FET. The background color of each pixel of the raster plot represents the transconductance, in accordance with the color bar on the right. A box and whisker plot on the right summarizing each sensor's transconductance. The 128 FETs have an average transconductance of 17 $\mu S \cdot V^{-1}$. **c,d,** Summary of all 128 FETs' output and transfer characteristics in gray lines, and the average is shown by the black lines. Both the conductance and transconductance have great consistency among all of the 128 FETs, because of the high reliability of the fabrication process. Each FET has high sensitivity for 3D tissue mapping.

5.4 Electrophysiology Recording on Cardiac Tissues.

We use the 128-FET device to measure an engineered cardiac microtissue. The tissue was Neonatal rat cardiomyocyte tissues were engineered on a PDMS platform composed of a well and two microposts using the methods previously reported[99]. Cardiomyocytes were mixed with the collagen-based gel at a density of ~50 M cells·ml^{-1}. Each cell-laden hydrogel was filled inside the PDMS well around two micro-posts and incubated for 1 hour. Then, culture media was added to the cell-laden gels, followed by incubation.

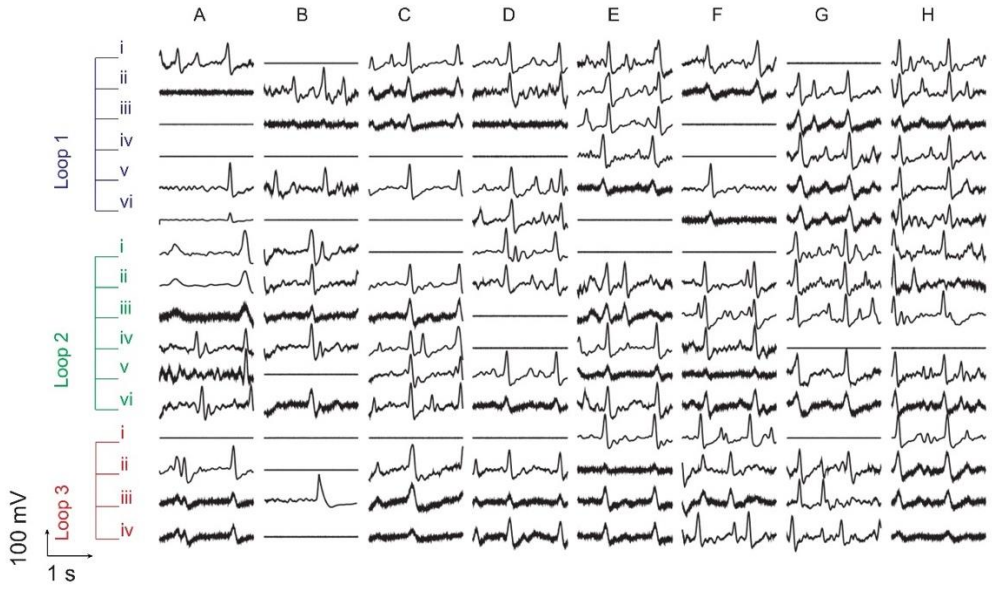

Figure 81. A representative dataset of recordings by the 128-FET array.
Representative recordings from the 3D cardiac tissue by the 128-FET array. Intracellular action potentials are recorded from all three loops on each arm.

Representative recordings by the array show intracellular action potentials in a 3D cardiac tissue, with 44% of the FETs being intracellular, 34% extracellular, and 22% inactive, where the intra- or extra-cellular signals were defined by the shape and amplitude of the signals[100] (Figures. 81 and 82).

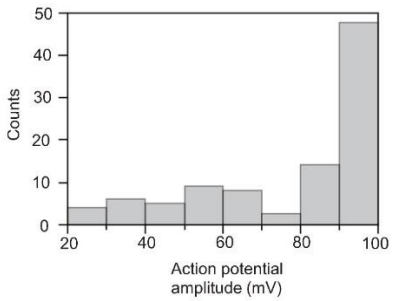

Figure 82. A histogram of spike amplitudes.
Statistical analysis of the recordings shown in Figure 81 shows over 40% FETs recorded high-amplitude intracellular signals.

The inactive FETs could be due to electrically inactive cells, or degraded performance of the FET, or nonideal FET-cell coupling (e.g., because of elastic response from the cytoskeleton).

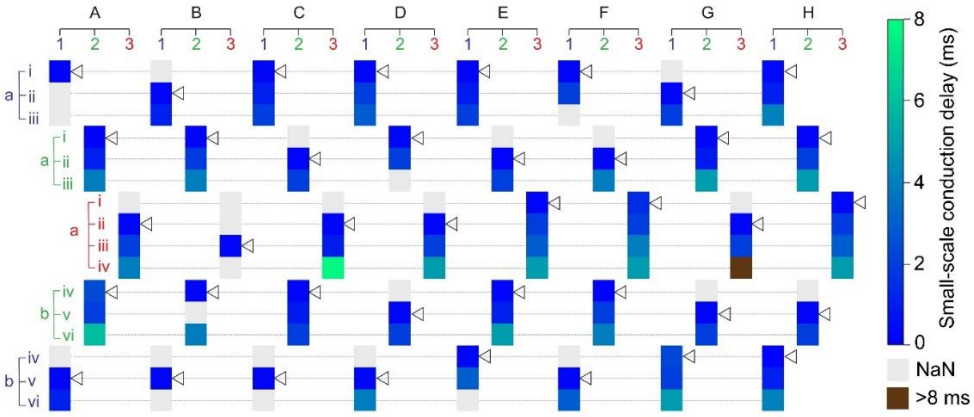

Figure 83. Small-scale signal conduction within the cardiac tissue by the 128-FET array.
The 128-FET array is classified into 40 units, where each arm has five units. Each unit is labelled by the combination of the located arm name (e.g., "A"), the loop number (e.g., "1"), and the relative location (e.g., "a"). In each unit, the FETs are labelled in i, ii, iii, and iv. Within each unit, intercellular signal conductions via gap junctions in neighboring cells are analyzed, and the latencies are denoted in the heatmaps. The signal conduction velocity inside each unit can be calculated. For instance, in E2b, the signal transmits 70 μm from E2iv to E2vi in 5 ms. By analyzing all signal conductions within each unit, we calculated the small-scale conduction velocity, whose average and standard deviation are 18.8 ± 7.5 μm·ms^{-1}, which are consistent with previously reported values. The triangle for each unit indicates the selected FET that has the earliest spike within that unit. We use the selected FET in each unit as the reference point to calculate the signal conduction velocities among different units. NaN: Not a number, meaning no cellular signal was recorded.

We used the FETs in each unit to study small-scale intercellular signal conductions, whose velocities are calculated to be 18.8 ± 7.5 μm·ms^{-1}, consistent with reported values[12] (Figures. 83 and 84).

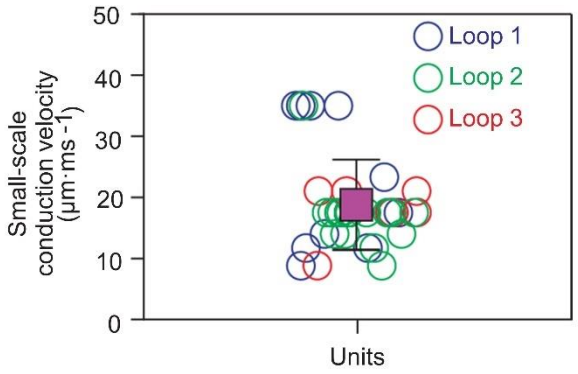

Figure 84. Calculation of small-scale intercellular signal conduction velocity.
The small-scale intercellular signal conduction velocity measured within each unit. The average and standard deviation of the velocities within the 40 units are 18.8 ± 7.5 μm·ms^{-1}.

We also leveraged the relatively large spacing between the 40 units of FETs to acquire the velocity of large-scale signal conduction (Figure 85). For each of the three heights, signals propagate clockwise among the units, forming a loop (Figure 77).

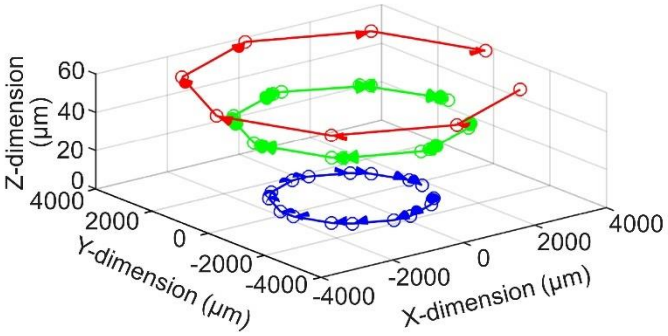

Figure 85. 3D visualization of the signal conduction in the whole 3D tissue construct.
On all three loops, the signal conduction directions are consistent, beginning at arm H and then propagating to arm A.

The calculated signal conduction velocities on the three different loops are 10.9 μm·ms^{-1}, 11.8 μm·ms^{-1}, and 12.2 μm·ms^{-1} (Figure 86).

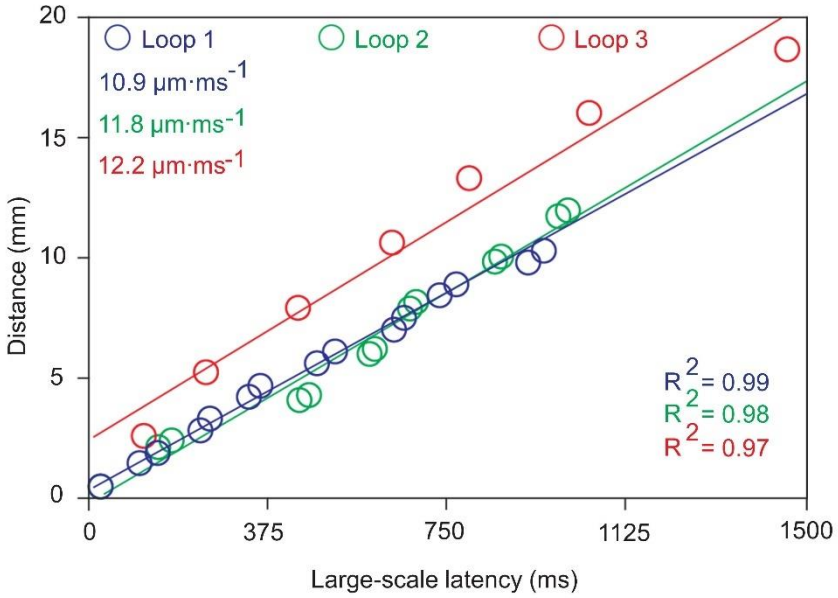

Figure 86. Calculation of large-scale intercellular signal conduction velocity.
Linear fit of the intercellular signal conduction velocity across the units in each loop.

The calculated large-scale conduction velocities are generally slower than those small-scale within each unit, because we assume the signal conduction path is linear from point to point on the large-scale; the actual path is likely to follow a zig-zag pattern[12], depending on the cells' relative positions and their electrical coupling states.

5.5 Conclusion.

In this chapter, we have introduced using a 128-FET array to record intracellular action potentials of cardiomyocytes in 3D cardiac tissue constructs. Neonatal rat cardiomyocytes were engineered to microtissue for the signal recording. The 128-FET array has its sensors located in three different heights making it have great contact with individual cells in the tissue construct.

The intracellular action potentials of cardiomyocytes were recorded and the calculated small-scale conduction velocity between cells is ~18.8 $\mu m \cdot ms^{-1}$. The large-scale conduction velocity is also calculated as ~11 $\mu m \cdot ms^{-1}$.

Chapters Five, in full, is a partial reprint of the materials: 'Three-dimensional transistor arrays for intra- and inter-cellular recording, Yue Gu, Chunfeng Wang, Namheon Kim, Jingxin Zhang, Tsui Min Wang, Jennifer Stowe, Rohollah Nasiri, Jinfeng Li, Daibo Zhang, Albert Yang, Leo Huan-Hsuan Hsu, Xiaochuan Dai, Jing Mu, Zheyuan Liu, Muyang Lin, Weixin Li, Chonghe Wang, Hua Gong, Yimu Chen, Yusheng Lei, Hongjie Hu, Yang Li, Lin Zhang, Zhenlong Huang, Xingcai Zhang, Samad Ahadian, Pooja Banik, Liangfang Zhang, Xiaocheng Jiang, Peter J. Burke, Ali Khademhosseini, Andrew D. McCulloch, Sheng Xu, accepted in Nature Nanotechnology, 2021'. The dissertation author was the first author of this paper.

Chapter 6. Summary

Throughout the time in Professor Xu's group as a graduate student, I have worked towards making significant contributions in the engineering of a soft platform for cellular electrophysiology research. Our contributions are substantial, as summarizing below.

In Chapter One, the fundamentals of electrophysiology, tools used for electrophysiology recordings, and the current problems presented in this field have been introduced and discussed. In Chapter Two, comprehensive methods including conventional micro/nanofabrication and a unique compressive buckling technique have been discussed. Our work presents a reliable approach to fabricating the FET array, which has excellent electrical properties. In Chapter Three, intracellular recordings on single cells have been discussed. Our work presents a high-sensitivity sensor that can record subthreshold cellular signals, which is comparable to the gold standard patch-clamp. In Chapter Four, intracellular and intercellular signal propagation have been studied using the 10-FET array. Our work demonstrates the first direct measurement of intracellular conduction. The conduction velocity inside a cell is five times that of the intercellular conduction. In Chapter Five, intracellular signals of cardiomyocytes of 3D cardiac tissue constructs have been recorded for the first time. Our work presents the first arrayed device for intracellular sensing on 3D cell cultures, which paves the way for in vivo measurement in the future.

In Chapter 2, we elaborate on the comprehensive method to fabricate the soft FET array. Using the conventional micro/nanofabrication techniques made the multilayered precursor on a planar substrate. A unique transfer printing and compressive buckling technique realized the 3D

structure of the FET array. Electrical characterization of the FET shows it has excellent sensitivity and small noise, which are the prerequisite of sensing cellular electrical activities, especially subthreshold membrane potentials. We also introduced a method to functionalize the FET surface by application of phospholipid bilayer materials, which greatly facilitate the internalization process of the FET into the cell body.

In Chapter Three, we have summarized the approaches of recording a single cell's intracellular and extracellular electrophysiological signals using the FET array. In general, the electrical recordings maintain both the shape and amplitude of the action potentials of HL-1 cells and primary cardiomyocytes. These recordings have been validated by the gold standard patch-clamp. And the phospholipid coatings on the FET surface are critical to forming a stable sensor and cell membrane interface leading to faithful recordings by the FET array. Further, the cells' correspondence to abnormal external solutions or drugs were recorded using the FET array, which further shows the FET's excellent performance in sensing electrophysiological signals, providing promise for applications in drug screening.

In Chapter Four, we have demonstrated the results of using ten FET sensors to record multiple cells simultaneously. Each high-sensitivity FET sensor can pick up an intracellular action potential from each cell. The calculated conduction velocity between cells ranges from 35.1~39.3 $\mu m \cdot ms^{-1}$. Intracellular signal conduction is also recorded for the first time, and the velocity was calculated to be ~182 $\mu m \cdot ms^{-1}$. Using confocal microscopy while recording the intracellular signal propagation validates the intracellular recording with two FET sensors. We discover that the intracellular signal propagation direction is related to the electrical coupling states between cells.

In Chapter Five, we have introduced using a 128-FET array to record intracellular action potentials of cardiomyocytes in 3D cardiac tissue constructs. Neonatal rat cardiomyocytes were engineered to microtissue for the signal recording. The 128-FET array has its sensors located in three different heights making it have great contact with individual cells in the tissue construct. The intracellular action potentials of cardiomyocytes were recorded, and the calculated small-scale conduction velocity between cells is ~18.8 $\mu m \cdot ms^{-1}$. The large-scale conduction velocity is also calculated as ~11 $\mu m \cdot ms^{-1}$.

In conclusion, with the device size down to the submicron regime, the high sensitivity, and the high signal-to-noise ratio, FETs have attracted growing attention as a tool for interrogating electrogenic cells in the past decade. However, 2D planar FETs for extracellular interfacing usually lack one-to-one correspondence between the cells and FETs, providing information on an ensemble of cells near the FET. 3D FETs allow direct interfacing with the cytoplasm of cells, which ensures the correspondence to each specific recorded cell. However, existing 3D FET devices are not scalable for large-scale, high-spatial-resolution sensing8. With an unprecedented number and pre-defined layout of sensors, the 3D FET array in this work can fill this technological gap. The arrayed FETs provide tremendous opportunities for studying cardiomyocytic intracellular ionic dynamics and gap junctional signal conduction between two adjacent cells, which enables us to acquire more insights into cardiomyocytic physiologies. By continuously monitoring the change in intercellular signal conduction directions over time, we can relate such information to evolutionary heart disease models, such as myocardial infarction, long-standing heart failure, atrial fibrillation, cardiac fibrosis, arrhythmias, tachycardias, and arrhythmogenesis40.

The intracellular signal discloses more meaningful information about the cell type and density of various ion channels. Particularly, the full-amplitude action potentials are highly relevant to the disease status and pathology of the cells[101]. Sub-threshold signals can potentially shed light on the theory of intercellular synchronization[33], the mechanism of electrophysiological modulation[77,102], and how these sub-threshold signals impact the development of sensory systems[103]. The studies of the conduction behavior would not only promote the understanding of the ionic transport across organellular membranes within a cell[93] but also facilitate the studies of electrical coupling between different cells. These findings carry significant implications for understanding subcellular electrophysiology, organellar ionic dynamics[93], organelle-cell membrane interaction, and their influences on cellular physiological activities, including proliferation, differentiation, and apoptosis.

Further explorations could ensue by applying the 3D FET array to various types of cardiac tissues, such as embryonic stem cell-derived cardiomyocytes, myocyte-fibroblast cocultures, and other general electrogenic cells such as neurons. Reliable recordings of 3D tissues on a large scale may reveal the cellular alignment directions. Future translating this platform technology for in vivo studies will depend on the FET's capability of penetrating through the thick membranes on the myocardium and the cortex, as well as eliminating motion artifacts induced by heart beating and brain pulsation. To that end, further refinement of the 3D FETs' structures (e.g., tip size, spacing, and relative positions), array size, materials of low modulus, surface coating, and deployment approach, as well as using artificial-intelligence assisted signal processing algorithms, would be

essential to prevent severe immune responses and enhance the quality and duration of the recordings.

References

1. Rettinger, J., Schwarz, S. & Schwarz, W. *Electrophysiology*. (Springer International Publishing, 2016).

2. Fish, E. Electric Fish and the Discovery Animal Electricity of The mystery of the electric fish motivated research into. *American Scientist* **72**, 598-607 (2014).

3. Vardi, R., Goldental, A., Sardi, S., Sheinin, A. & Kanter, I. Simultaneous multi-patch-clamp and extracellular-array recordings: Single neuron reflects network activity. *Sci Rep* **6**, 36228 (2016).

4. Bear, M. F. *Neuroscience: exploring the brain*. Fourth edition edn, (2016).

5. Wang, G., Wyskiel, D. R., Yang, W., Wang, Y., Milbern, L. C., Lalanne, T., Jiang, X., Shen, Y., Sun, Q. Q. & Zhu, J. J. An optogenetics- and imaging-assisted simultaneous multiple patch-clamp recording system for decoding complex neural circuits. *Nat. Protoc.* **10**, 397-412 (2015).

6. Stett, A., Burkhardt, C., Weber, U., Van Stiphout, P. & Knott, T. CYTOCENTERING : A Novel Technique Enabling Automated Cell-by-Cell Patch Clamping with the C YTO P ATCH ™ Chip. *Receptors and Channels* **9**, 59-66 (2011).

7. Asmild, M., Oswald, N., Krzywkowski, K. M., Friis, S., Jacobsen, R. B., Reuter, D., Taboryski, R., Kutchinsky, J., Vestergaard, R. K., Schroder, R. L., Sorensen, C. B., Bech, M., Korsgaard, M. P. & Willumsen, N. J. Upscaling and automation of electrophysiology: toward high throughput screening in ion channel drug discovery. *Receptors Channels* **9**, 49-58 (2003).

8. Lepple-Wienhues, A., Ferlinz, K., Seeger, A. & Schafer, A. Flip the tip: an automated, high quality, cost-effective patch clamp screen. *Receptors Channels* **9**, 13-17 (2003).

9. Dunlop, J., Bowlby, M., Peri, R., Vasilyev, D. & Arias, R. High-throughput electrophysiology: an emerging paradigm for ion-channel screening and physiology. *Nat Rev Drug Discov* **7**, 358-368 (2008).

10. Papke, R. L. & Stokes, C. Working with OpusXpress: methods for high volume oocyte experiments. *Methods* **51**, 121-133 (2010).

11. Zhang, A. & Lieber, C. M. Nano-Bioelectronics. *Chem Rev* **116**, 215-257 (2016).

12. Abbott, J., Ye, T., Qin, L., Jorgolli, M., Gertner, R. S., Ham, D. & Park, H. CMOS nanoelectrode array for all-electrical intracellular electrophysiological imaging. *Nat. Nanotechnol.* **12**, 460-466 (2017).

13. Branner, A. & Normann, R. A. A multielectrode array for intrafascicular recording and stimulation in sciatic nerve of cats. *Brain Res Bull* **51**, 293-306 (2000).

14. Normann, R. A., Maynard, E. M., Rousche, P. J. & Warren, D. J. A neural interface for a cortical vision prosthesis. *Vision Res* **39**, 2577-2587 (1999).

15. Henze, D. A., Borhegyi, Z., Csicsvari, J., Mamiya, A., Harris, K. D. & Buzsáki, G. Intracellular Features Predicted by Extracellular Recordings in the Hippocampus In Vivo. *Journal of Neurophysiology* **84**, 390-400 (2000).

16. Lee, J. H., Jeong, Y. K., Peters, J. A., Nam, G. H., Jin, S. & Kim, J. H. In Situ Fabrication of Nano Transistors by Selective Deposition of a Gate Dielectric around Carbon Nanotubes. *ACS Appl Mater Interfaces* **7**, 24094-24102 (2015).

17. Mercanzini, A., Cheung, K., Buhl, D. L., Boers, M., Maillard, A., Colin, P., Bensadoun, J. C., Bertsch, A. & Renaud, P. Demonstration of cortical recording using novel flexible polymer neural probes. *Sensor Actuat a-Phys* **143**, 90-96 (2008).

18. Barz, F., Trouillet, V., Paul, O. & Ruther, P. CMOS-Compatible, Flexible, Intracortical Neural Probes. *IEEE Trans Biomed Eng* **67**, 1366-1376 (2020).

19. Luan, L., Wei, X., Zhao, Z., Siegel, J. J., Potnis, O., Tuppen, C. A., Lin, S., Kazmi, S., Fowler, R. A., Holloway, S., Dunn, A. K., Chitwood, R. A. & Xie, C. Ultraflexible nanoelectronic probes form reliable, glial scar-free neural integration. *Sci Adv* **3**, e1601966 (2017).

20. Jia, W. J., Dai, G. B., Geng, G. S., Yang, Z. B., Tang, M. J., Xiu, P., Zhang, F. & Wang, H. B. Recent Studies on the Application of Patch-Clamp Technique in Cellular Electrophysiology. *Gao Xiao Hua Xue Gong Cheng Xue Bao/Journal of Chemical Engineering of Chinese Universities* **32**, 767-778 (2018).

21. Takeuchi, S., Suzuki, T., Mabuchi, K. & Fujita, H. 3D flexible multichannel neural probe array. *J Micromech Microeng* **14**, 104-107 (2004).

22. Kim, D. H., Viventi, J., Amsden, J. J., Xiao, J., Vigeland, L., Kim, Y. S., Blanco, J. A., Panilaitis, B., Frechette, E. S., Contreras, D., Kaplan, D. L., Omenetto, F. G., Huang, Y., Hwang, K. C., Zakin, M. R., Litt, B. & Rogers, J. A. Dissolvable films of silk fibroin for ultrathin conformal bio-integrated electronics. *Nat. Mater.* **9**, 511-517 (2010).

23. Miklas, J. W., Nunes, S. S., Sofla, A., Reis, L. A., Pahnke, A., Xiao, Y., Laschinger, C. & Radisic, M. Bioreactor for modulation of cardiac microtissue phenotype by combined static stretch and electrical stimulation. *Biofabrication* **6**, 024113 (2014).

24. Fu, Y., Wang, N., Yang, A., Law, H. K., Li, L. & Yan, F. Highly Sensitive Detection of Protein Biomarkers with Organic Electrochemical Transistors. *Adv Mater* **29**, 1-7 (2017).

25. Hai, A., Shappir, J. & Spira, M. E. In-cell recordings by extracellular microelectrodes. *Nat Methods* **7**, 200-202 (2010).

26. Hai, A., Shappir, J. & Spira, M. E. Long-term, multisite, parallel, in-cell recording and stimulation by an array of extracellular microelectrodes. *J Neurophysiol* **104**, 559-568 (2010).

27. Lin, Z. C. & Cui, B. Nanowire transistors: room for manoeuvre. *Nat Nanotechnol* **9**, 94-96 (2014).

28. Xie, C., Lin, Z., Hanson, L., Cui, Y. & Cui, B. Intracellular recording of action potentials by nanopillar electroporation. *Nat. Nanotechnol.* **7**, 185-190 (2012).

29. Abbott, J., Ye, T., Krenek, K., Gertner, R. S., Ban, S., Kim, Y., Qin, L., Wu, W., Park, H. & Ham, D. A nanoelectrode array for obtaining intracellular recordings from thousands of connected neurons. *Nat. Biomed. Eng.* **4**, 232-241 (2020).

30. Lin, Z. C., McGuire, A. F., Burridge, P. W., Matsa, E., Lou, H. Y., Wu, J. C. & Cui, B. Accurate nanoelectrode recording of human pluripotent stem cell-derived cardiomyocytes for assaying drugs and modeling disease. *Microsyst. Nanoeng.* **3**, 16080 (2017).

31. Liu, R., Chen, R., Elthakeb, A. T., Lee, S. H., Hinckley, S., Khraiche, M. L., Scott, J., Pre, D., Hwang, Y., Tanaka, A., Ro, Y. G., Matsushita, A. K., Dai, X., Soci, C., Biesmans, S., James, A., Nogan, J., Jungjohann, K. L., Pete, D. V., Webb, D. B., Zou, Y., Bang, A. G. & Dayeh, S. A. High Density Individually Addressable Nanowire Arrays Record Intracellular Activity from Primary Rodent and Human Stem Cell Derived Neurons. *Nano Lett* **17**, 2757-2764 (2017).

32. Robinson, J. T., Jorgolli, M., Shalek, A. K., Yoon, M. H., Gertner, R. S. & Park, H. Vertical nanowire electrode arrays as a scalable platform for intracellular interfacing to neuronal circuits. *Nat. Nanotechnol.* **7**, 180-184 (2012).

33. Eschermann, J. F., Stockmann, R., Hueske, M., Vu, X. T., Ingebrandt, S. & Offenhausser, A. Action potentials of HL-1 cells recorded with silicon nanowire transistors. *Appl Phys Lett* **95**, 1-4 (2009).

34. Qing, Q., Pal, S. K., Tian, B., Duan, X., Timko, B. P., Cohen-Karni, T., Murthy, V. N. & Lieber, C. M. Nanowire transistor arrays for mapping neural circuits in acute brain slices. *Proc. Natl. Acad. Sci. USA* **107**, 1882-1887 (2010).

35. Viventi, J., Kim, D. H., Moss, J. D., Kim, Y. S., Blanco, J. A., Annetta, N., Hicks, A., Xiao, J., Huang, Y., Callans, D. J., Rogers, J. A. & Litt, B. A conformal, bio-interfaced class of silicon electronics for mapping cardiac electrophysiology. *Sci. Transl. Med.* **2**, 24ra22 (2010).

36. Fang, H., Yu, K. J., Gloschat, C., Yang, Z., Chiang, C. H., Zhao, J., Won, S. M., Xu, S., Trumpis, M., Zhong, Y., Song, E., Han, S. W., Xue, Y., Xu, D., Cauwenberghs, G., Kay, M., Huang, Y., Viventi, J., Efimov, I. R. & Rogers, J. A. Capacitively Coupled Arrays of Multiplexed Flexible Silicon Transistors for Long-Term Cardiac Electrophysiology. *Nat Biomed Eng* **1**2017).

37. Fan, Y. J., Li, X., Kuang, S. Y., Zhang, L., Chen, Y. H., Liu, L., Zhang, K., Ma, S. W., Liang, F., Wu, T., Wang, Z. L. & Zhu, G. Highly Robust, Transparent, and Breathable Epidermal Electrode. *ACS Nano* **12**, 9326-9332 (2018).

38. Tian, B. & Lieber, C. M. Synthetic nanoelectronic probes for biological cells and tissues. *Annu. Rev. Anal. Chem. (Palo Alto Calif)* **6**, 31-51 (2013).

39. Dai, X., Zhou, W., Gao, T., Liu, J. & Lieber, C. M. Three-dimensional mapping and regulation of action potential propagation in nanoelectronics-innervated tissues. *Nat. Nanotechnol.* **11**, 776-782 (2016).

40. Xie, C., Liu, J., Fu, T. M., Dai, X., Zhou, W. & Lieber, C. M. Three-dimensional macroporous nanoelectronic networks as minimally invasive brain probes. *Nat Mater* **14**, 1286-1292 (2015).

41. Duan, X., Gao, R., Xie, P., Cohen-Karni, T., Qing, Q., Choe, H. S., Tian, B., Jiang, X. & Lieber, C. M. Intracellular recordings of action potentials by an extracellular nanoscale field-effect transistor. *Nat. Nanotechnol.* **7**, 174-179 (2011).

42. Fu, T. M., Duan, X., Jiang, Z., Dai, X., Xie, P., Cheng, Z. & Lieber, C. M. Sub-10-nm intracellular bioelectronic probes from nanowire-nanotube heterostructures. *Proc Natl Acad Sci USA* **111**, 1259-1264 (2014).

43. Gao, R., Strehle, S., Tian, B., Cohen-Karni, T., Xie, P., Duan, X., Qing, Q. & Lieber, C. M. Outside looking in: nanotube transistor intracellular sensors. *Nano Lett* **12**, 3329-3333 (2012).

44. Tian, B., Cohen-Karni, T., Qing, Q., Duan, X., Xie, P. & Lieber, C. M. Three-dimensional, flexible nanoscale field-effect transistors as localized bioprobes. *Science* **329**, 830-834 (2010).

45. Qing, Q., Jiang, Z., Xu, L., Gao, R., Mai, L. & Lieber, C. M. Free-standing kinked nanowire transistor probes for targeted intracellular recording in three dimensions. *Nat. Nanotechnol.* **9**, 142-147 (2014).

46. Xu, S., Yan, Z., Jang, K. I., Huang, W., Fu, H., Kim, J., Wei, Z., Flavin, M., McCracken, J., Wang, R., Badea, A., Liu, Y., Xiao, D., Zhou, G., Lee, J., Chung, H. U., Cheng, H., Ren, W., Banks, A., Li, X., Paik, U., Nuzzo, R. G., Huang, Y., Zhang, Y. & Rogers, J. A. Materials science. Assembly of micro/nanomaterials into complex, three-dimensional architectures by compressive buckling. *Science* **347**, 154-159 (2015).

47. Zhao, H., Li, K., Han, M., Zhu, F., Vazquez-Guardado, A., Guo, P., Xie, Z., Park, Y., Chen, L., Wang, X., Luan, H., Yang, Y., Wang, H., Liang, C., Xue, Y., Schaller, R. D., Chanda, D., Huang, Y., Zhang, Y. & Rogers, J. A. Buckling and twisting of advanced materials into morphable 3D mesostructures. *Proc Natl Acad Sci U S A* **116**, 13239-13248 (2019).

48. Won, S. M., Wang, H., Kim, B. H., Lee, K., Jang, H., Kwon, K., Han, M., Crawford, K. E., Li, H., Lee, Y., Yuan, X., Kim, S. B., Oh, Y. S., Jang, W. J., Lee, J. Y., Han, S., Kim, J., Wang, X., Xie, Z., Zhang, Y., Huang, Y. & Rogers, J. A. Multimodal Sensing with a Three-Dimensional Piezoresistive Structure. *ACS Nano* **13**, 10972-10979 (2019).

49. Wang, X., Guo, X., Ye, J., Zheng, N., Kohli, P., Choi, D., Zhang, Y., Xie, Z., Zhang, Q., Luan, H., Nan, K., Kim, B. H., Xu, Y., Shan, X., Bai, W., Sun, R., Wang, Z., Jang, H., Zhang, F., Ma, Y., Xu, Z., Feng, X., Xie, T., Huang, Y., Zhang, Y. & Rogers, J. A. Freestanding 3D Mesostructures, Functional Devices, and Shape-Programmable Systems Based on Mechanically Induced Assembly with Shape Memory Polymers. *Adv Mater* **31**, e1805615 (2019).

50. Fu, H., Nan, K., Bai, W., Huang, W., Bai, K., Lu, L., Zhou, C., Liu, Y., Liu, F., Wang, J., Han, M., Yan, Z., Luan, H., Zhang, Y., Zhang, Y., Zhao, J., Cheng, X., Li, M., Lee, J. W., Liu, Y., Fang, D., Li, X., Huang, Y., Zhang, Y. & Rogers, J. A. Morphable 3D mesostructures and microelectronic devices by multistable buckling mechanics. *Nat Mater* **17**, 268-276 (2018).

51. Kim, B. H., Lee, J., Won, S. M., Xie, Z., Chang, J. K., Yu, Y., Cho, Y. K., Jang, H., Jeong, J. Y., Lee, Y., Ryu, A., Kim, D. H., Lee, K. H., Lee, J. Y., Liu, F., Wang, X., Huo, Q., Min, S., Wu, D., Ji, B., Banks, A., Kim, J., Oh, N., Jin, H. M., Han, S., Kang, D., Lee, C. H., Song, Y. M., Zhang, Y., Huang, Y., Jang, K. I. & Rogers, J. A. Three-Dimensional Silicon Electronic Systems Fabricated by Compressive Buckling Process. *ACS Nano* **12**, 4164-4171 (2018).

52. Yan, Z., Zhang, F., Wang, J., Liu, F., Guo, X., Nan, K., Lin, Q., Gao, M., Xiao, D., Shi, Y., Qiu, Y., Luan, H., Kim, J. H., Wang, Y., Luo, H., Han, M., Huang, Y., Zhang, Y. & Rogers,

J. A. Controlled mechanical buckling for origami-inspired construction of 3D microstructures in advanced materials. *Adv Funct Mater* **26**, 2629-2639 (2016).

53. Ling, Y., Zhuang, X., Xu, Z., Xie, Y., Zhu, X., Xu, Y., Sun, B., Lin, J., Zhang, Y. & Yan, Z. Mechanically Assembled, Three-Dimensional Hierarchical Structures of Cellular Graphene with Programmed Geometries and Outstanding Electromechanical Properties. *ACS Nano* **12**, 12456-12463 (2018).

54. Won, S. M., Song, E., Reeder, J. T. & Rogers, J. A. Emerging Modalities and Implantable Technologies for Neuromodulation. *Cell* **181**, 115-135 (2020).

55. Jang, K. I., Li, K., Chung, H. U., Xu, S., Jung, H. N., Yang, Y., Kwak, J. W., Jung, H. H., Song, J., Yang, C., Wang, A., Liu, Z., Lee, J. Y., Kim, B. H., Kim, J. H., Lee, J., Yu, Y., Kim, B. J., Jang, H., Yu, K. J., Kim, J., Lee, J. W., Jeong, J. W., Song, Y. M., Huang, Y., Zhang, Y. & Rogers, J. A. Self-assembled three dimensional network designs for soft electronics. *Nat Commun* **8**, 15894 (2017).

56. Yan, Z., Zhang, F., Liu, F., Han, M., Ou, D., Liu, Y., Lin, Q., Guo, X., Fu, H., Xie, Z., Gao, M., Huang, Y., Kim, J., Qiu, Y., Nan, K., Kim, J., Gutruf, P., Luo, H., Zhao, A., Hwang, K. C., Huang, Y., Zhang, Y. & Rogers, J. A. Mechanical assembly of complex, 3D mesostructures from releasable multilayers of advanced materials. *Sci Adv* **2**, e1601014 (2016).

57. Luan, H., Cheng, X., Wang, A., Zhao, S., Bai, K., Wang, H., Pang, W., Xie, Z., Li, K., Zhang, F., Xue, Y., Huang, Y. & Zhang, Y. Design and Fabrication of Heterogeneous, Deformable Substrates for the Mechanically Guided 3D Assembly. *ACS Appl Mater Interfaces* **11**, 3482-3492 (2019).

58. Xu, S., Yan, Z., Jang, K.-I., Huang, W., Fu, H., Kim, J., Wei, Z., Flavin, M., McCracken, J., Wang, R., Badea, A., Liu, Y., Xiao, D., Zhou, G., Lee, J., Chung, H. U., Cheng, H., Ren, W., Banks, A., Li, X., Paik, U., Nuzzo, R. G., Huang, Y., Zhang, Y. & Rogers, J. A. Assembly of micro/nanomaterials into complex, three-dimensional architectures by compressive buckling. *Science* **347**, 154-159 (2015).

59. Liu, Y., Wang, X., Xu, Y., Xue, Z., Zhang, Y., Ning, X., Cheng, X., Xue, Y., Lu, D., Zhang, Q., Zhang, F., Liu, J., Guo, X., Hwang, K. C., Huang, Y., Rogers, J. A. & Zhang, Y. Harnessing the interface mechanics of hard films and soft substrates for 3D assembly by controlled buckling. *Proc Natl Acad Sci U S A* **116**, 15368-15377 (2019).

60. Liu, F., Chen, Y., Song, H., Zhang, F., Fan, Z., Liu, Y., Feng, X., Rogers, J. A., Huang, Y. & Zhang, Y. High Performance, Tunable Electrically Small Antennas through Mechanically Guided 3D Assembly. *Small* **15**, e1804055 (2019).

61. Dargent, T., Haddadi, K., Lasri, T., Clément, N., Ducatteau, D., Legrand, B., Tanbakuchi, H. & Theron, D. An interferometric scanning microwave microscope and calibration method for sub-fF microwave measurements. *Rev Sci Instrum* **84**, 123705 (2013).

62. Li, J., Nernati, Z., Haddadi, K., Wallace, D. C. & Burke, P. J. in *2018 IEEE/MTT-S International Microwave Symposium - IMS.* 115-118.

63. Sonmez, B. G., Ertop, O. & Mutlu, S. Modelling and Realization of a Water-Gated Field Effect Transistor (WG-FET) Using 16-nm-Thick Mono-Si Film. *Sci Rep* **7**, 12190 (2017).

64. Lee, J. W., Jang, D., Kim, G. T., Mouis, M. & Ghibaudo, G. Analysis of charge sensitivity and low frequency noise limitation in silicon nanowire sensors. *Journal of Applied Physics* **107**, 044501 (2010).

65. Yuan, S., Fan, X. & Wang, Z. Design and fabrication of field-effect biosensors for biochemical detection. *IET Nanobiotechnol* **8**, 208-215 (2014).

66. Lee, J. W., Yun, W. S. & Ghibaudo, G. Impact of trap localization on low-frequency noise in nanoscale device. *Journal of Applied Physics* **115**, 194501 (2014).

67. Noy, A. Bionanoelectronics. *Adv. Mater.* **23**, 807-820 (2011).

68. Hempel, F., Law, J. K., Nguyen, T. C., Munief, W., Lu, X., Pachauri, V., Susloparova, A., Vu, X. T. & Ingebrandt, S. PEDOT:PSS organic electrochemical transistor arrays for extracellular electrophysiological sensing of cardiac cells. *Biosens Bioelectron* **93**, 132-138 (2017).

69. Grant, A. O. Cardiac Ion Channels. *Circulation: Arrhythmia and Electrophysiology* **2**, 185-194 (2009).

70. Elasser, A. & Chow, T. P. Silicon carbide benefits and advantages for power electronics circuits and systems. *Proceedings of the IEEE* **90**, 969-986 (2002).

71. Patlak, J. B. & Ortiz, M. Slow currents through single sodium channels of the adult rat heart. *Journal of General Physiology* **86**, 89-104 (1985).

72. Anumonwo, J. M. B., Tallini, Y. N., Vetter, F. J. & Jalife, J. Action Potential Characteristics and Arrhythmogenic Properties of the Cardiac Conduction System of the Murine Heart. *Circ. Res.* **89**, 329-335 (2001).

73. Gong, H., Chen, F., Huang, Z., Gu, Y., Zhang, Q., Chen, Y., Zhang, Y., Zhuang, J., Cho, Y. K., Fang, R. H., Gao, W., Xu, S. & Zhang, L. Biomembrane-Modified Field Effect Transistors for Sensitive and Quantitative Detection of Biological Toxins and Pathogens. *ACS Nano* **13**, 3714-3722 (2019).

74. Hu, C.-M. J., Zhang, L., Aryal, S., Cheung, C., Fang, R. H. & Zhang, L. Erythrocyte membrane-camouflaged polymeric nanoparticles as a biomimetic delivery platform. *Proc Natl Acad Sci USA* **108**, 10980-10985 (2011).

75. Ai, X., Wang, S., Duan, Y., Zhang, Q., Chen, M. S., Gao, W. & Zhang, L. Emerging Approaches to Functionalizing Cell Membrane-Coated Nanoparticles. *Biochemistry* **60**, 941-955 (2020).

76. Wang, S., Duan, Y., Zhang, Q., Komarla, A., Gong, H., Gao, W. & Zhang, L. Drug Targeting via Platelet Membrane–Coated Nanoparticles. *Small Structures* **1**, 2000018 (2020).

77. Hu, C.-M. J., Fang, R. H., Copp, J., Luk, B. T. & Zhang, L. A biomimetic nanosponge that absorbs pore-forming toxins. *Nat Nanotechnol* **8**, 336-340 (2013).

78. Zhuang, J., Duan, Y., Zhang, Q., Gao, W., Li, S., Fang, R. H. & Zhang, L. Multimodal Enzyme Delivery and Therapy Enabled by Cell Membrane-Coated Metal–Organic Framework Nanoparticles. *Nano Letters* **20**, 4051-4058 (2020).

79. Aalipour, A., Xu, A. M., Leal-Ortiz, S., Garner, C. C. & Melosh, N. A. Plasma Membrane and Actin Cytoskeleton as Synergistic Barriers to Nanowire Cell Penetration. *Langmuir* **30**, 12362-12367 (2014).

80. Prinz, C. N. Interactions between semiconductor nanowires and living cells. *J Condens Matter Phys* **27**, 233103 (2015).

81. Tian, B. & Lieber, C. M. Nanowired Bioelectric Interfaces. *Chem. Rev.* **119**, 9136-9152 (2019).

82. Zhao, Y., You, S. S., Zhang, A., Lee, J. H., Huang, J. & Lieber, C. M. Scalable ultrasmall three-dimensional nanowire transistor probes for intracellular recording. *Nat. Nanotechnol.* **14**, 783-790 (2019).

83. Elcarpio, J. O. B. D., Ahinski, A. N. B., Zzo, N. I. J. I., Claycomb, W. C., Lanson, N. a., Stallworth, B. S., Egeland, D. B., Delcarpio, J. B., Bahinski, a. & Izzo, N. J. HL-1 cells : A cardiac muscle cell line that contracts and retains phenotypic characteristics of the adult cardiomyocyte. *Proc. Natl. Acad. Sci. USA* **95**, 2979-2984 (1998).

84. White, S. M., Constantin, P. E. & Claycomb, W. C. Cardiac physiology at the cellular level: use of cultured HL-1 cardiomyocytes for studies of cardiac muscle cell structure and function. *Am J Physiol Heart Circ Physiol* **286**, H823-829 (2004).

85. Czeschik, A., Rinklin, P., Derra, U., Ullmann, S., Holik, P., Steltenkamp, S., Offenhausser, A. & Wolfrum, B. Nanostructured cavity devices for extracellular stimulation of HL-1 cells. *Nanoscale* **7**, 9275-9281 (2015).

86. Smith, A. W., Segar, C. E., Nguyen, P. K., MacEwan, M. R., Efimov, I. R. & Elbert, D. L. Long-term culture of HL-1 cardiomyocytes in modular poly(ethylene glycol) microsphere-based scaffolds crosslinked in the phase-separated state. *Acta Biomater* **8**, 31-40 (2012).

87. Liu, H., Bolonduro, O. A., Hu, N., Ju, J., Rao, A. A., Duffy, B. M., Huang, Z., Black, L. D. & Timko, B. P. Heart-on-a-Chip Model with Integrated Extra- and Intracellular Bioelectronics for Monitoring Cardiac Electrophysiology under Acute Hypoxia. *Nano Lett* **20**, 2585-2593 (2020).

88. Dutta, S., Minchole, A., Quinn, T. A. & Rodriguez, B. Electrophysiological properties of computational human ventricular cell action potential models under acute ischemic conditions. *Prog Biophys Mol Biol* **129**, 40-52 (2017).

89. Kireev, D., Seyock, S., Lewen, J., Maybeck, V., Wolfrum, B. & Offenhausser, A. Graphene Multielectrode Arrays as a Versatile Tool for Extracellular Measurements. *Adv. Healthc. Mater.* **6**, 1601433 (2017).

90. Hegyi, B., Chen-Izu, Y., Izu, L. T. & Bányász, T. Altered K+ current profiles underlie cardiac action potential shortening in hyperkalemia and β-adrenergic stimulation. *Can. J. Physiol. Pharmacol.* **97**, 773-780 (2019).

91. Lu, Y.-Y., Cheng, C.-C., Chen, Y.-C., Lin, Y.-K., Chen, S.-A. & Chen, Y.-J. Electrolyte disturbances differentially regulate sinoatrial node and pulmonary vein electrical activity: A contribution to hypokalemia- or hyponatremia-induced atrial fibrillation. *Heart Rhythm* **13**, 781-788 (2016).

92. Bers, D. M., Barry, W. H. & Despa, S. Intracellular Na^+ regulation in cardiac myocytes. *Cardiovasc. Res.* **57**, 897-912 (2003).

93. Brown, A. M., Lee, K. S. & Powell, T. Voltage clamp and internal perfusion of single rat heart muscle cells. *J. Physiol.* **318**, 455-477 (1981).

94. Gouwens, N. W. & Wilson, R. I. Signal Propagation in Drosophila Central Neurons. *J. of Neurosci.* **29**, 6239-6249 (2009).

95. McCain, M. L., Desplantez, T., Geisse, N. A., Rothen-Rutishauser, B., Oberer, H., Parker, K. K. & Kleber, A. G. Cell-to-cell coupling in engineered pairs of rat ventricular cardiomyocytes: relation between Cx43 immunofluorescence and intercellular electrical conductance. *Am. J. Physiol. Heart Circ. Physiol.* **302**, H443-450 (2012).

96. Lancaster, M. A. & Knoblich, J. A. Organogenesis in a dish: Modeling development and disease using organoid technologies. *Science* **345**, 1247125 (2014).

97. Zuppinger, C. 3D Cardiac Cell Culture: A Critical Review of Current Technologies and Applications. *Front. Cardiovasc. Med.* **6**, 87 (2019).

98. Hong, G., Fu, T. M., Qiao, M., Viveros, R. D., Yang, X., Zhou, T., Lee, J. M., Park, H. G., Sanes, J. R. & Lieber, C. M. A method for single-neuron chronic recording from the retina in awake mice. *Science* **360**, 1447-1451 (2018).

99. Zhao, Y., Rafatian, N., Feric, N. T., Cox, B. J., Aschar-Sobbi, R., Wang, E. Y., Aggarwal, P., Zhang, B., Conant, G., Ronaldson-Bouchard, K., Pahnke, A., Protze, S., Lee, J. H., Davenport Huyer, L., Jekic, D., Wickeler, A., Naguib, H. E., Keller, G. M., Vunjak-Novakovic, G., Broeckel, U., Backx, P. H. & Radisic, M. A Platform for Generation of Chamber-Specific Cardiac Tissues and Disease Modeling. *Cell* **176**, 913-927 e918 (2019).

100. Dipalo, M., Amin, H., Lovato, L., Moia, F., Caprettini, V., Messina, G. C., Tantussi, F., Berdondini, L. & De Angelis, F. Intracellular and Extracellular Recording of Spontaneous Action Potentials in Mammalian Neurons and Cardiac Cells with 3D Plasmonic Nanoelectrodes. *Nano Letters* **17**, 3932-3939 (2017).

101. Dankerl, M., Eick, S., Hofmann, B., Hauf, M., Ingebrandt, S., Offenhausser, A., Stutzmann, M. & Garrido, J. A. Diamond Transistor Array for Extracellular Recording From Electrogenic Cells. *Adv. Funct. Mater.* **19**, 2915-2923 (2009).

102. Hess, L. H., Jansen, M., Maybeck, V., Hauf, M. V., Seifert, M., Stutzmann, M., Sharp, I. D., Offenhausser, A. & Garrido, J. A. Graphene transistor arrays for recording action potentials from electrogenic cells. *Adv. Mater.* **23**, 5045-5049, 4968 (2011).

103. Gu, X., Yao, C., Liu, Y. & Hsing, I. M. 16-Channel Organic Electrochemical Transistor Array for In Vitro Conduction Mapping of Cardiac Action Potential. *Adv Healthc Mater* **5**, 2345-2351 (2016).